Supporting Information

Welding Metallophthalocyanines into Bimetallic Molecular Meshes for Ultrasensitive, Low-Power Chemiresistive Detection of Gases

Zheng Meng,[1] Aylin Aykanat,[1] Katherine A. Mirica[1,*]

[1]Department of Chemistry, Burke Laboratory, Dartmouth College, Hanover, NH 03755

**E-mail: Katherine.A.Mirica@dartmouth.edu*

Contents

1. Materials and Methods

Nickel(II) chloride (CAS N.O.: 7718-54-9), ammonium molybdate (CAS N.O.: 12054-85-2), urea (CAS N.O.: 57-13-6), boron tribromide (CAS N.O.: 10294-33-4), poly(methylhydrosiloxane) (PMHS, CAS N.O.: 63148-57-2), 1,1'-ferrocenediyl-bis(diphenylphosphine) (DPPF, CAS N.O.: 12150-46-8), tris(dibenzylideneacetone)dipalladium(0) ($Pd_2(dba)_3$, CAS N.O.: 51364-51-3), zinc cyanide (CAS N.O.: 557-21-1), $MgSO_4$ (CAS N.O.: 7487-88-9), 1,8-diazabicyclo[5.4.0]undec-7-ene (DBU, CAS N.O.: 6674-22-2), nickel(II) acetate tetrahydrate (CAS N.O.: 6018-89-9), copper acetate (CAS N.O.: 142-71-2), *N*-methyl-2-pyrrolidone (CAS N.O.: 68-12-2) and ethylene glycol (CAS N.O.: 107-21-1) were purchased form Sigma Aldrich. Methanol (CAS N.O.: 67-56-1), dichloromethane (CAS N.O.: 75-09-2), acetone (CAS N.O.: 67-64-1), *N, N*-dimethylacetamide (CAS N.O.: 127-19-5), and ethyl acetate (CAS N.O.: 141-78-6) were purchased from BDH Chemicals. Compounds 4,5-dimethoxyphthalodinitrile,[S1] 2,3-dibromo-6,7-dipropoxynaphthalene[S2] were synthesized according to the literature procedures. The yields were given as isolated yields. NMR spectra were recorded on a Bruker 600 MHz NMR spectrometer. The chemical shifts (δ) were expressed in ppm with internal standard tetramethylsilane (TMS) and solvent signals as internal references, and *J* values were given in Hz. Standard abbreviations indicating multiplicity were used as follows: s (singlet), br (broad), d (doublet), t (triplet), q (quartet), m (multiplet).

Scanning Electron Microscopy (SEM) and Energy Dispersive X-ray Spectroscopy (EDX) were performed using a Hitachi TM3000 SEM (Tokyo, Japan) equipped for X-ray microanalysis with a Bruker Edax light element Si(Li) detector (Billerica, MA). Transmission electron microscopy was carried out at a Tecnai F20ST FEG TEM instrument. Powder X-ray diffraction (PXRD) measurements were performed with a Rigaku sixth generation MiniFlex X-ray diffractometer with a 600 W (40 kV, 15 mA) CuKα (α = 1.54 Å) radiation source. Nitrogen adsorption experiments were performed with ASAP Plus 2020 (Mircromeritics, Norcross, Georgia) instrument. Elemental analyses were performed by *Atlantic Microlab, inc*. X-ray photoelectron spectroscopy experiments were conducted on a Physical Electronics Versaprobe II X-ray Photoelectron Spectrometer under ultrahigh vacuum (base pressure 10^{-10} mbar). The measurement chamber was equipped with a monochromatic Al (Kα) X-ray source. Both survey and high-resolution spectra were obtained using a beam diameter of 200 μm.

2. Synthesis of Phthalocyanine Based MOFs

2.1. Synthesis of (2,3,9,10,16,17,23,24-octahydroxyphthalocyaninato) nickel(II) NiPc

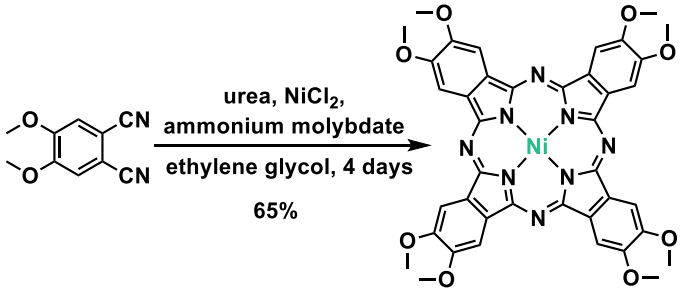

Synthesis of (2,3,9,10,16,17,23,24-octamethoxyphthalocyaninato) Ni(II). 4,5-Dimethoxyphthalodinitrile (5.0 g, 26.6 mmol), urea (1.6 g, 26.6 mmol), $NiCl_2$ (907 mg, 7 mmol), and ammonium molybdate (300 mg, 0.25 mmol) were refluxed in 100 mL of ethylene glycol under argon atmosphere for 4 days. The mixture was then cooled to room temperature, and 70 mL of water was added. The resulting solid was washed successively with methanol (40 mL × 5) and acetone (40 mL × 5) by using a centrifuge to collect precipitate. The product was then dried under vacuum to give (2,3,9,10,16,17,23,24-octamethoxyphthalocyaninato) Ni(II) as a dark green solid in 65% yield (3.52 g). The characterization data are consistent with literature.[S3]

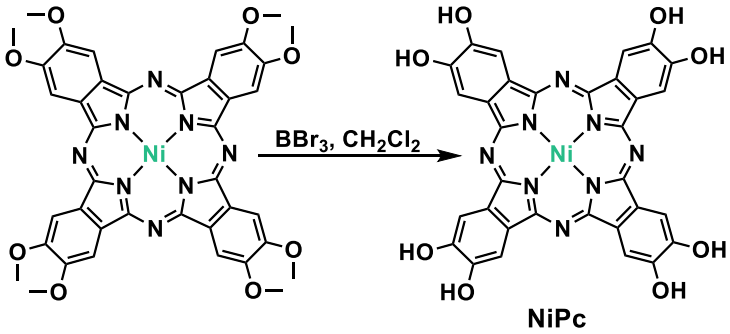

Synthesis of NiPc. (2,3,9,10,16,17,23,24-octamethoxyphthalocyaninato) Ni(II) (1.2 g, 14.76 mmol) was suspended in 50 mL of dichloromethane, and BBr_3 (5.7 mL, 59 mmol, 40 e.q.) was added under N_2. The mixture was stirred for 6 days, and then poured into 100 mL of H_2O. The precipitate was collected by centrifugation. The obtained solid was then dispersed in MeOH (20 mL), shaken vigorously and then centrifuged. The solid was collected and then subjected by MeOH washing using centrifuge for another 4 times. The product was then dried under vacuum to give **NiPc** as a dark green solid (0.78 g, yield 75%). M.P.: > 300 ^{o}C; ^{1}H NMR (600 M, DMSO-d_6): δ = 8.54 (s, 8H), 10.31 (br, 8H).

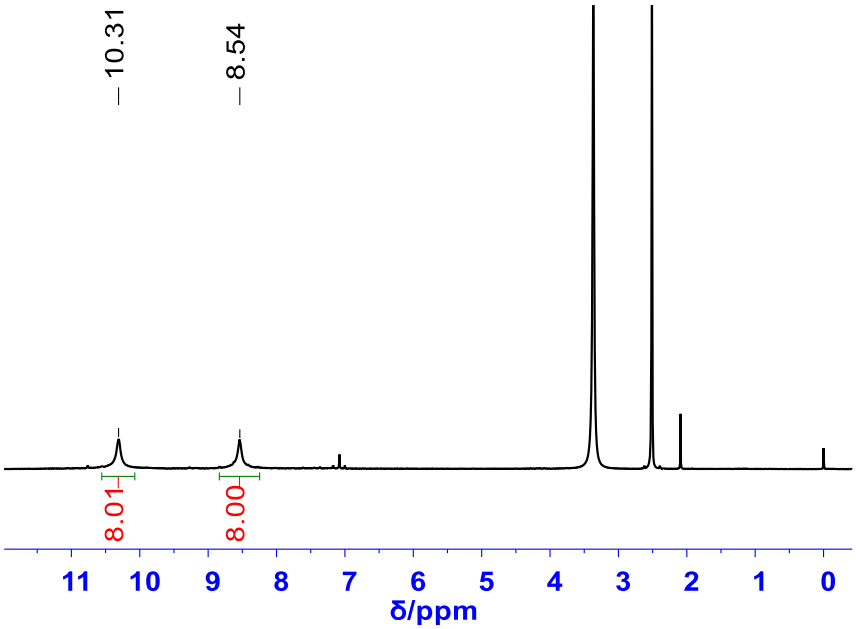

Figure S1. ^{1}H NMR (600 M, 298 K, DMSO-d_6) spectrum of NiPc.

2.2. Synthesis of (3,4,12,13,21,22,30,31-octahydroxynaphthalocyaninato) nickel(II) NiNPc

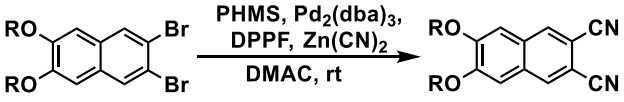

R= propyl

Synthesis of 6,7-dimethoxynaphthalene-2,3-dicarbonitrile. A 100 mL two-neck round-bottom flask was charged with 8.04 g (20 mmol) of dibromo-6,7-dipropoxynaphthalene in DMAC (40 mL) and PMHS (400 mg) was added at r.t. The reaction mixture was heated to 120 °C and $Pd_2(dba)_3$ (366 mg, 2 mol%) and DPPF (300 mg, 2.7 mol%) were added. Afterwards, $Zn(CN)_2$ (3.2 g, 24.8 mmol) was added in 4 portions within 5 hours. The reaction mixture was heated for another 2 hours and then cooled down to room temperature, diluted with EtOAc and filtered. Filtrate was washed with H_2O, dried with $MgSO_4$, and concentrated in vacuo. The crude product was recrystallized from an EtOAc/hexane (v/v=1/1) solvent to give colorless crystals (4.8 g, yield 81%). M.P.: 199-201 °C; ^{1}H NMR (600 M, $CDCl_3$): δ = 7.94 (s, 1H), 7.00 (s, 1H), 3.97 (t, J = 6.5 Hz, 2H), 1.80 (h, J = 7.1 Hz, 2H), 0.96 (t, J = 7.4 Hz, 3H); ^{13}C NMR (150 MHz, $CDCl_3$): δ = 153.0, 133.3, 129.8, 116.5, 107.9, 107.3, 70.7, 22.3, 10.5. HRMS (ESI): m/z calcd for $C_{18}H_{19}N_2O_2$: 295.1447; found: 295.1448 $[M+H]^+$.

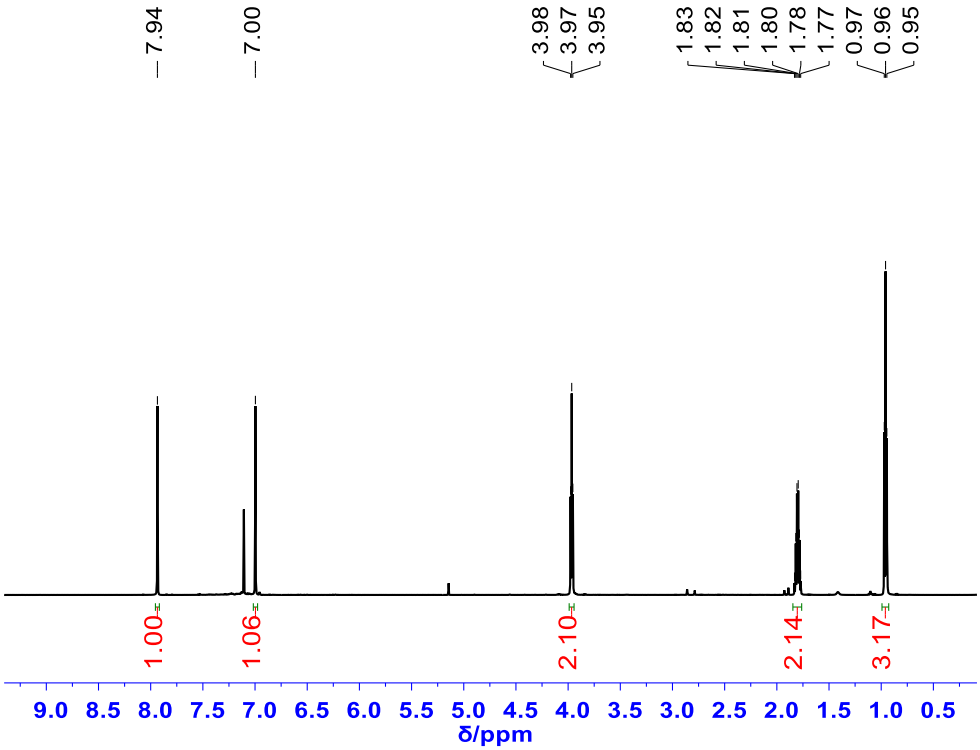

Figure S2. ^{1}H NMR (600 M, 298 K, $CDCl_3$) spectrum of 6,7-dimethoxynaphthalene-2,3-dicarbonitrile.

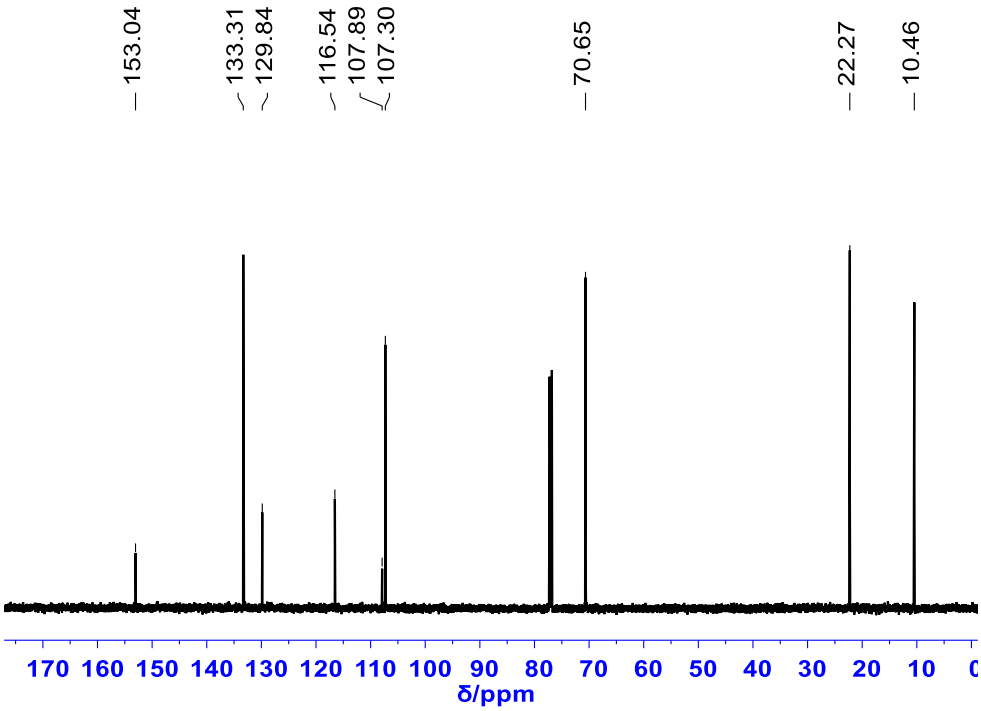

Figure S3. ^{13}C NMR (150 M, 298 K, $CDCl_3$) spectrum of 6,7-dimethoxynaphthalene-2,3-dicarbonitrile.

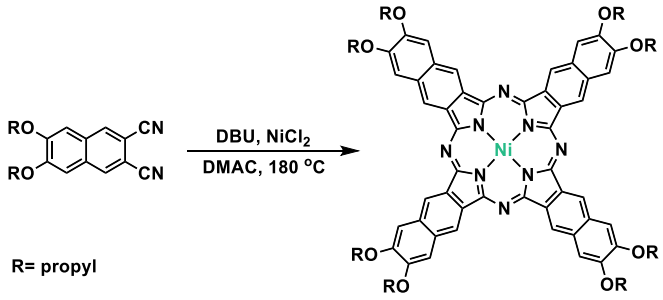

Synthesis of (3,4,12,13,21,22,30,31-octapropyl-2,3-naphthalocyaninato) nickel(II). To a solution of 6,7-dipropoxynaphthalene-2,3-dicarbonitrile (3.82 g, 13 mmol) in DMAC (20 mL) was added $NiCl_2$ (840 mg, 0.3 mmol, 0.5 eq.) and DBU (198 mg, 1.3 mmol). The mixture was then stirred at 180 °C under nitrogen for 3 days. After cooling to rt, the mixture was poured into water. The precipitate was collected by filtration. It was subsequently washed with methanol (10 mL × 5) and acetone (10 mL × 5) by using a centrifuge and then dried in vacuo, which finally gave a green solid as the product (2.81 g, yield 70%). M.P.: > 300 °C; ^{1}H NMR (600 M, DMSO-d_6): δ = 8.22 (s, 8H), 7.67 (s, 8H), 4.11 (t, J = 6.4 Hz, 17H), 1.91 – 1.74 (m, 17H), 1.04 (t, J = 7.3 Hz, 26H) ; ^{13}C NMR (150 MHz, DMSO-d_6): δ = 169.70, 151.37, 131.82, 127.37, 122.69, 110.11, 70.19, 22.35, 10.85. HRMS (ESI): m/z calcd for $C_{72}H_{72}N_8NiO_8$: 1234.4827; found: 1234.4851 $[M]^+$.

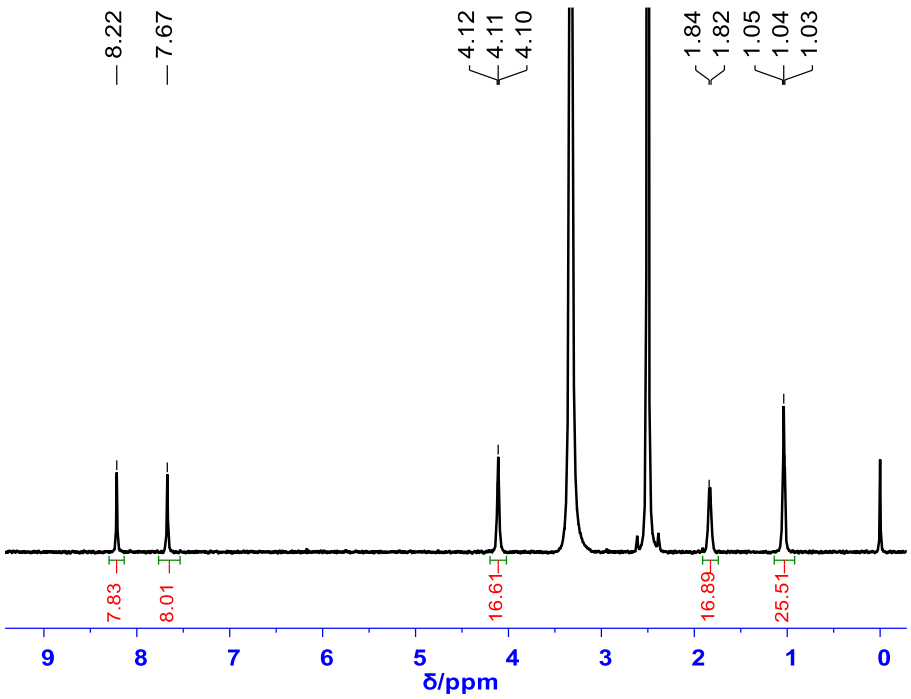

Figure S4. ^{1}H NMR (600 M, 298 K, DMSO-d_6) spectrum of (3,4,12,13,21,22,30,31-octapropyl-2,3-naphthalocyaninato) nickel(II).

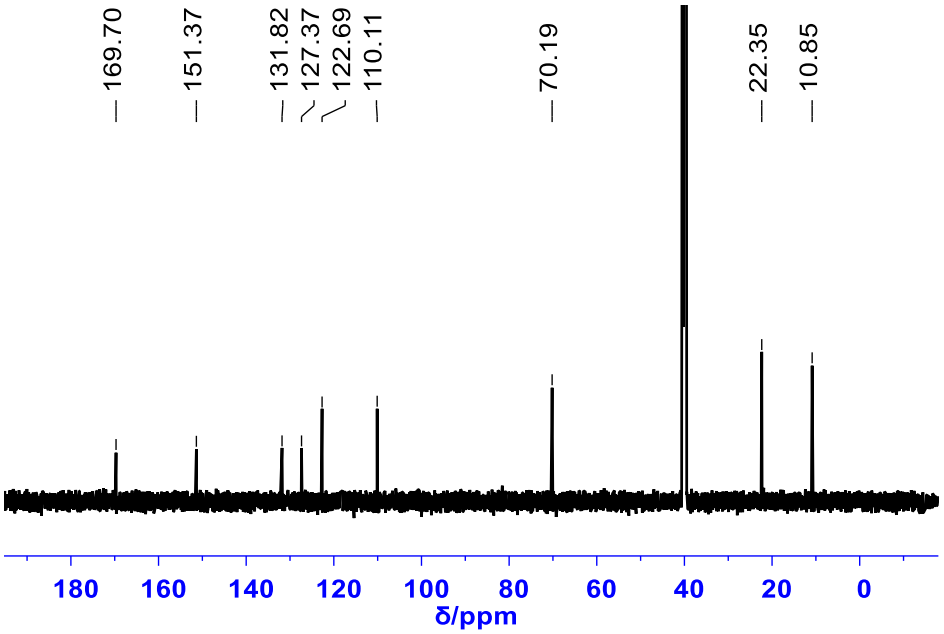

Figure S5. ^{13}C NMR (150 M, 298 K, DMSO-d_6) spectrum of (3,4,12,13,21,22,30,31-octapropyl-2,3-naphthalocyaninato) nickel(II).

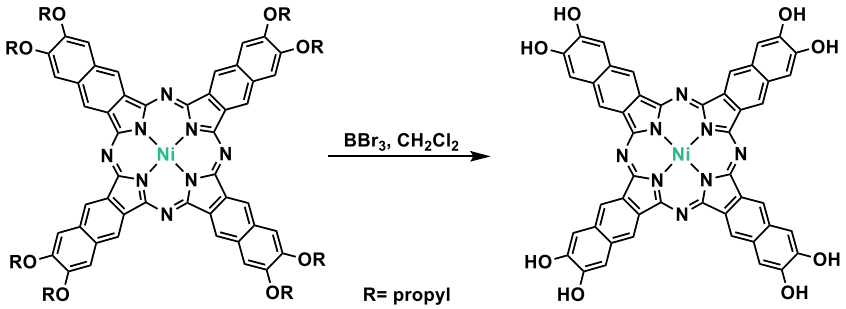

Synthesis of NiNPc. (3,4,12,13,21,22,30,31-octamethoxynaphthalocyaninato) Ni(II) (0.96 g, 0.78 mmol) was suspended in 50 mL of dichloromethane, and BBr_3 (3.0 mL, 31 mmol, 40 e.q.) was added. After the mixture was stirred for 5 days under N_2, 10 mL of methanol was added. The precipitate was collect by filtration, washed by methanol (20 mL × 6) by using a centrifuge and dried in vacuum to give **NiNPc** as a green solid (0.61 g, yield 87%). M.P.: > 300 ^{o}C; ^{1}H NMR (600 M, DMSO-d_6): δ = 10.25 (s, 8H), 8.11 (s, 8H), 7.43 (s, 8H); ^{13}C NMR (150 MHz, DMSO-d_6) δ = 169.8, 150.0, 131.5, 126.5, 122.4, 112.7; HRMS (TOF): m/z calcd for $C_{48}H_{24}N_8NiO_8$: 898.1071; found: 898.1089 $[M]^+$.

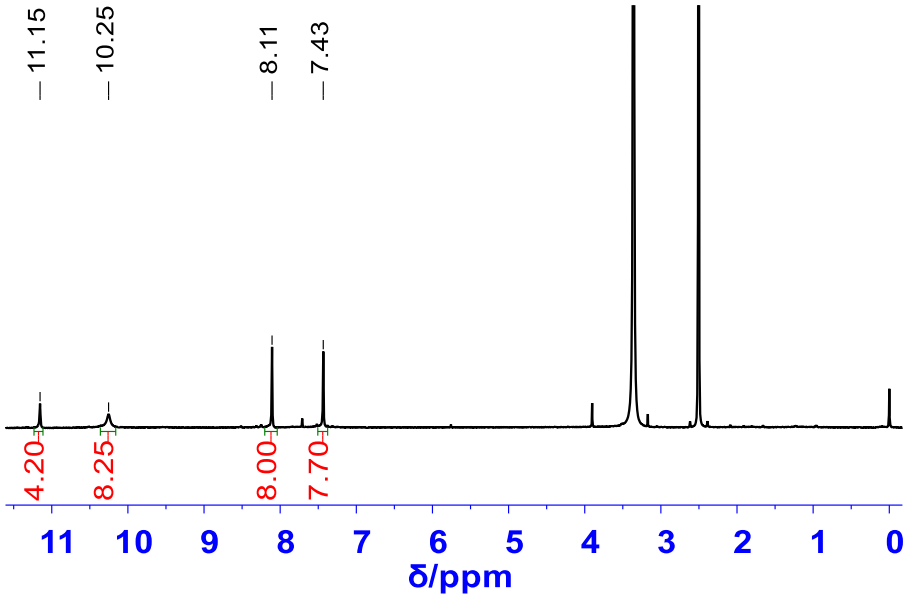

Figure S6. ^{1}H NMR (600 M, 298 K, DMSO-d_6) spectrum of **NiNPc.**

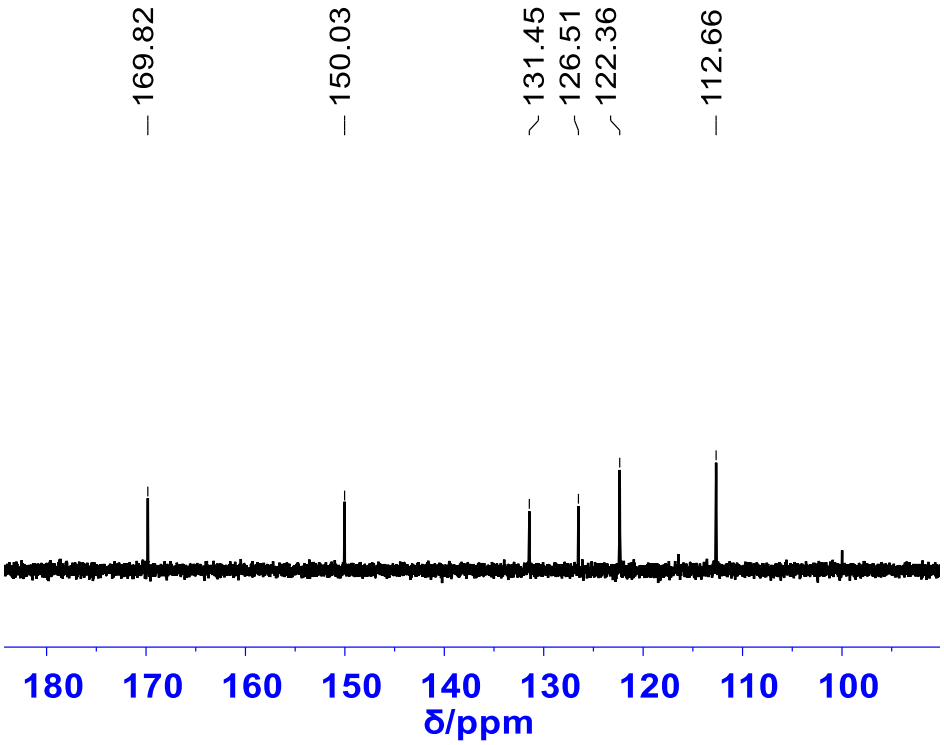

Figure S7. ^{13}C NMR (150 M, 298 K, DMSO-d_6) spectrum of **NiNPc.**

2.3. Synthesis of NiPc-M (M=Ni, Cu) MOF

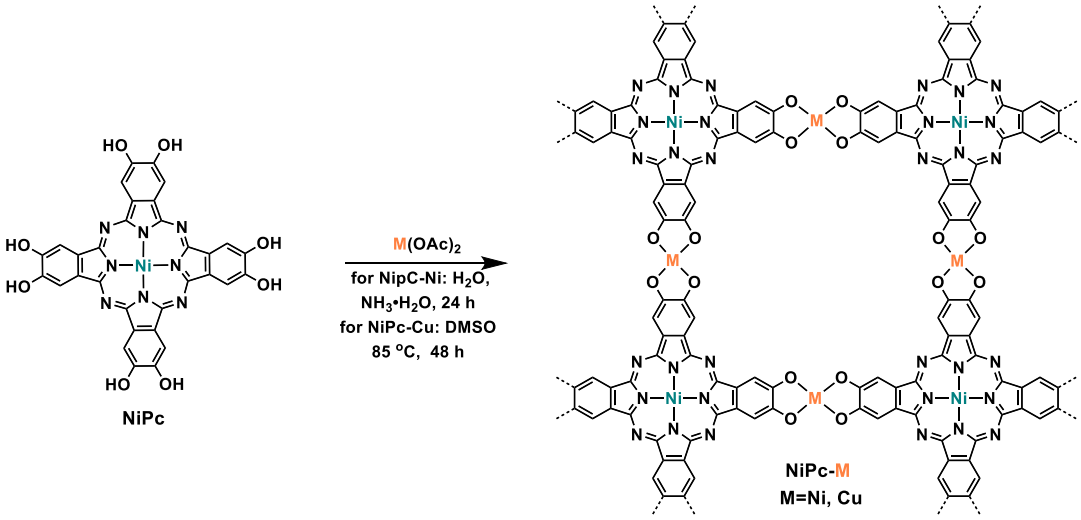

Synthesis of NiPc-Ni. To a 50 mL round bottom flask charged with **NiPc** (70 mg, 0.1 mmol), 12 mL of H_2O was added. The mixture was sonicated for 3 minutes to get a dark green suspension. Then 62.2 mg of $Ni(OAc)_2$•$4H_2O$ (2.5 e.q.) and 1.2 mL of NH_3•H_2O (25%~28%) were added (2.5 e.q.) successively. The mixture was sonicated for another 5 minutes and then was heated at 85°C for 24 hours with the flask loosely capped to permit exposure to air. After that the reaction was cooled to room temperature and the dark blue to black precipitate was filtered. The product was washed successively with DMSO/NH_3•H_2O (v/v=10:1, 3×10 mL), deionized water (5 × 20 mL), and acetone (5 × 20 mL). The filtrate was then transferred to a vacuum (20 mTorr) oven at 65°C and kept for 24 hours which gave **NiPc-Ni** as black solid (92 mg). The yield was 112% based on a theoretical formula of (**NiPc**)$_1Ni_2$.

Synthesis of NiPc-Cu. To a 50 mL round bottom flask charged with **NiPc** (70 mg, 0.1 mmol), 12 mL of DMSO were added. The mixture was sonicated for 3 minutes to get a clear dark green solution. Then 45.4 mg of copper acetate was added (2.5 e.q.). The mixture was sonicated for another 5 minutes and then was heated at 85°C for 48 hours with the flask loosely capped. After that the reaction was cooled to room temperature and the dark blue to black precipitate was filtered. The product was washed successively with DMSO (3×10 mL), deionized water (5 × 20 mL), and acetone (5 × 20 mL). The filtrate was then transferred to a vacuum (20 mTorr) oven at 65°C and kept for 24 hours, which gave **NiPc-Cu** as black solid (65 mg). The yield was 83% based on a theoretical formula of (**NiPc**)$_1Cu_2$.

2.4. Synthesis of NiNPc-M (M=Ni, Cu) MOFs

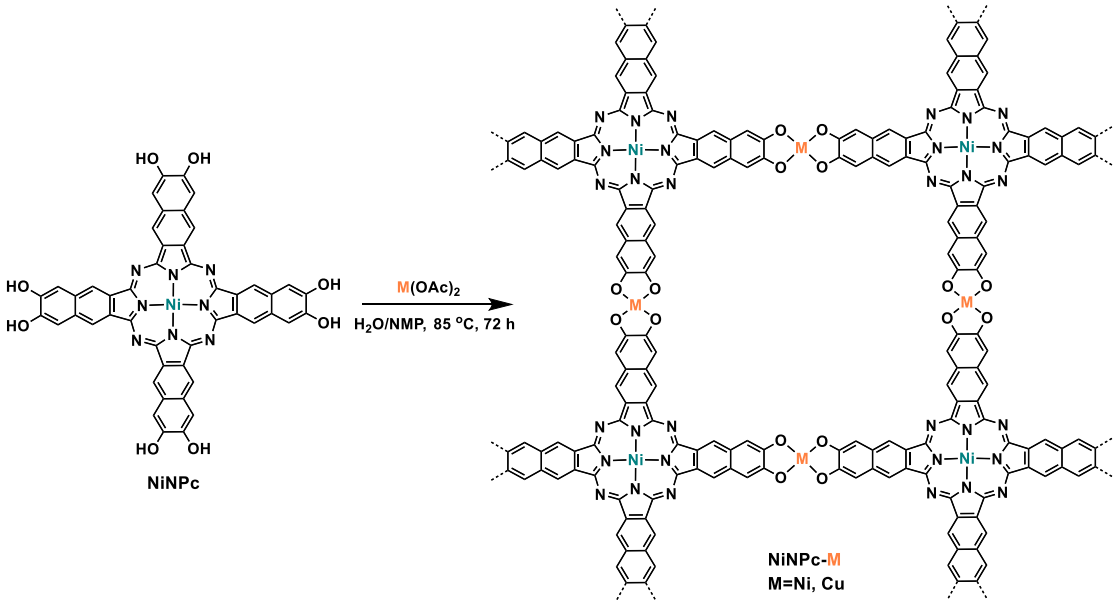

Synthesis of NiNPc-Ni. To a 50 mL round bottom flask charged with **NiNPc** (90 mg, 0.1 mmol), 6.6 mL of NMP and 6.6 mL of H_2O were added. The mixture was sonicated 15 minutes to get a homogeneous solution. Then 62.2 mg of $Ni(OAc)_2 \bullet 4H_2O$ was added (2.5 e.q.). The mixture was sonicated for another 5 minutes and then was heated at 85°C for 72 hours with the flask loosely capped. After that the reaction was cooled to room temperature and the dark blue precipitate was filtered. The product was washed successively with NMP/H_2O (v/v=1:1, 3×10 mL), deionized water (5 × 20 mL) and acetone (5 × 20 mL). The filtrate was then transferred to a vacuum (20 mTorr) oven at 65°C and dried for 24 hours, which gave **NiNPc-Ni** as dark blue solid (88 mg). The yield was 86% based on a theoretical formula of $(\mathbf{NiNPc})_1Ni_2$.

Synthesis of NiNPc-Cu. To a 50 mL round bottom flask charged with **NiNPc** (90 mg, 0.1 mmol), 6.6 mL of NMP and 6.6 mL of H_2O were added. The mixture was sonicated 15 minutes to get a homogeneous solution. Then 45.4 mg of copper acetate was added (2.5 e.q.). The mixture was sonicated for another 5 minutes and then was heated at 85°C for 72 hours with the flask loosely capped. After that the reaction was cooled to room temperature and the dark blue to black precipitate was filtered. The product was washed successively with NMP/H_2O (v/v=1:1, 3×10 mL), deionized water (3 × 20 mL), and acetone (5 × 20 mL). The filtrate was then transferred to a vacuum (20 mTorr) oven at 65°C and dried for 24 hours, which gave **NiNPc-Cu** as black solid (98 mg). The yield was 95% based on a theoretical formula of $(\mathbf{NiNPc})_1Cu_2$.

3. ATR-FTIR Spectroscopy

Infrared spectra were collected using a JASCO model FT IR-6100 Fourier transform infrared spectrophotometer.

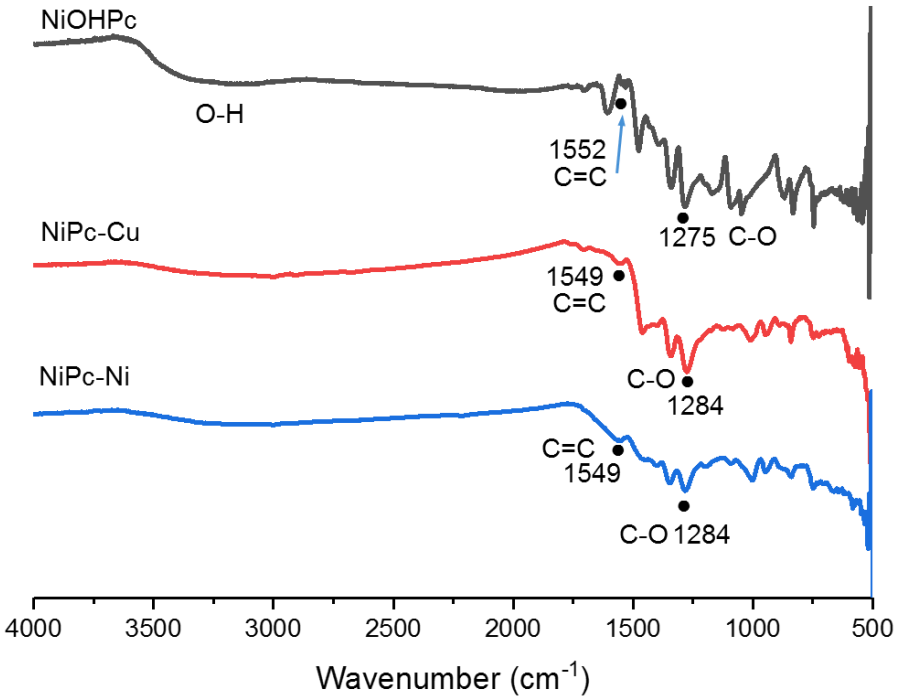

Figure S8. Comparison of ATR-FTIR spectra of **NiPc**, **NiPc-Cu** and **NiPc-Ni**.

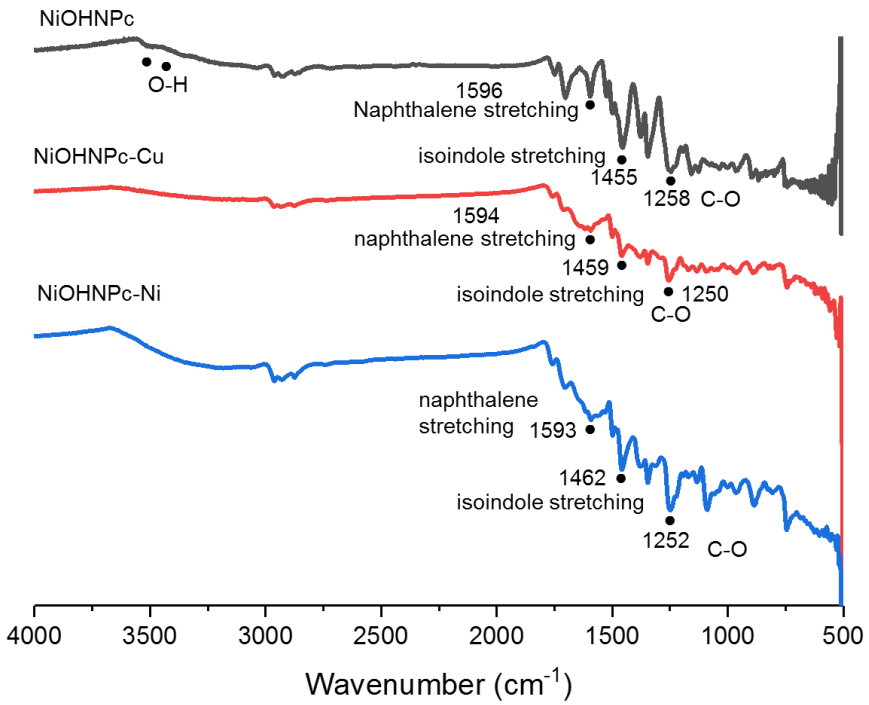

Figure S9. Comparison of ATR-FTIR spectra of **NiNPc**, **NiNPc-Cu** and **NiNPc-Ni**.

4. X-ray Photoelectron Spectroscopy

X-ray photoelectron spectroscopy (XPS) experiments were conducted on a Physical Electronics Versaprobe II X-ray Photoelectron Spectrometer under ultrahigh vacuum (base pressure 10^{-10} mbar). The measurement chamber was equipped with a monochromatic Al (Kα) X-ray source. Both survey and high-resolution spectra were obtained using a beam diameter of 200 μm. The spectra were processed with CasaXPS.

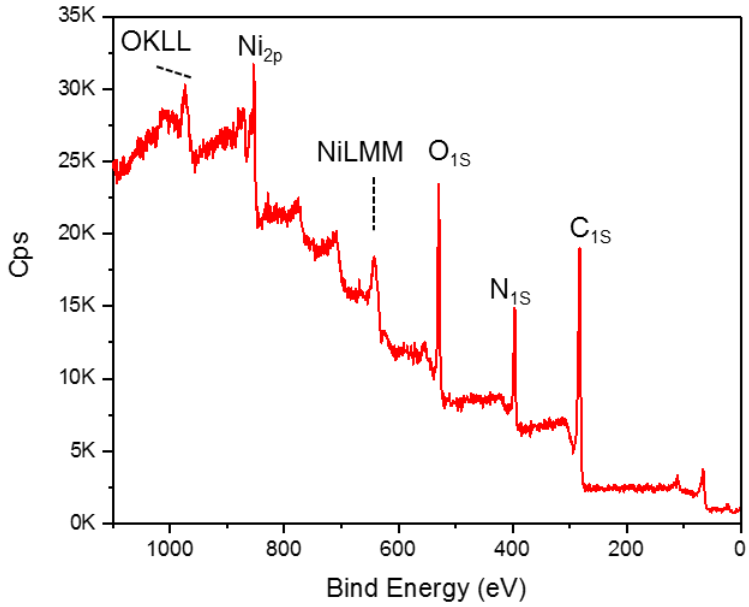

Figure S10. XPS survey spectrum of **NiPc-Ni** showing the presence of C, N, O, and Ni elements.

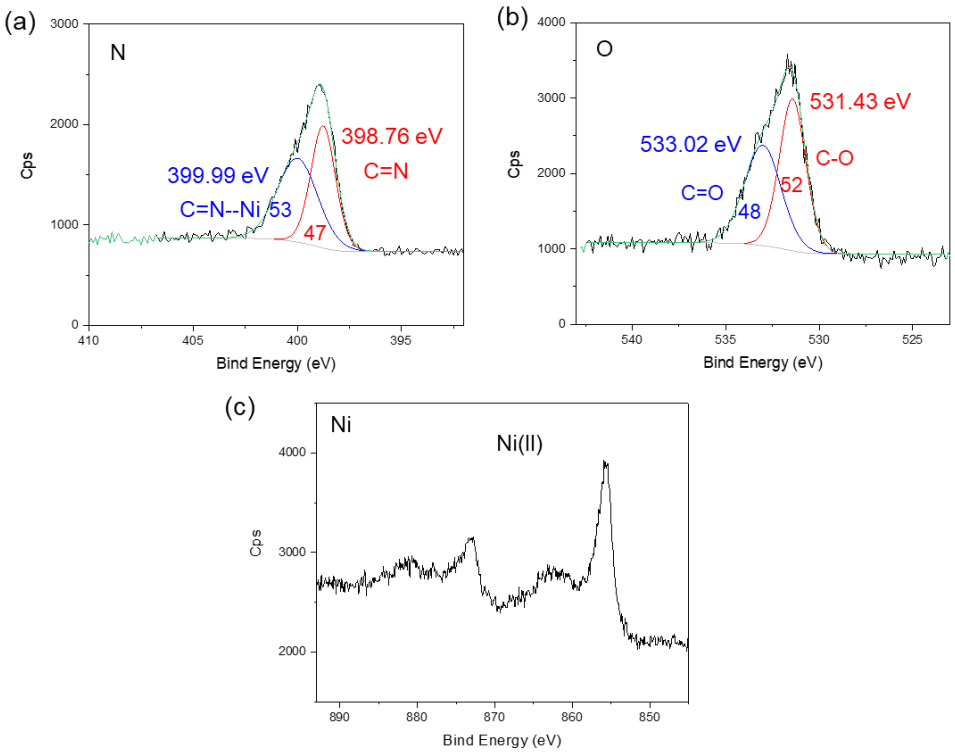

Figure S11. Deconvoluted XPS spectra of the **NiPc-Ni**: (a) N1s, (b) O1s, and (c) Ni2p. The black, grey, and green curve represent original data, background and the sum of the deconvoluted peaks, respectively. In (a) the blue curve corresponds to N(1s) in C=N···Ni and the red curve corresponds to C1s C=N-C. In (b) the red curve corresponds C-O and the blue curve corresponds to C=O.

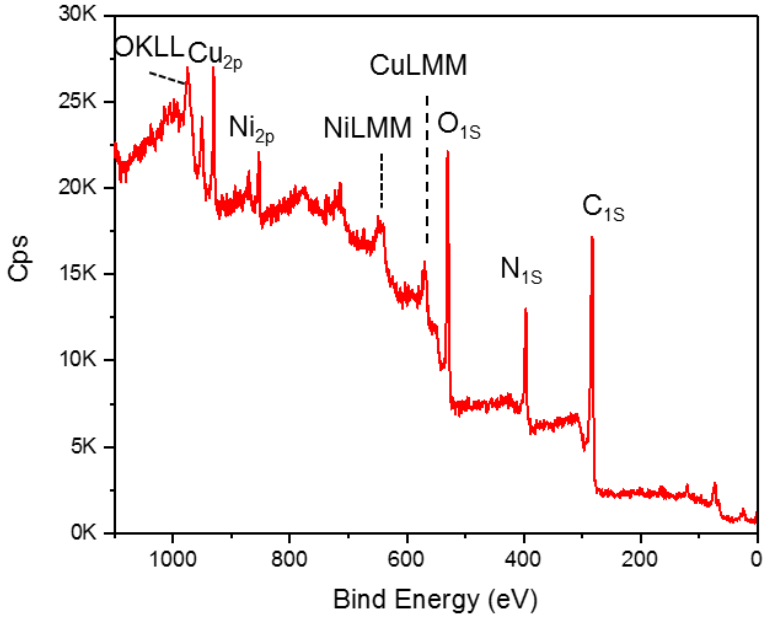

Figure S12. XPS survey spectrum of **NiPc-Cu** showing the presence of C, N, O, Ni and Cu elements.

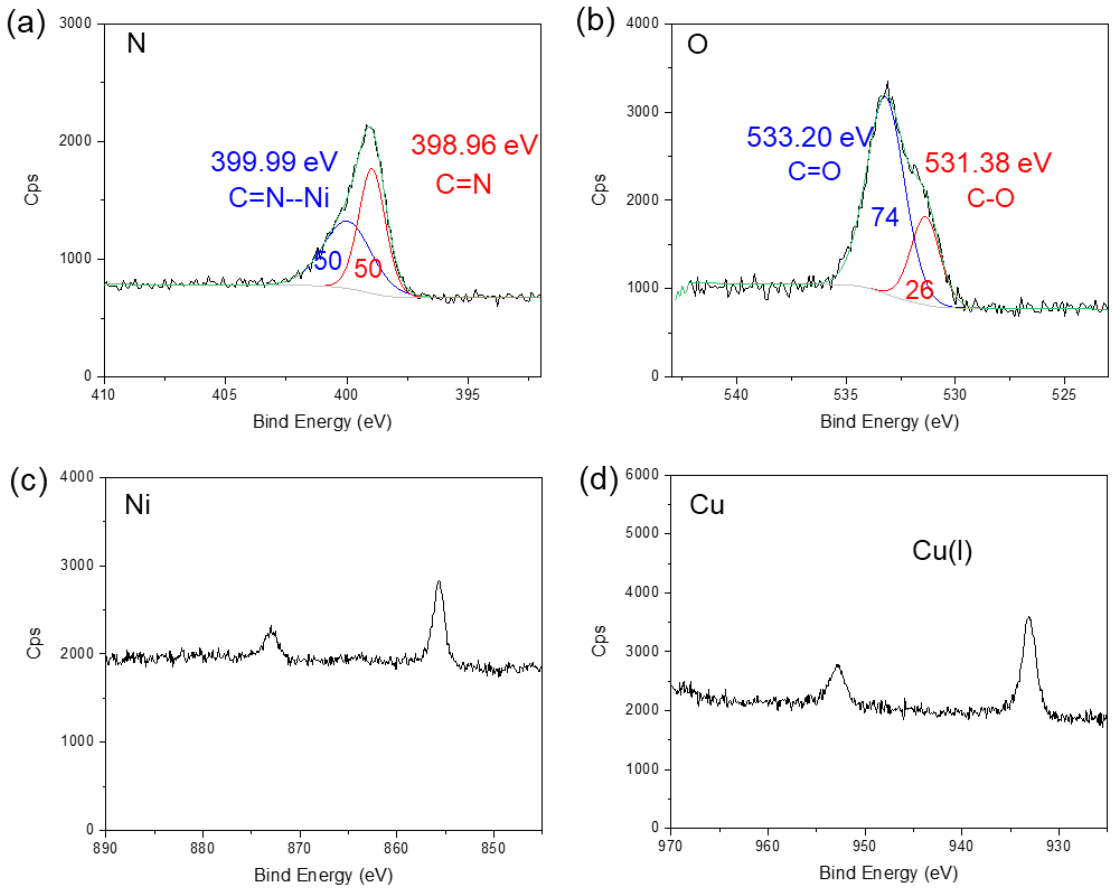

Figure S13. Deconvoluted XPS spectra of **NiPc-Cu**: (a) N1s (b) O1s, (c) Ni2p, (d) Cu2p. The black, grey, and green curve represent original data, background and the sum of the deconvoluted peaks, respectively. In (a) the blue curve corresponds to N(1s) in C=N···Ni and the red curve corresponds to C1s C=N-C. In (b) the red curve corresponds C-O and the blue curve corresponds to C=O.

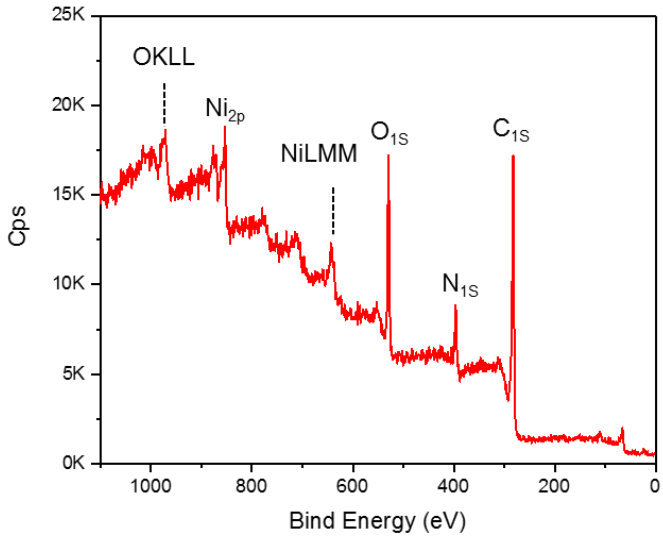

Figure S14. XPS survey spectrum of **NiNPc-Ni** showing C, N, O, Ni and Cu elements.

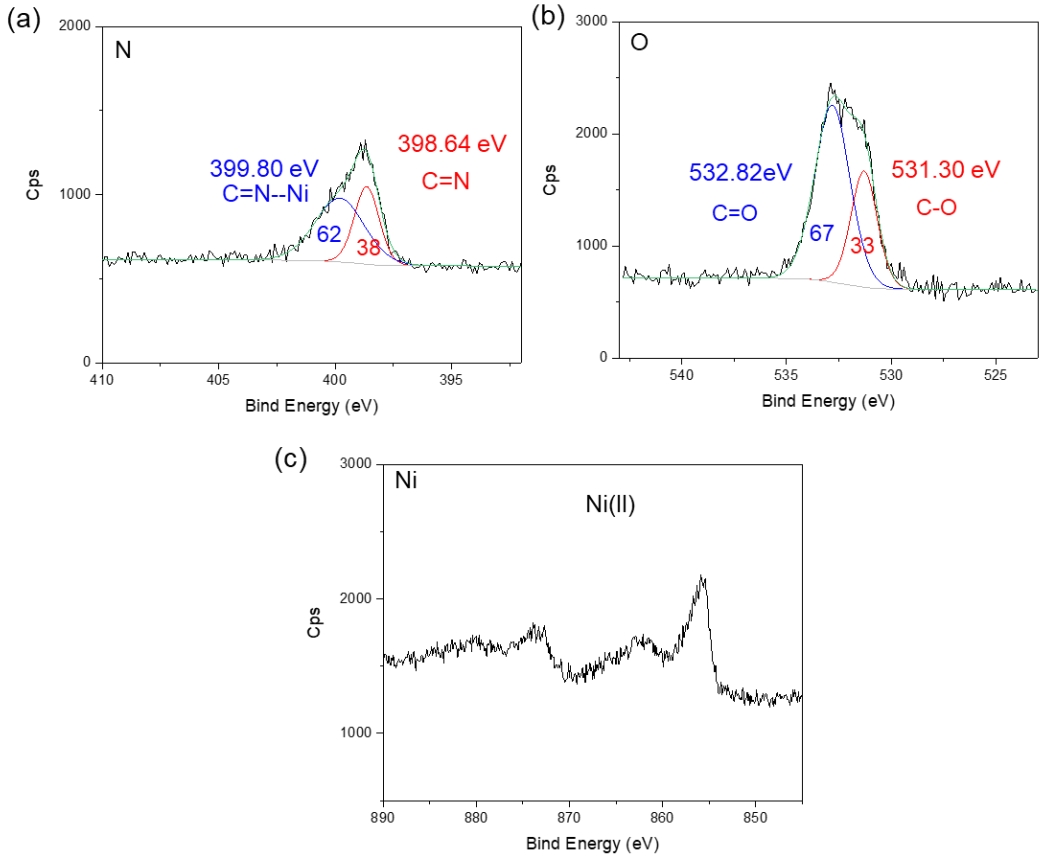

Figure S15. Deconvoluted XPS spectra of the **NiNPc-Ni**: (a) C1s, (b) N1s and (c) Ni2p. The black, grey, and green curve represent original data, background and the sum of the deconvoluted peaks, respectively. In (a) the blue curve corresponds to N(1s) in C=N-Ni and the red curve corresponds to C1s C=N-C. In (b) the red curve corresponds C-O and the blue curve corresponds to C=O.

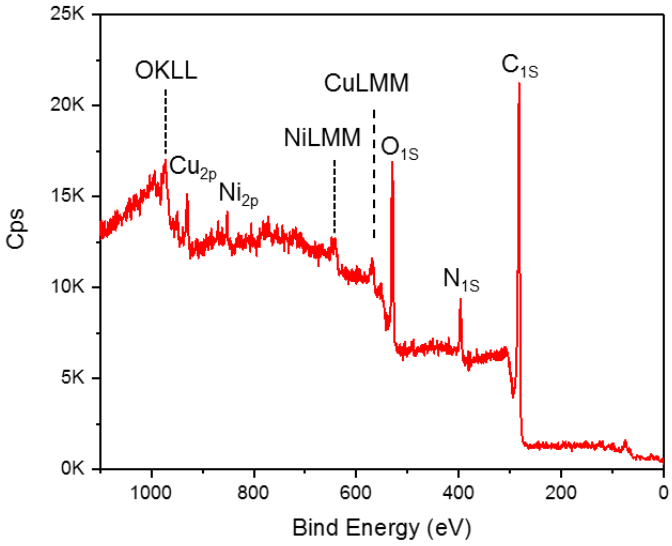

Figure S16. XPS survey spectrum of **NiNPc-Cu** showing C, N, O, Ni and Cu elements.

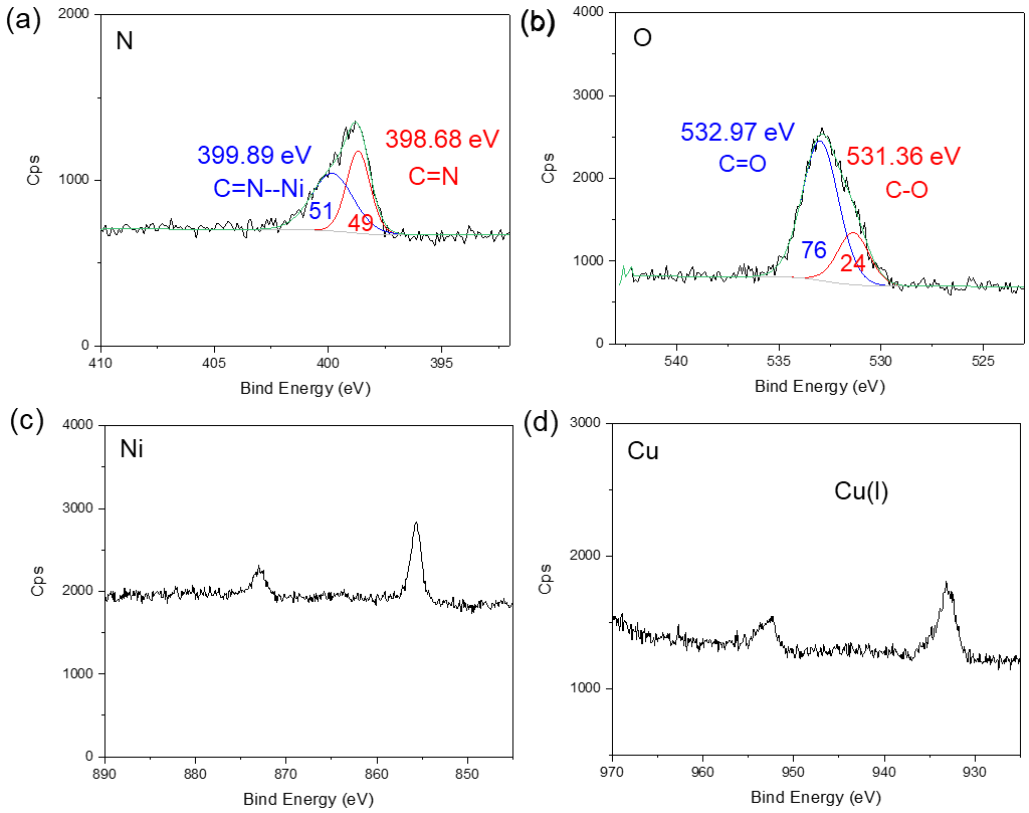

Figure S17. Deconvoluted XPS spectra of the **NiNPc-Cu**: (a) C1s, (b) N1s, (c) Ni2p, and (d) Cu2p. The black, grey, and green curve represent original data, background and the sum of the deconvoluted peaks, respectively. In (a) the blue curve corresponds to N(1s) in C=N···Ni and the red curve corresponds to C1s C=N-C. In (b) the red curve corresponds C-O and the blue curve corresponds to C=O.

The XPS spectra revealed the presence of C, O, and N, along with Ni and/or Cu elements in **NiPc-M** and **NiNPc-M** MOFs (**Figure S10, S12, S14,** and **S16**), which coincide with the desired elemental composition of these MOFs.

Oxidation state analysis of metal and ligand in NiPc-Ni. High-resolution scans of the Ni2p showed two peaks with binding energies of ~855.6 and ~873.2 eV (2p3/2 and 2p1/2 levels, respectively) with the presences characteristic satellite peaks (**Figure S11**), indicating the oxidation state of the Ni is +2. These results are consistent with the experimental data reported by Sheberla et al.[S4] and Dong et al.,[S5] where Ni in both Ni_3HITP_2 (HITP = 2,3,6,7,10,11-hexaiminotriphenylene) and Ni_3HTTP_2 (HTTP = 2,3,6,7,10,11-hexathioltriphenylene) showed +2 oxidation state. EPR spectrum of **NiPc-Ni** showed no visible peaks, which further supports the +2 oxidation state for Ni (**Figure S28**).

High-resolution scans of the O 1s region revealed two chemical environments with the peak with binding energies at 531.4 and 533.2 eV (**Figure S11**), which can be ascribed to two different O environment, C=O and C-O, respectively.[S6-7] The ratio of 48:52 further demonstrated that the ligand is likely in a (sq, sq, sq, sq) (sq=semiquinone) oxidation state, corresponding to a total charge of −4. Considering the theoretical ligand: metal ratio of 1:2, **NiPc-Ni** very likely has a charge neutral skeleton. High-resolution scans of the N 1s region further revealed two chemical environments with peaks found at 398.8 and 400.0 eV in a ratio of 47:53, which matches the presence of two different kinds of N atoms (Ni-coordinated and non-coordinated, in a 1:1 ratio) in the **NiPc** unit, suggesting the absence of large number of NH_4^+ acting as counter ions.

Oxidation state analysis of metal and ligand in NiPc-Cu. High-resolution scans of the Cu2p region produced two peaks with binding energies of ~933.1 and ~952.5 eV (2p3/2 and 2p1/2 levels, respectively) with very weak satellite peaks (**Figure S13)**. The lack of obvious satellite structure suggests the absence of Cu(II).[S8] The Cu 2p 2/3 peak near 933.1 eV matches well with the binding energy value of a typical Cu 2p 2/3 peak of Cu(I) compound, which means the Cu(II) ion have been reduced by the **NiPc** ligand during the formation of **NiPc-Cu.** The XPS data is consistent with results analyzed from the EPR spectrum of **NiPc-Cu,** which showed only weak peak at *g*=2.02, probably due to the small amount of paramagnetic Cu^{2+} (**Figure S29**).

High-resolution scans of the O 1s region revealed two chemical environments with the binding energies at 531.4 and 533.2 eV (**Figure S13**), which can be ascribed to two different O environments: C=O and C-O, respectively.[S6-7] The ratio of 74:25 further demonstrated that the ligand is likely in a (sq, sq, q, q) (q=quinone) oxidation state, corresponding to a total charge of −2 charge on the ligand. The relatively higher oxidation states of the **NiPc,** compared with that in

NiPc-Ni, may be caused by the stronger oxidation ability of Cu^{2+}. High-resolution scans of the N 1s region revealed two chemical environments with peaks found at 399.0 and 400.0 eV in a ratio of 50:50, which matches the presences of two different kinds of N atoms (Ni coordinated and non-coordinated, in a 1:1 ratio) in the **NiPc** unit, thus eliminating the possibility of NH_4^+ acting as counter ions. Combining the theoretical ligand: metal ratio of 1:2 and the above analysis, it is suggested that **NiPc-Cu** has a charge neutral skeleton with a general formula of (**NiPc**)$_1$Cu$_2$.

Oxidation state analysis of metal and ligand in NiNPc-Ni. High-resolution scans of the Ni2p peak two peaks with binding energies of ~855.6 and ~873.2 eV (2p3/2 and 2p1/2 levels, respectively) with their characteristic satellite peaks (**Figure S15**), indicating the oxidation state of the Ni is +2.

High-resolution scans of the O 1s region revealed two chemical environments with binding energies at 531.3 and 532.8 eV (**Figure S15**), which can be ascribed to two different O environments, C=O and C-O, respectively. The ratio of 67:33 demonstrated that the ligand is likely in oxidation state with sq:q=2:1, corresponding to −8/3 state. The combination of the Ni and **NiNPc** in a 2:1 ratio doesn't afford a charge neutral framework, which suggests the presence of acetate oy hydroxide as the negative counter ions.

Oxidation state analysis of metal and ligand in NiNPc-Cu. High-resolution scans of the Cu2p region showed two peaks with binding energies of ~933.1 and ~952.8 eV (2p3/2 and 2p1/2 levels, respectively) with very weak satellite peaks (**Figure S17)**. The lack of obvious satellite structure suggests the absence of Cu(II).[S8] The Cu 2p 2/3 peak near 933.1 eV matches well with the binding energy value of a typical Cu 2p 2/3 peak of Cu(I) compound. Similar to the situation in **NiPc-Ni**, Cu(II) ions were likely reduced by the **NiNPc** ligand during the formation of **NiPc-Cu**. In addition, EPR showed very weak peak (g=2.03) likely originating d from the metal centered radical of Cu^{2+} (**Figure S31**), consistent with the scarcity of Cu^{2+} in **NiNPc-Cu.**

High-resolution scans of the O 1s region revealed two chemical environments with binding energies at 531.4 and 533.0 eV (**Figure S17**), which can be ascribed to two types of oxygen atoms, C=O and C-O, respectively.[S6-7] The ratio of 52:48 demonstrated that the ligand is likely in a (sq, sq, sq, sq) oxidation state, corresponding to an overall charge of −4. High-resolution scans of the N 1s region revealed two chemical environments with the peak positions found at 398.8 and 400.0 eV in a ratio of 53:47, which matched the presence of two different kinds of N atoms (Ni coordinated and non-coordinated, in a 1:1 ratio) in the **NiNPc** unit, eliminating the possibility of NH_4^+ acting as counter ions. Combining the theoretical ligand: metal ratio of 1:2 and the above analysis, **NiNPc-Cu** has a charge neutral skeleton with a general formula of (**NiNPc**)$_1$Cu$_2$, which is the same with

NiPc-Cu.

5. Elemental Analysis

Elemental analyses, including C, H, N were performed by Atlantic Microlab inc. using combustion method by automatic analyzers. The metal contents (Ni, Cu) were analyzed by ICP-MS. The results are listed below.

Table S1. Elemental analysis of **NiPc-Ni**.

Sample	Element	Theoretical[1]	Found
NiPc-Ni	C	47.54	36.30
	H	1.00	2.76
	N	13.96	15.20
	Ni	21.78	20.45

[1]Based on the formula (**NiPc**)$_1$Ni$_2$.

Table S2. Elemental analysis of **NiPc-Cu**.

Sample	Element	Theoretical[1]	Found
NiPc-Cu	C	46.97	39.60
	H	0.99	2.06
	N	13.69	11.47
	Ni	7.17	5.68
	Cu	15.53	13.84

[1]Based on the formula (**NiPc**)$_1$Cu$_2$.

Table S3. Elemental analysis of **NiNPc-Ni**.

Sample	Element	Theoretical[1]	Found
NiNPc-Ni	C	57.15	59.02
	H	1.60	4.29
	N	11.11	9.49
	Ni	17.45	15.54

[1]Based on the formula (**NiNPc**)$_1$Ni$_2$

Table S4. Elemental analysis of **NiNPc-Cu**.

Sample	Element	Theoretical[1]	Found
NiNPc-Cu	C	56.61	54.88
	H	1.58	3.73
	N	11.00	9.02
	Ni	5.76	4.88
	Cu	12.48	9.17

[1]Based on the formula (**NiNPc**)$_1$Cu$_2$.

6. Structure Analysis by Computational Study and Powder X-ray Diffraction

To build the crystal structure of **NiPc-Ni** and **NiPc-Cu**, model complexes composed of one phthalocyanine unit and four metal catecholate units were built. Their structures are shown in **Figure S18**. These model complexes were optimized by using B3LYP density-functional theory method with a basis set of 3-21G. The optimized structures of the model complexes were imported into Materials Studio. The initial crystal structures were constructed starting with a unit cell with the space group P1 with lattice parameters of $\alpha=\beta=\gamma=90$ °. The *a* and *b* values were estimated from the size of the model complexes. The *c* values were estimated according to the distance between the metal center of phthalocyanine unit and were chosen from the values calculated from the pXRD. The symmetries of the initial structures were then found and imposed to a higher symmetry of P4/mmm with a threshold of 0.01 Å pm (fine level). The crystal structure of **NiNPc-Ni** and **NiNPc-Cu** were also built using a similar approach.

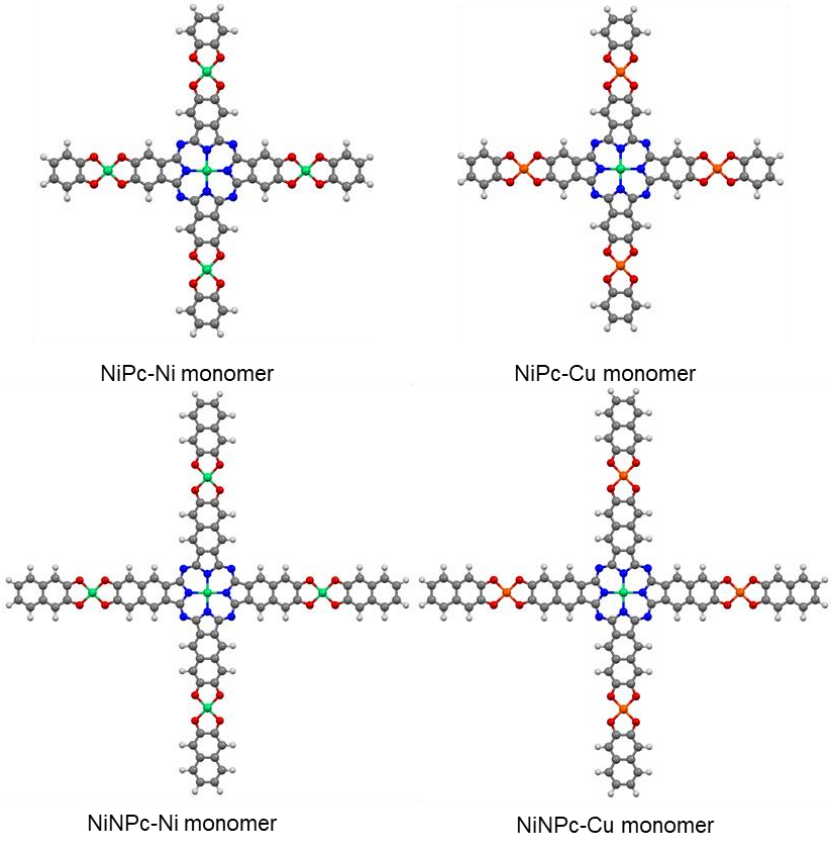

Figure S18. Model complexes used for the construction of the initial MOF structures.

The geometry optimization, including energy minimization with cell parameters, were performed by using CASTEP module in Materials Studio with Perdew−Burke−Ernzerhof (PBE) generalized gradient approximation (GGA). The total energy change was set to less than 10^{-5} eV

and the magnitude of the largest force acting on the atoms was set to less than 0.03 eV A^{-1}. The cut-off energies were set at 500.0 eV. Calculation of the simulated powder diffraction patterns were performed by Materials Studio Reflex Plus Module. The optimized crystal structure the four MOFs with their lattice parameters are shown in **Figure S19**. Modeling of the staggered structures was performed in a similar manner but with the space group I4/mmm (**Figure S20**).

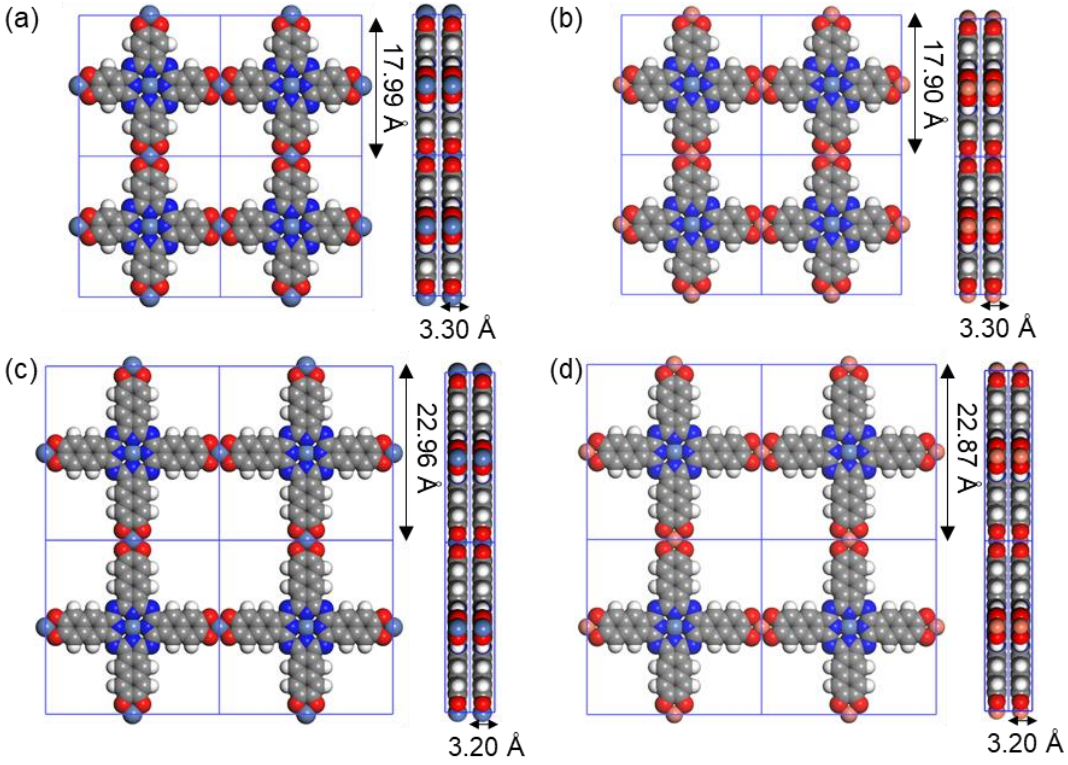

Figure S19. Views from *z* and *x* axes of modeled MOF crystal structures with eclipsed packing mode for (a) **NiPc-Ni**; (b) **NiPc-Cu**; (c) **NiNPc-Ni**; (d) **NiNPc-Cu**.

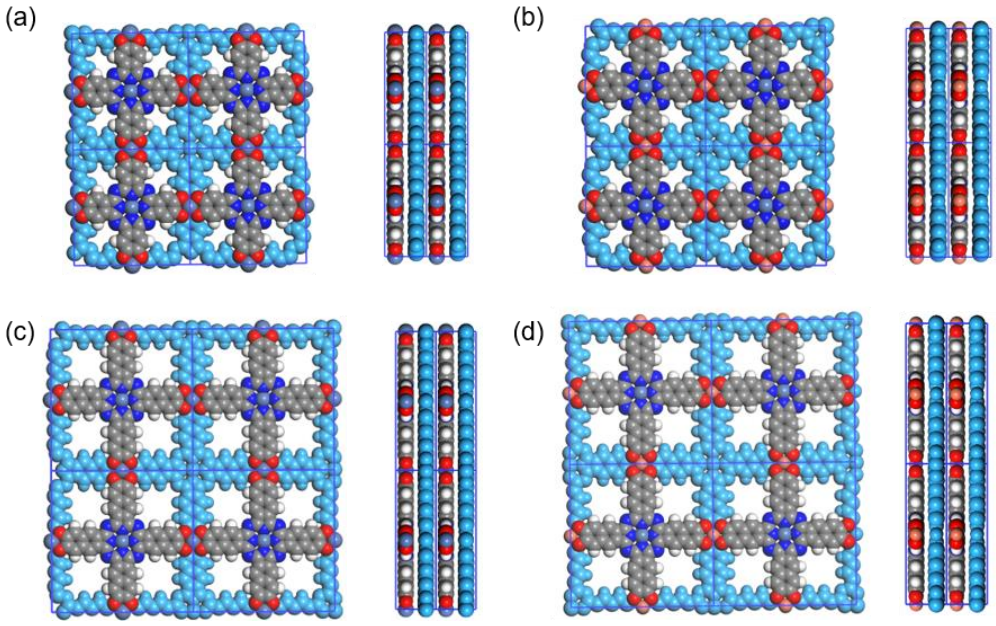

Figure S20. Views from *z* and *x* axes of modeled MOF crystal structures with staggered packing for (a) **NiPc-Ni**; (b) **NiPc-Cu**; (c) **NiNPc-Ni**; (d) **NiNPc-Cu**.

Powder X-ray diffraction (PXRD) data of **NiPc-Cu**, **NiPc-Ni**, **NiNPc-Cu** and **NiNPc-Ni** were collected using a Rigaku sixth generation MiniFlex X-ray diffractometer. Cu Kα radiation (λ = 1.5406 Å; 600 W, 40 kV, 15 mA) was focused using a planar Göbel mirror riding the Kα line.

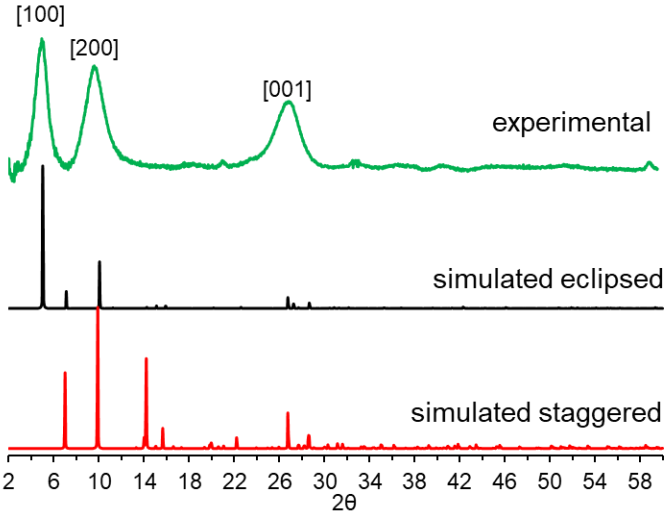

Figure S21. PXRD spectra for experimental (green line) and simulated models in eclipsed (black line) and staggered packing (red line) of **NiPc-Ni**.

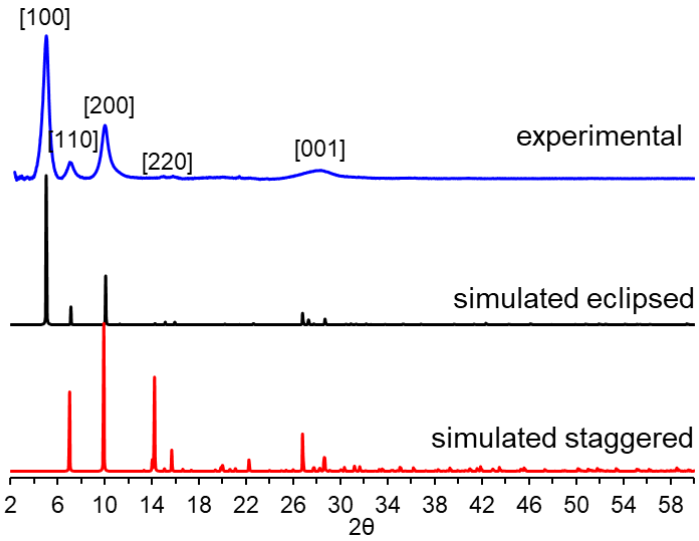

Figure S22. PXRD spectra for experimental (blue line) and simulated models in eclipsed (black line) and staggered packing (red line) of **NiPc-Cu**.

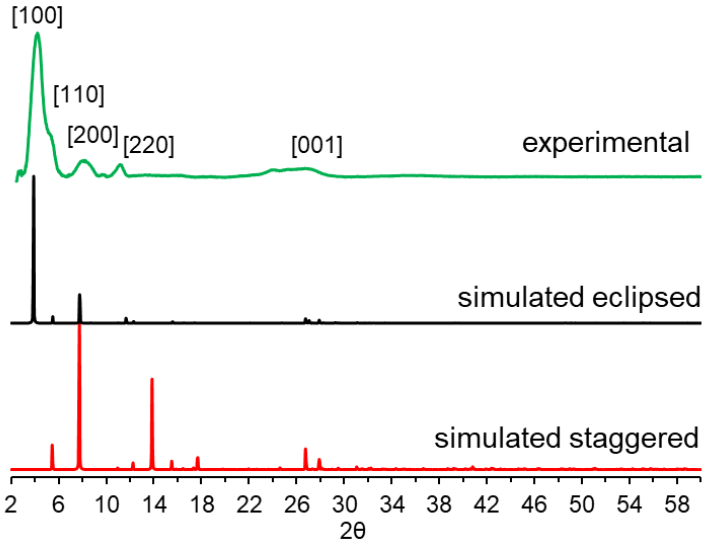

Figure S23. Experimental (blue line) and simulated PXRD pattern (black line) of **NiNPc-Ni**.

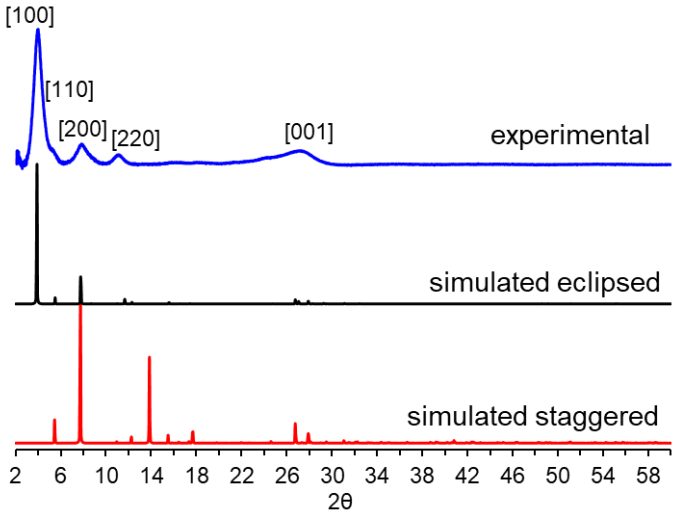

Figure S24. PXRD spectra for experimental (blue line) and simulated models in eclipsed (black line) and staggered packing (red line) of **NiNPc-Cu**.

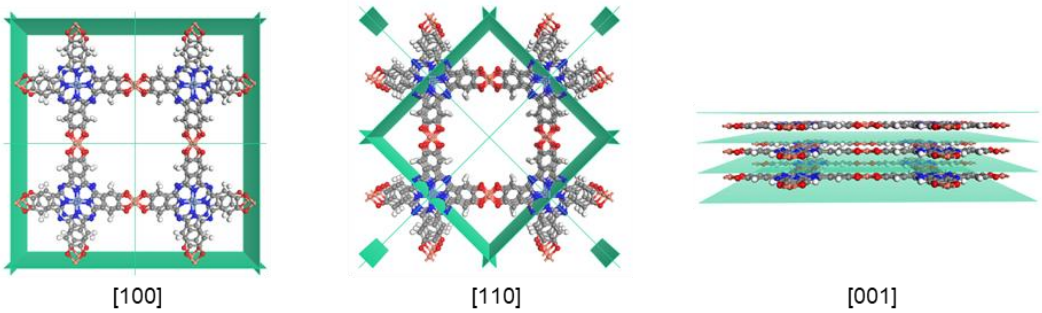

Figure S25. Representation of the planes [100], [110] and [001] in the crystal structure of MOFs demonstrated by using **NiPc-Cu** as an example.

7. Computational Study of the Electronic Properties

For computational study of electronic properties, including band structures, density of states, the functional GGA with PBE was employed with an energy cutoff set at 500 eV. The Brillouin zones were sampled using a 2 × 2 × 4 k-point mesh in the Monkhorst – Pack scheme.

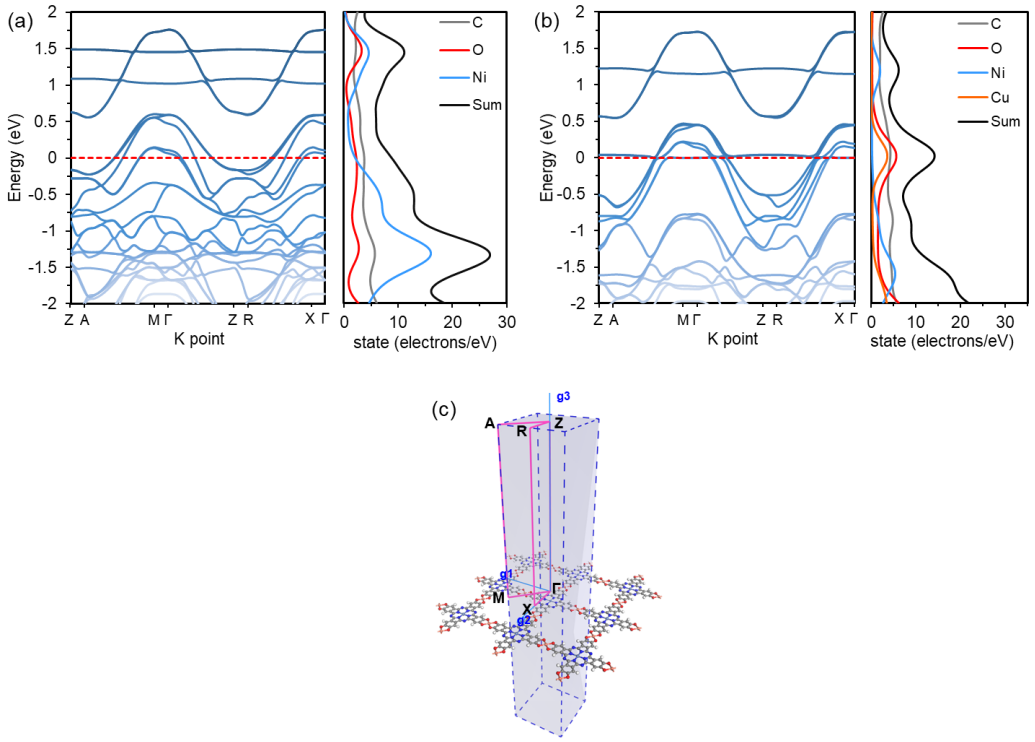

Figure S26. Calculated electronic band structure (left) and density of state (right) for (a) **NiPc-Ni** and (b) **NiPc-Cu**, respectively. (c) Corresponding first Brillouin zone and high-symmetry K-points.

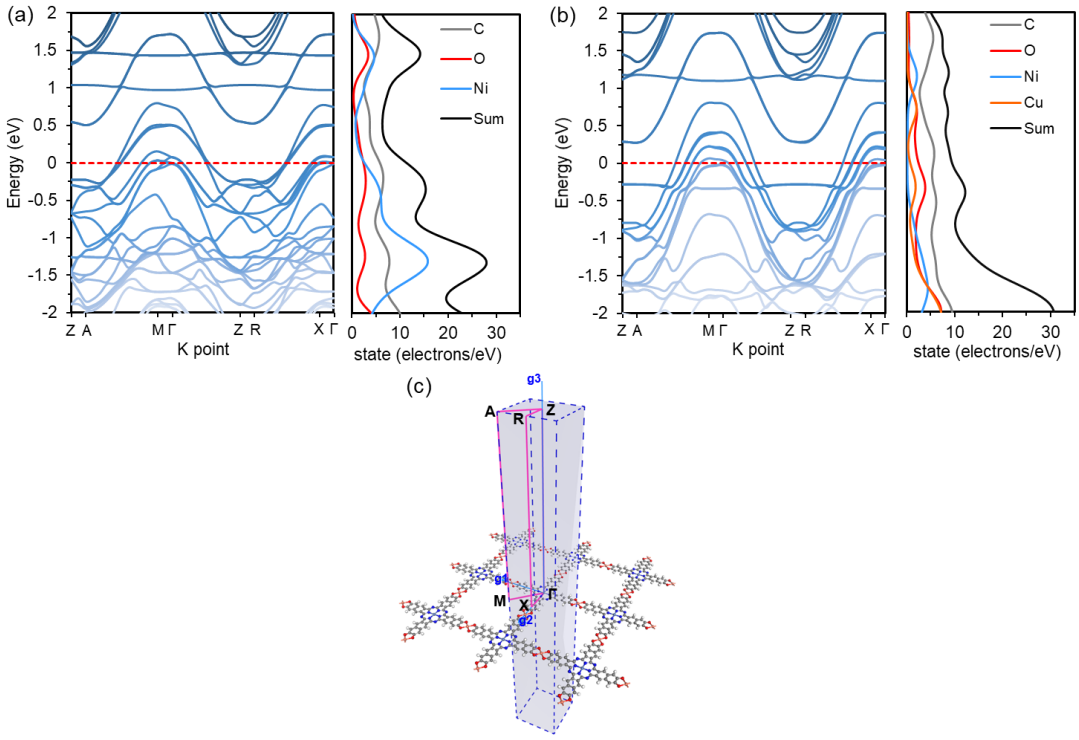

Figure S27. Calculated electronic band structure (left) and density of states (right) for (a) **NiNPc-Ni** and (b) **NiNPc-Cu**, respectively. (c) Corresponding first Brillouin zone and high-symmetry K-points.

DFT electronic band structure calculations suggested that bulk **NiPc-M** and **NiNPc-M** should be metallic. Both of **NiPc-M** and **NiNPc-M** MOFs exhibited dispersed electronic band structures that cross the Fermi level. The Dirac bands cross the Fermi level in both A−M and Γ−Z directions and have wide band dispersions of approximate 0.8-1.0 eV (**Figure S26a-b** and **Figure S27a-b**). Density of states analysis showed that considerable contributions were from the metal linkers, C, and O orbitals near the Fermi level, indicating the high degree of in-plane and out-of-plane π conjugation for these materials.

The high symmetry points in the first Brillouin zone are shown in **Figure S26c** and **Figure S27c**. In **NiPc-M** and **NiNPc-M,** bands cross the Fermi level in the out-of-plane direction, including A−M, Γ−Z, R−X directions, which indicates the metallic nature of materials. Because no bands cross the Fermi level through the in-plane directions (Z−R and X−Γ), the bulk materials are expected to be metallic in the *c* directions and semiconducting in the *ab* direction, suggesting that a dominant mechanism for conductivity in these **MPc** based MOFs maybe through conductive pathways along the *c*-axis.[S9] This electronic property is different from the M_3HIB_2 (M=Ni, Cu, HIB = hexaiminobenzene)[S10] and nickel bis(dithiolene) based MOFs[S11] where the in-plane charge transport is predicated to be more favorable than out-of-plane charge transport, and is similar with that of cobalt triphenylenehexathiolate framework where the out-of-plane transport is believed to be the dominant conductive pathway.[S9] As demonstrated above, **NiPc-M** and **NiNPc-M** MOFs adopt eclipsed stacking modes, which endows the stacking structures and alignment of the π-conjugated **NiPc** and **NiNPc** units, facilitating **NiPc**-on-**NiPc** (or **NiNPc**-on-**NiNPc**) and metal-on-metal pathways within 2D stacks. The out-of-plane charge-transport property is consistent with those found in the phthalocyanine-[S12-13] and porphyrin-based COFs,[S14-15] which usually exhibited high carrier mobility along the direction of the stacking due to the formation of periodic π-columns.

8. Electron Paramagnetic Resonance (EPR) Spectroscopy

EPR spectra were collected on a Bruker BioSpin Gmbh spectrometer equipped with a standard mode cavity. For each sample, about 2 mg material was used. The samples were flushed with N_2 for 15 minutes and then sealed in the EPR tube under N_2 atmosphere. The EPR spectrum was collected under liquid nitrogen temperature (77 K) with the parameters listed in the **Table S5**. **NiPc** and **NiNPc** ligand showed very intense peaks at g = 1.991 and 1.989, respectively, which are probably due to the adsorption of oxygen molecules (**Figure S28-S31**) or the existence of the partially oxidized species. **NiPc-Ni** showed **EPR** signal at g=1.988 from the ligand centered radical (**Figure S28**). **NiPc-Cu** showed relatively weaker metal centered EPR signal (g=2.021) compared with the ligand **NiPc (Figure S29)**. **NiNPc-Ni** showed peak at g=1.996 which originated from the

radial centered on the **NiNPc** ligand (**Figure S30**). In the EPR spectrum of **NiNPc-Cu**, peaks from the both the metal-centered (g=2.030) and ligand-centered radical (g=1.986) were shown (**Figure 31**).

Table S5. Parameters of EPR for ligands and MOFs.

Sample	sweep width/G	center field/G	modulation amplitude/G	microwave frequency/GHz	microwave power/mW
NiPc	2000	3400	4	9.673	0.0002026
NiNPc	2000	3400	4	9.658	0.0002026
NiPc-Ni	3000	3400	4	9.692	0.0002026
NiPc-Cu	3000	3400	4	9.668	0.0002017
NiNPc-Ni	3000	3400	4	9.712	0.0002026
NiNPc-Cu	3000	3400	4	9.668	0.0002017

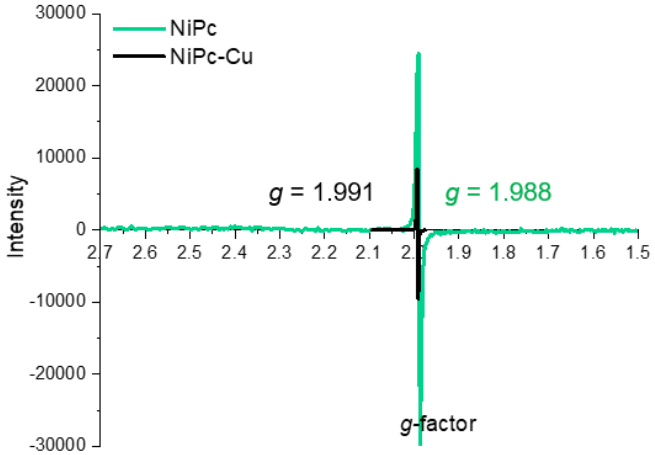

Figure S28. EPR spectra (77 K) of **NiPc** ligand (black) and **NiPc-Ni** MOF (green).

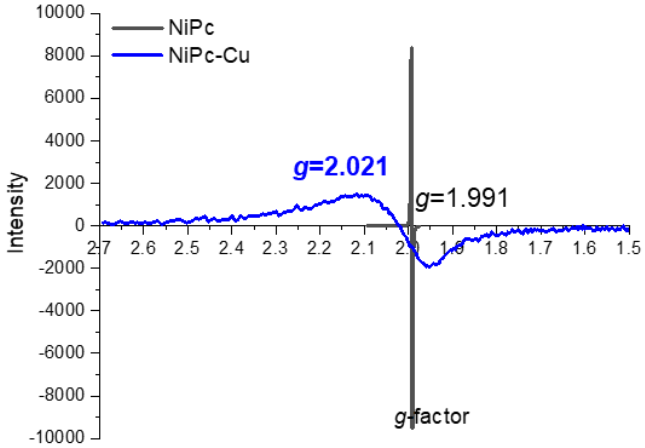

Figure S29. EPR spectra (77 K) of **NiPc** ligand (black) and **NiPc-Cu** MOF (blue).

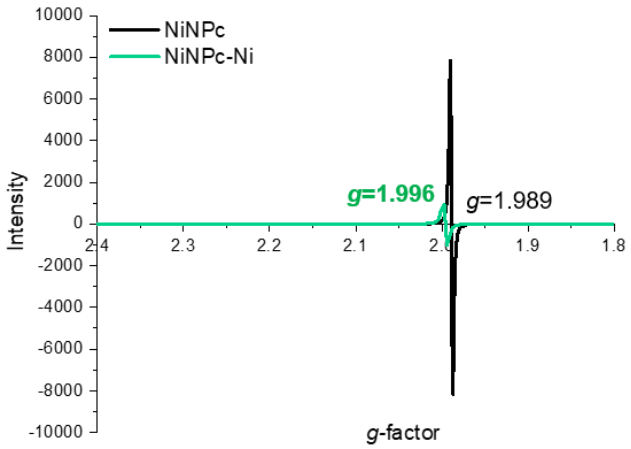

Figure S30. EPR spectra (77 K) of **NiNPc** ligand (black) and **NiNPc-Ni** MOF (green).

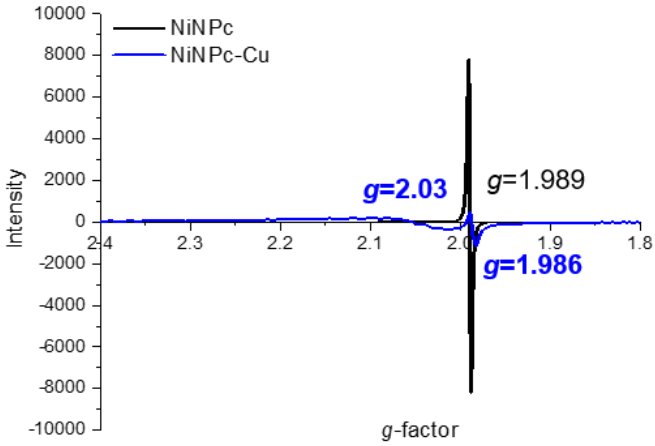

Figure S31. EPR spectra (77 K) of **NiNPc** ligand (black) and **NiNPc-Cu** MOF (blue).

9. SEM and TEM

Scanning electron microscopy of the MOFs **NiPc-Ni, NiPc-Cu, NiNPc-Ni,** and **NiNPc-Cu** were obtained using a Hitachi TM3000 SEM. The material was pressed onto carbon conductive tape that was attached to the aluminum plate. The images were taken at a 10 mm working distance using a 15 kV beamline in a to 10^{-6} torr vacuum chamber.

Transmission electron microscopy was carried out in a Tecnai F20ST FEG TEM instrument. The sample was prepared by drop casting an acetone suspension (0.5 mg in 5 mL) of the MOFs onto a copper grid (300 mesh, 3.0 mm O.D). An operating voltage of 120 kV was used for imaging.

Energy dispersive X-Ray spectroscopy was collected using SDD X-ray microanalysis system with Octane Pro 10 sq. mm detector and TEAM software.

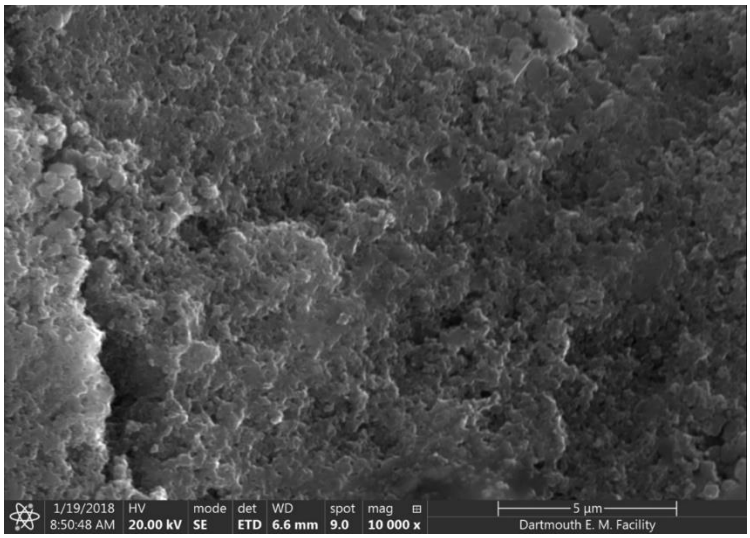

Figure S32. SEM image of **NiPc-Ni**.

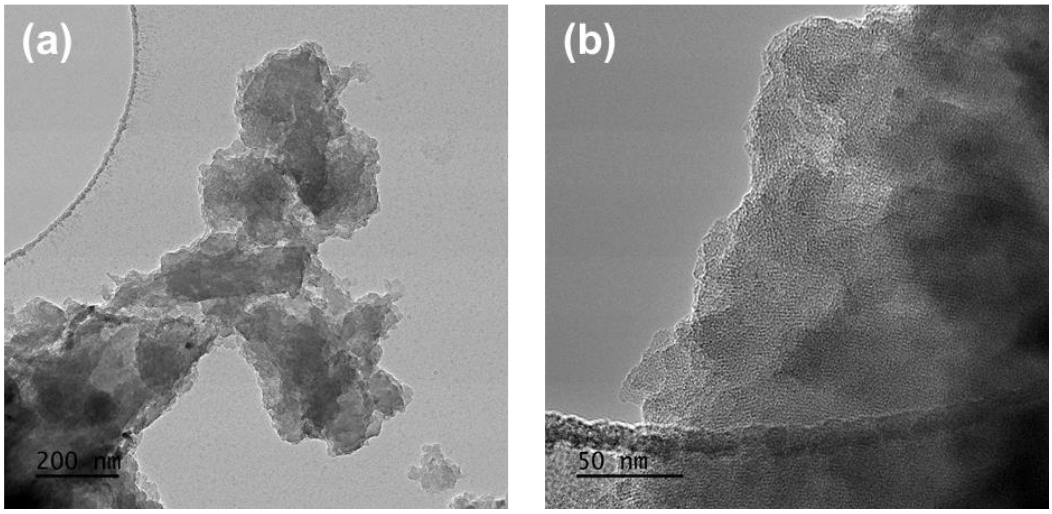

Figure S33. TEM image of **NiPc-Ni** at different magnifications.

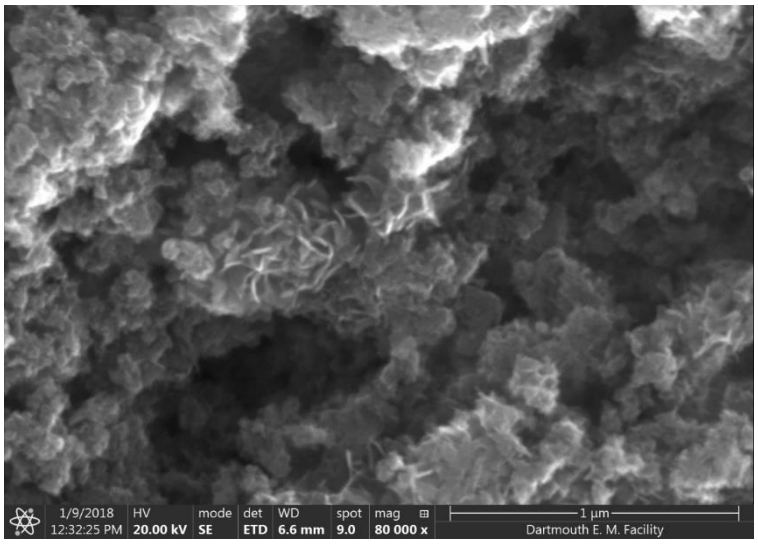

Figure S34. SEM image of **NiPc-Cu**.

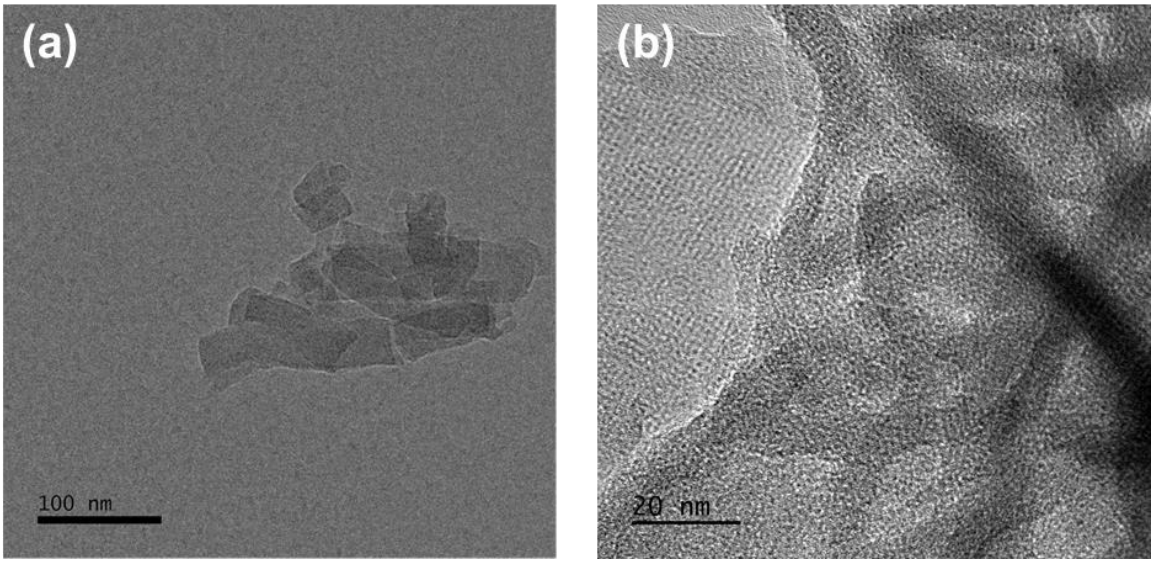

Figure S35. TEM image of **NiPc-Cu** at different magnifications.

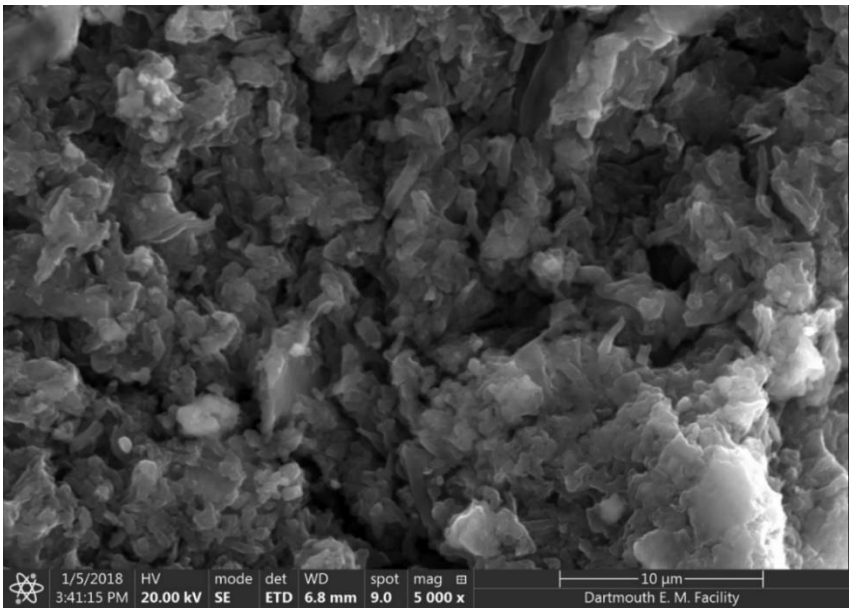

Figure S36. SEM image of **NiNPc-Ni**.

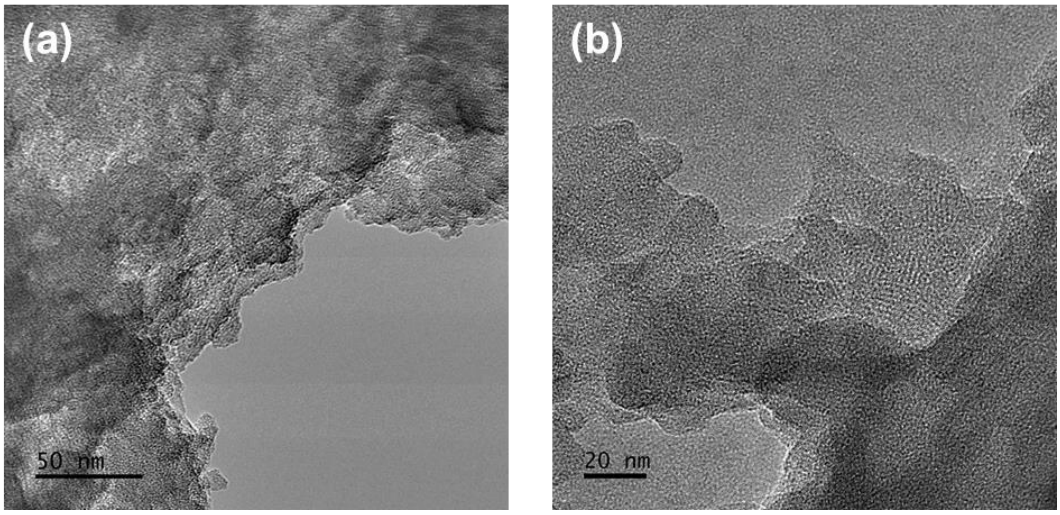

Figure S37. TEM image of **NiNPc-Ni** at different magnifications.

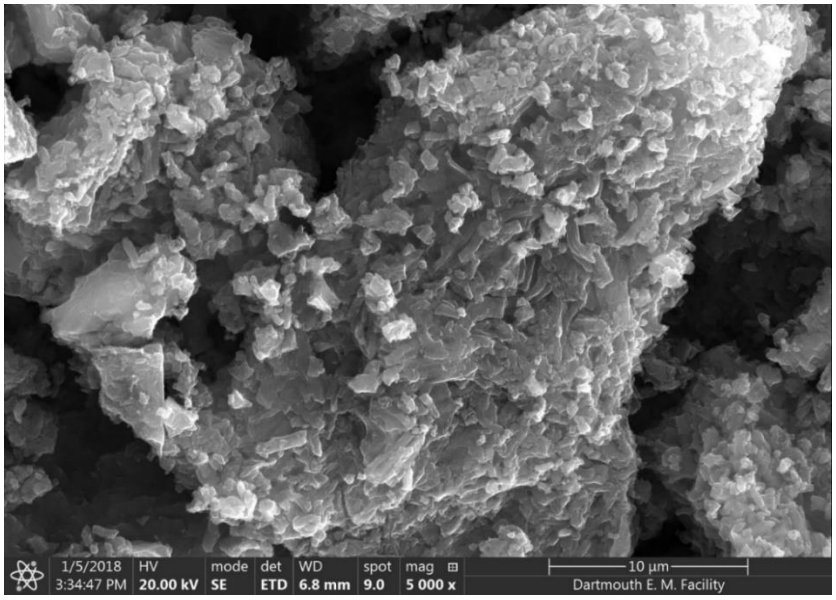

Figure S38. SEM image of **NiNPc-Cu**.

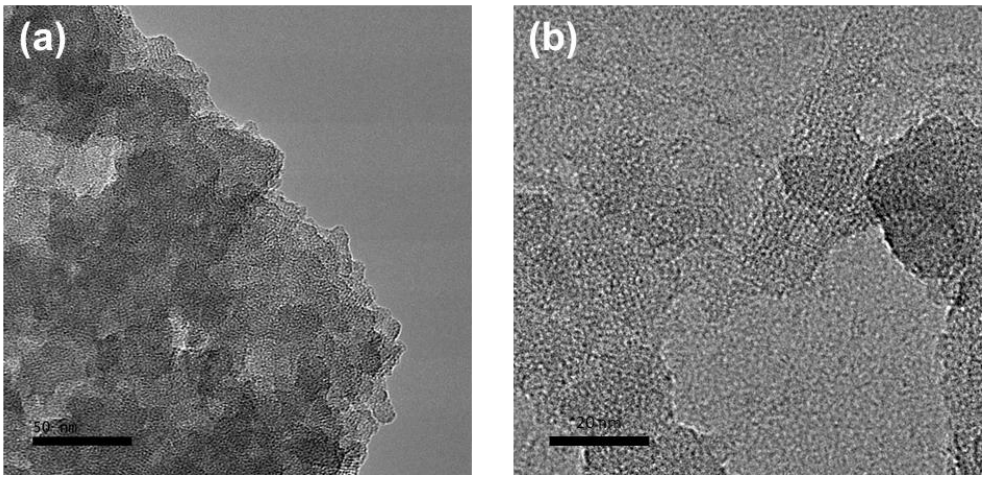

Figure S39. TEM image of **NiNPc-Cu** at different magnifications.

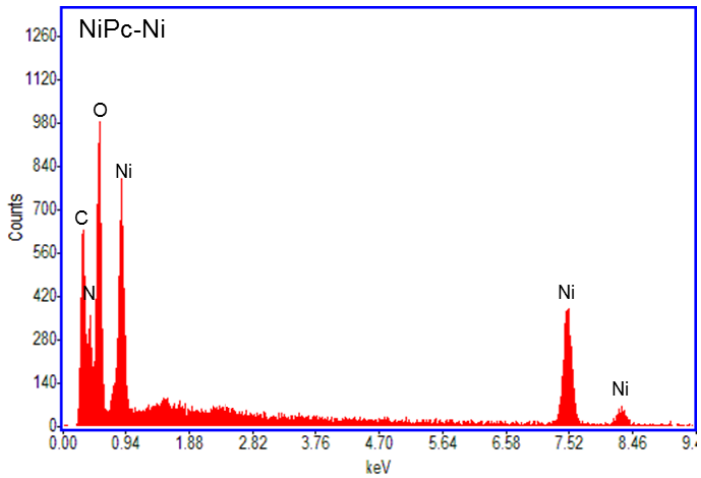

Figure S40. EDAX spectrum of **NiPc-Ni**.

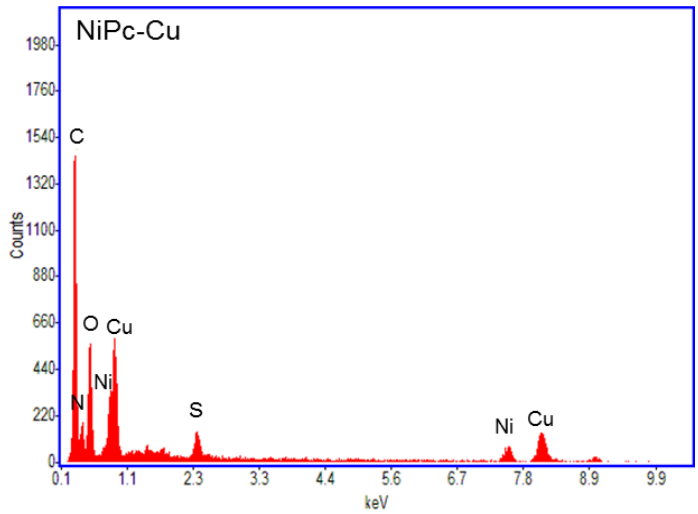

Figure S41. EDAX spectrum of **NiPc-Cu**.

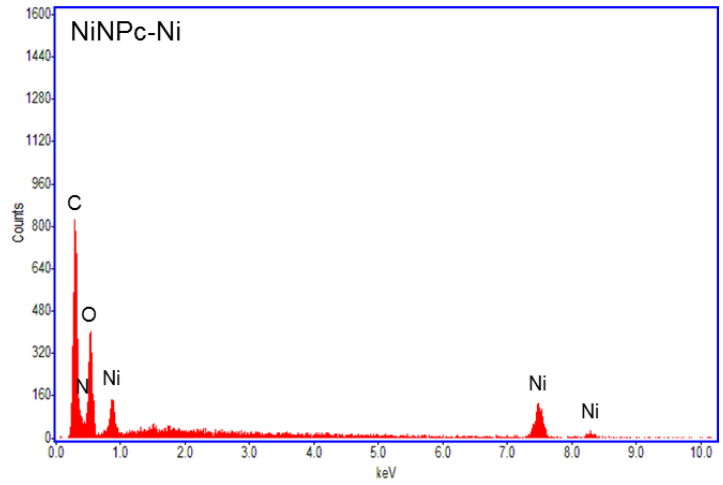

Figure S42. EDAX spectrum of **NiNPc-Ni**.

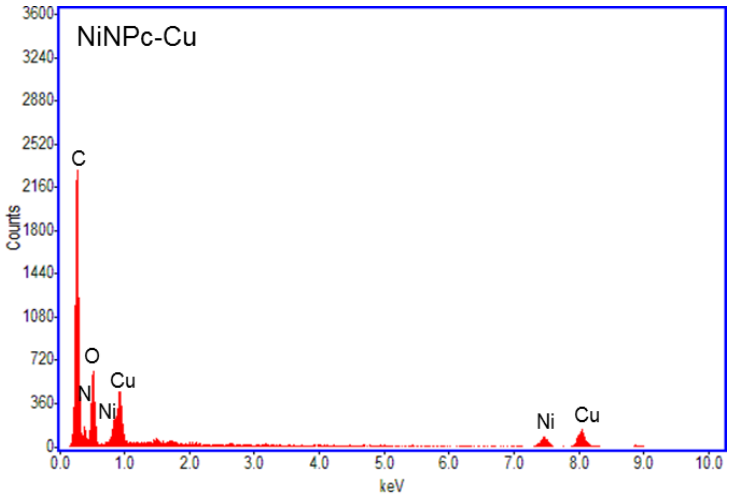

Figure S43. EDAX spectrum of **NiNPc-Cu**.

10. Brunauer–Emmett–Teller (BET) Analysis

In order to assess the porosity of the MOFs, gas adsorption measurements were performed on an ASAP Plus 2020 (Mircromeritics, Norcross, Georgia) 3FLEX instrument with N_2 at 77K. To remove the residual high boiling point solvent used in the synthesis of the MOFs, the samples of MOFs were activated by soaking in acetone for 3 days during which the acetone was changed every 24 hours. The samples were then dried in the oven under vacuum (20 mTorr, 65 °C for 24 hours). Before gas adsorption measurements, the samples were degassed under vacuum at 80 °C for 12 hours. For BET calculations, a full isotherm with a fitting range of 0 to 0.3 P/P_0 was used. The Brunauer-Emmett-Teller (BET) surface areas for the four MOFs are listed below.

Table S6. BET surface areas of the MOFs.

	NiPc-Ni	NiPc-Cu	NiNPc-Ni	NiNPc-Cu
BET (m^2/g)	101	284	174	267

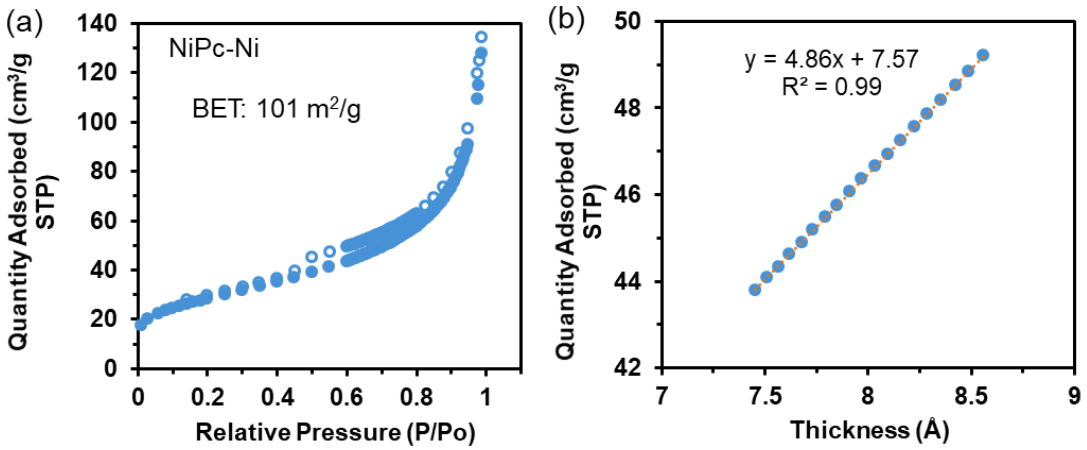

Figure S44. (a) Nitrogen sorption curves (filled circles: adsorption, open circles: desorption, STP=standard temperature pressure) and (b) *t*-Plot for nitrogen adsorbed at 77 K by activated **NiPc-Ni**. The BET surface area by the gas adsorption analysis is 101 m^2/g. The external surface area is 81 m^2/g and the micropore area is 20 m^2/g.

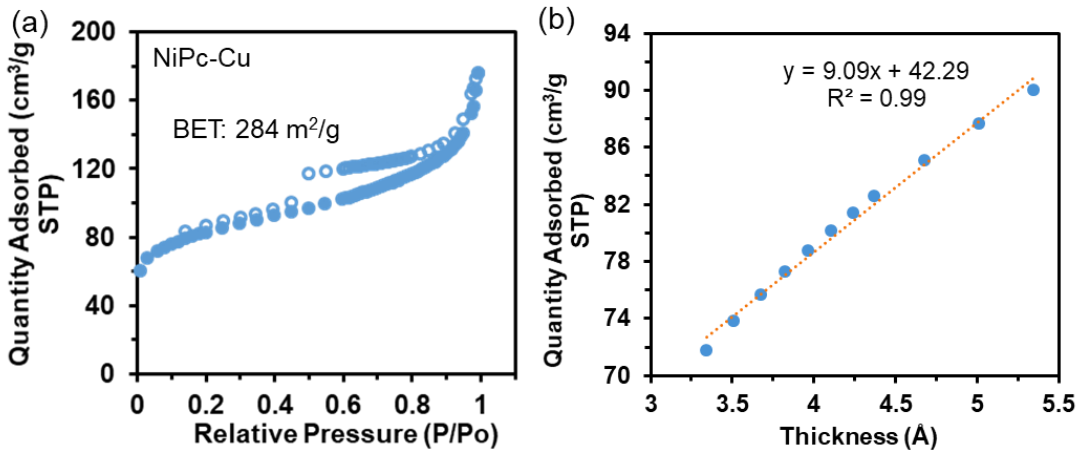

Figure S45. (a) Nitrogen sorption curves (filled circles: adsorption, open circles: desorption, STP=standard temperature pressure) and (b) *t*-Plot for nitrogen adsorbed at 77 K by activated **NiPc-Cu**. The BET surface area by the gas adsorption analysis is 284 m^2/g. The external surface area is 143 m^2/g and the micropore area is 141 m^2/g.

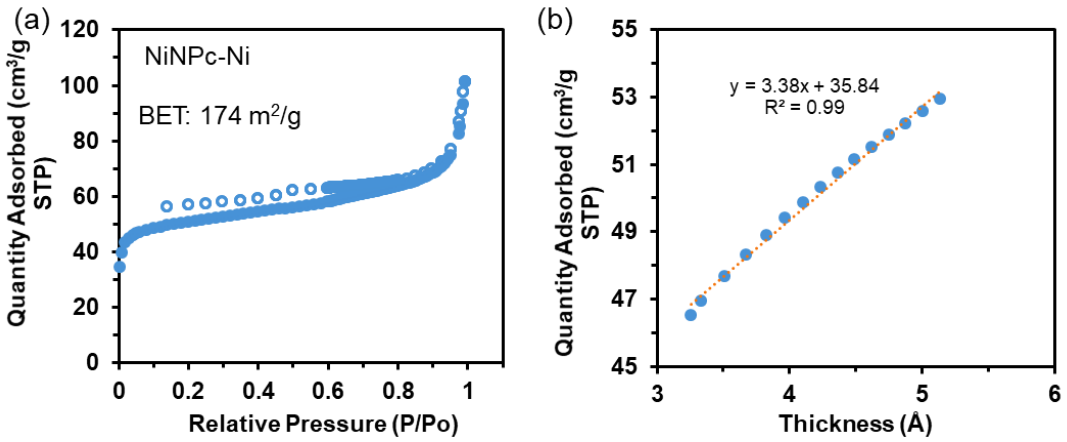

Figure S46. (a) Nitrogen adsorption curves (STP=standard temperature pressure) and (b) *t*-Plot for nitrogen adsorbed at 77 K by acidified material **NiNPc-Ni**. The BET surface area by the gas adsorption analysis is 174 m^2/g. The external surface area is 52 m^2/g and the micropore area is 152 m^2/g.

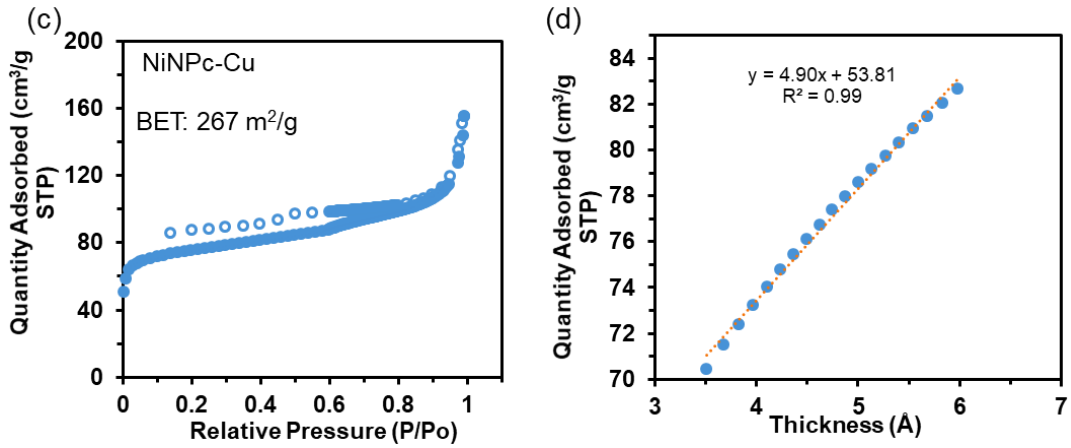

Figure S47. (a) Nitrogen adsorption curves (STP=standard temperature pressure) and (b) *t*-Plot for nitrogen adsorbed at 77 K by acidified material **NiNPc-Cu**. The BET surface area by the gas adsorption analysis is 267 m^2/g. The external surface area is 76 m^2/g and the micropore area is 191 m^2/g.

11. Thermal Gravimetric Analyses (TGA)

Thermal gravimetric analysis was performed using a TA Instruments TGA Q150 with a 40 ^oC/min ramp from room temperature to 850 ^oC.

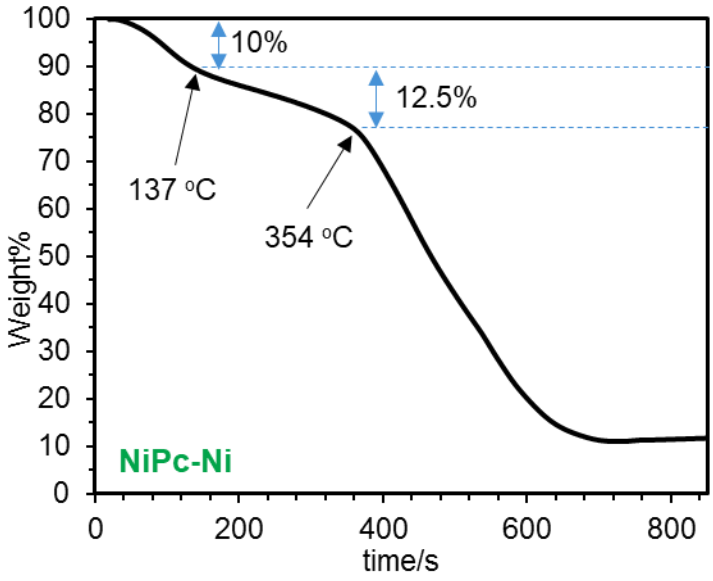

Figure S48. TGA curve of **NiPc-Ni**.

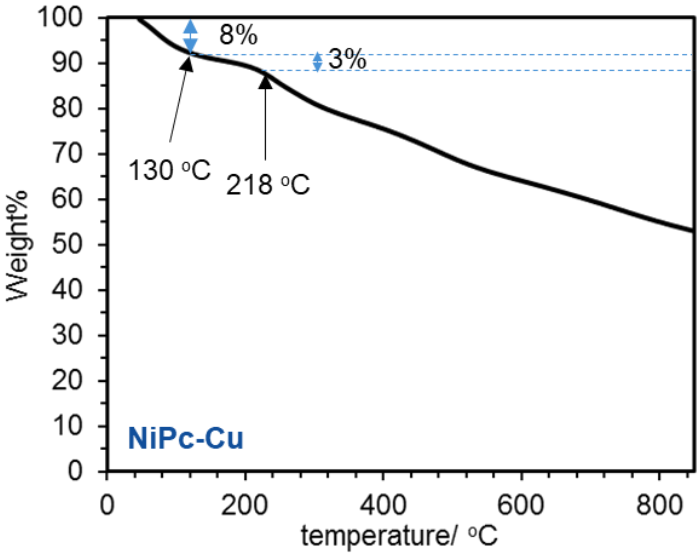

Figure S49. TGA curve of **NiPc-Cu**.

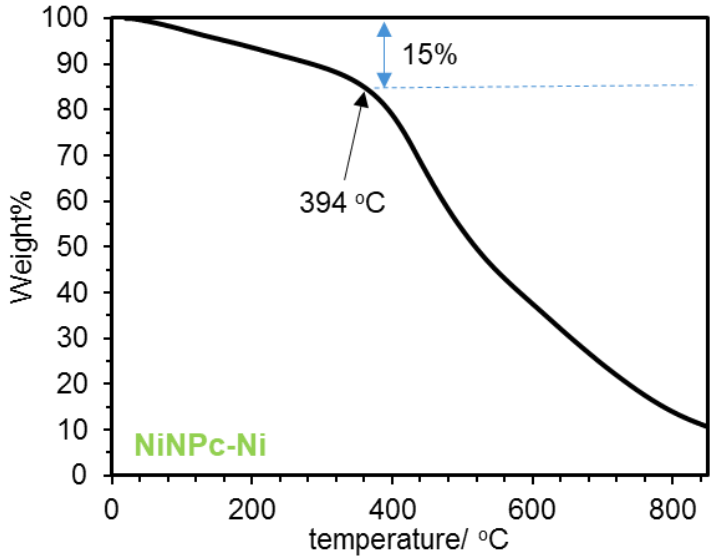

Figure S50. TGA curve of **NiNPc-Ni**.

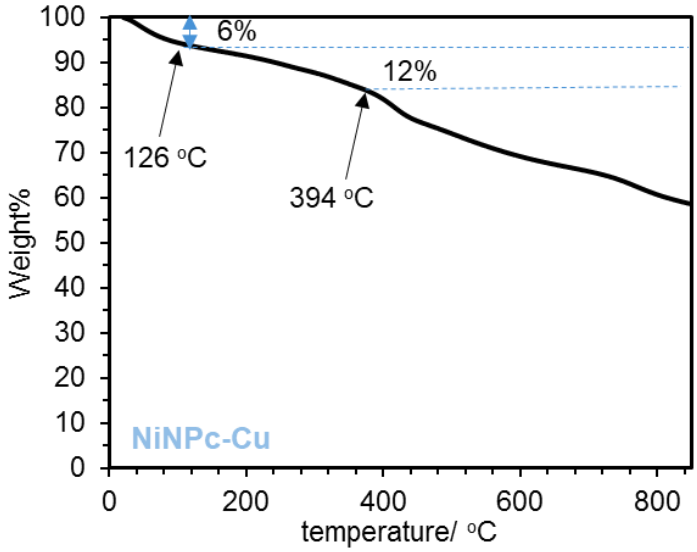

Figure S51. TGA curve of **NiNPc-Cu**.

12. Measurements of Conductivity

To make a pressed pellet, 50 mg of the MOF sample was put into a 6 mm inner-diameter split sleeve pressing die and pressed for 5 min under a pressure of approximately 1000 psi. A Signatone tungsten carbide four-point linear probe was employed to collect bulk conductivity measurements of the MOFs with a space between tips of 1.25 mm. We calculated the bulk conductivity measurements (S/cm) using **Equation S1**. Herein, I (A) is current, V is the voltage of cross the probes, s (cm) is distance of between the probes (1.25 mm), F (unitless) is the correction factor accounting for the diameter and thickness of the pellet.[S16-17]

$$\sigma = \frac{I}{V}\frac{1}{2\pi sF} \qquad \textbf{(S1)}$$

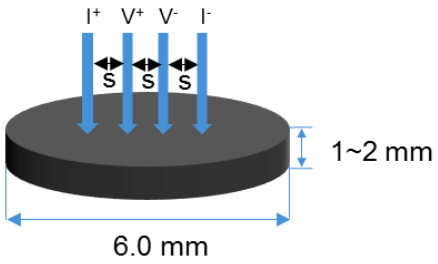

Figure S52. Representation of configuration for the measurement of conductivity by four-point probe method.

Table S7. Conductivity of the MOF measured by four-point probe method.

MOF	NiPc-Ni	NiPc-Cu	NiNPc-Ni	NiNPc-Cu
σ (S/cm)	7.22×10^{-4}	1.43×10^{-2}	1.78×10^{-2}	3.13×10^{-2}

13. Gas Sensing Experiments

13.1. Fabrication of Gas Sensors

1-4 mg of MOF samples was dispersed in 1 mL of deionized water. The mixture was then sonicated for 30 minutes and a homogeneous suspension was obtained. 10 µL of the suspension was drop casted onto interdigitated gold electrodes with 5 µm gaps (part NO. G-IDEAU5, purchased form Metrohm) (**Figure S53**), which was then allowed to dry in the air under room temperature in a dark area for about 18 hours before use.

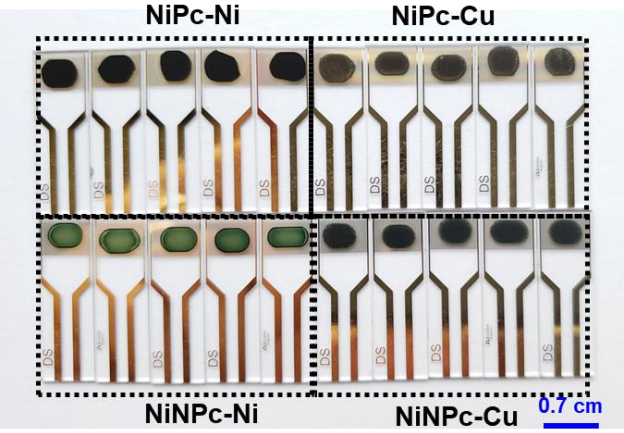

Figure S53. Photograph of chemiresistive devices made by drop casting the suspension of MOFs in water onto 5 µm interdigitate gold electrodes.

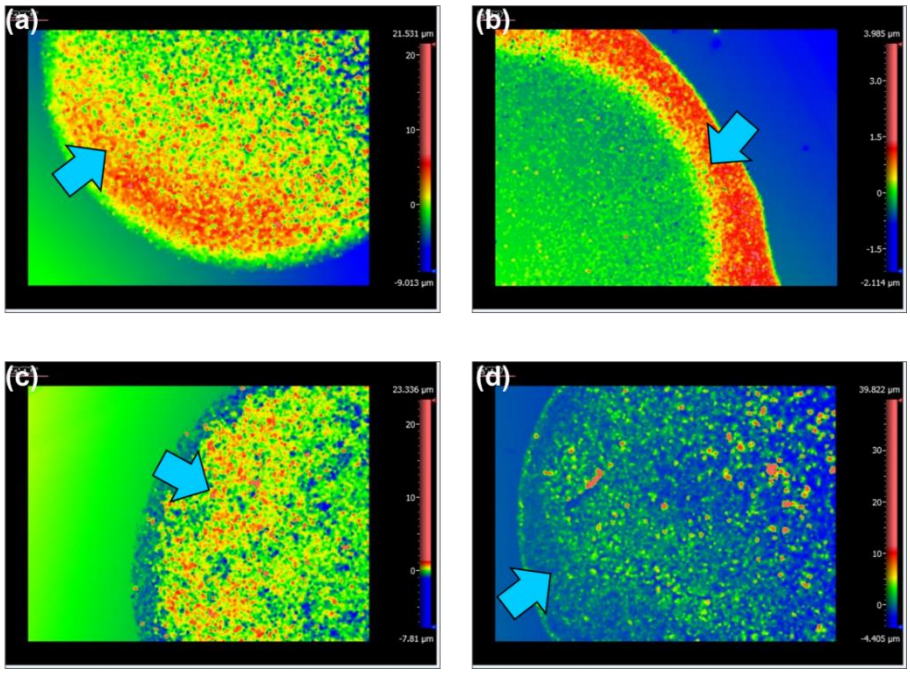

Figure S54. Interferometry profile of the devices made from (a) **NiPc-Ni**, (b) **NiPc-Cu**, (c) **NiNPc-Ni**, and (d) **NiNPc-Cu** as shown in **Figure S53**. Arrows indicates the MOF films.

Table S8. The concentration of the MOF suspension and the resistances and film thickness of the device

Device	Suspension of MOF in H_2O	Film thickness (µm)	Resistance of devices (KΩ)[a]
NiPc-Ni	4 mg in 1mL	2-3	138 ± 15
NiPc-Cu	1 mg in 1 mL	0.7-1	0.73 ± 0.11
NiNPc-Ni	2 mg in 1 mL	0.5-1	7.90 ± 0.74
NiNPc-Cu	2 mg in 1 mL	0.5-1	8.72 ± 0.48

[a] Resistance was measured under ambient conditions under air using a two-point probe.

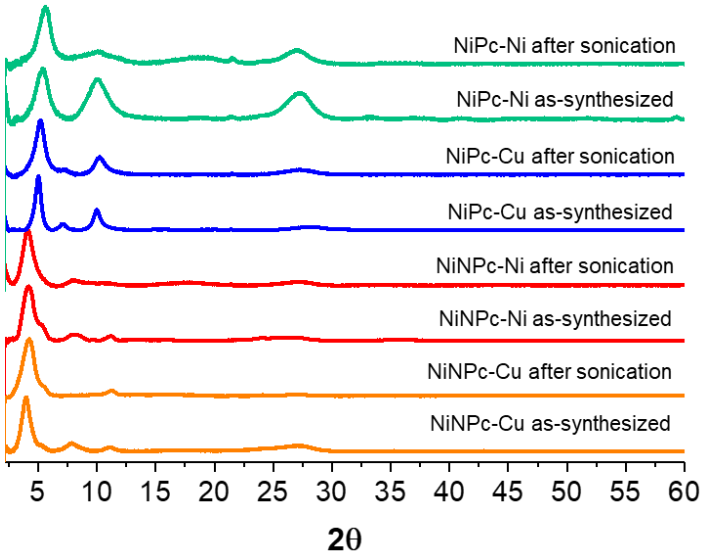

Figure S55. PXRD spectra of the MOFs before and after sonication in H_2O for 2 hours, showing that the MOFs maintained their crystallinities in suspension.

13.2. Sensing Experiments

The sensing performance of the fabricated devices was monitored in a sealed gas-sensing chamber at room temperature. An electrical feed-through and gas inlet and outlet were installed in the chamber. Dry N_2 was used as the balance/purging gas. A Sierra Micro-Trak and a Smart-Trak mass flow controllers were used in combination to deliver controlled concentrations of gases from custom-ordered pre-mixed tanks (10,000 ppm of NH_3 in N_2, and 100 ppm and 10,000 ppm of H_2S or NO in N_2) equipped with two-stage stainless steel regulators. Gas streams from the tanks were diluted with dry N_2 for delivery of controlled concentrations of gases. The concentrations of target gases (NH_3, NO, and H_2S) were adjusted by controlling the flow rates of the target gas and balance gas, which was achieved using two mass-flow controllers. The system was limited to mixing of one gas at a time with a dry N_2 or humidified N_2 stream. The flow of balance/purging gas was controlled at 0.5 or 1 L/min and the flow of the analyte was controlled at 0.3 to 4 mL/min. Before target gas exposure, the gas sensors were stabilized under N_2 exposure for at least 1 h to obtain a flat base line. For the sensing test of NH_3, NO, and H_2S, the exposure of target gas and purging gas was 30 minutes. Unless otherwise specified, all sensing experiments were performed under a constant applied voltage of 0.1 V.

The generation of 5000 ppm humidity stream was followed by the procedure previously reported by our group.[S18] Typically, the gas generator permeation tube was heated to 90 °C using the embedded oven with temperature control, and loaded with a vial of deionized water. Total span

gas flow through the oven was set to 417 mL/min. (During a calibration time of 1169.3 min, 1.9569 g of H_2O in the vial was lost. The concentration of the stream can be calculated as $c = \frac{1.9569\ \text{g}}{18.01\ \text{g mol}^{-1}} \times 22.41\ L\ mol^{-1} \times \frac{1}{0.417\ L/min \times 1169.3\ min}$=5×10^{-3} v/v=5000 ppm.) The resulting vapor stream was mixed with the gas stream delivered by the mass flow system using a Y-connection. The dilution stream of nitrogen usually employed for the dilution of tank gases was not used, with the humid nitrogen from the gas generator serving as the dilution vapor. The dilution vapor (5000 ppm water) was mixed with the controlled stream from the mass flow controllers (1.7 mL/min) to deliver a humidified stream of a single gaseous analyte at 40 ppm.

Raw current data (collected under constant applied voltage) was normalized and converted to normalized conductance according to **Equation S2**, wherein I_o = initial current and I = current at various points during measurement.

$$-\frac{\Delta G}{G_0} = -\frac{I-I_0}{I_0} \times 100\% \qquad \textbf{(S2)}$$

The theoretical limits of detection (LOD) were calculated using reported protocols.[S19-20] First, the root mean squared (rms) value — representing the noise-based deviation in $-\Delta G/G_o$ — was calculated using the baseline trace before exposure to analyte. We took 600-1000 consecutive points (N) and fit the data to a polynomial (5th order). We then calculated sum of squared residuals (SSR) from **Equation S3**, where y_i is measured $-\Delta G/G_o$ and y is the value calculated from the polynomial fit. The root-mean-square deviation (RMS) was then calculated by **Equation S4**. We plotted concentration of analyte versus response ($-\Delta G/G_o$) after a specific exposure time and isolated the range of values wherein this relationship was linear (**Figure S57, S59, S66b, S68b, S74, and S76**). Linear regression provided an equation of best-fit (slope = m). With these values, we extrapolated the theoretical LOD from **Equation (S5)**.

$$SSR = \sum(y_i - y)^2 \qquad \textbf{(S3)}$$

$$RMS = \sqrt{\frac{SSR}{N}} \qquad \textbf{(S4)}$$

$$LOD = 3 \times \frac{RMS}{m} \qquad \textbf{(S5)}$$

Device to device reproducibility is quantified by coefficient of variation (relative standard deviation), and the data is summarized in **Table S18**.

The degree of saturation (DS) of the sensor, which is defined as the ratio of the quantity of the analyte adsorbed after a specific amount of time by the sensor to the quantity of the analyte

absorbed upon the saturation,[S21] was calculated using the **equation S6**. This calculation was based on the assumptions that saturation point achieved after 30 minutes exposure and that the current change (ΔI_t) of the device after *t* min exposure is linear proportional to the quantity of the adsorbed analytes (C_t) by the sensing materials.[S22]

$$DS\% = \frac{C_t}{C_O} = \frac{I_{1.5} - I_0}{I_{30} - I_0} \times 100\% \qquad \textbf{(S6)}$$

In this equation, I_0, $I_{1.5}$, and I_{30} are the current of the devices after analyte dosing for 0, 1.5, and 30 min exposure, respectively, and C_o is the quantity of the adsorbed analytes upon saturation.

13.2.1. NH_3 Sensing

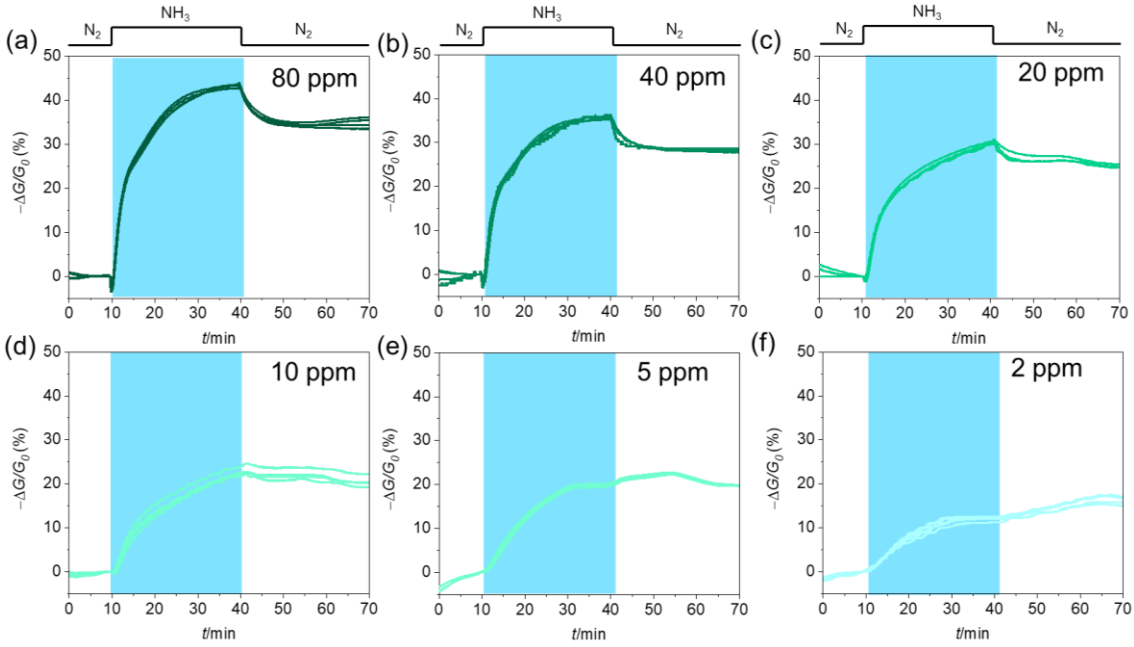

Figure S56. Responses of **NiPc-Ni** devices to (a) 80, (b) 40, (c) 20, (d) 10, (e) 5, and (f) 2 ppm of NH_3. For each concentration, 3–4 freshly prepared devices were used at an applied voltage of 1.0 V.

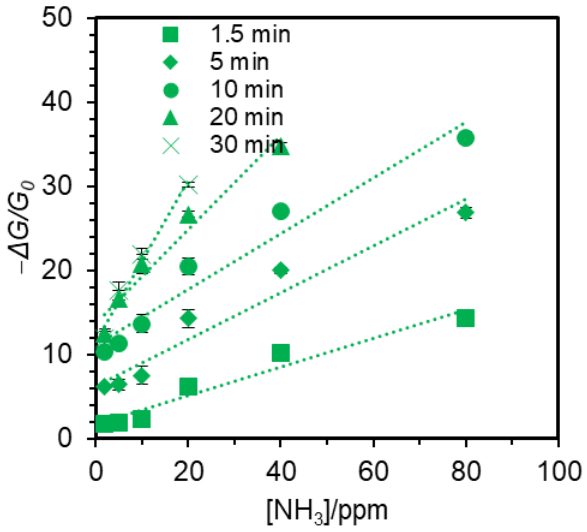

Figure S57. Response of **NiPc-Ni** device as a function of NH_3 concentration. The values of response after the exposure for 1.5, 5, 10, 20 and 30 min were plotted. The slopes of the curves are 0.17, 0.27, 0.33, 0.56, and 0.97. SSR is 0.3061. *N*=1000, RMS is 0.017495.

Table S9. Calculated limits of detection for NH_3 using **NiPc-Ni** under different exposure time.

Exposure time/min	1.5	5	10	20	30
LOD/ppm	0.31	0.19	0.16	0.09	0.05

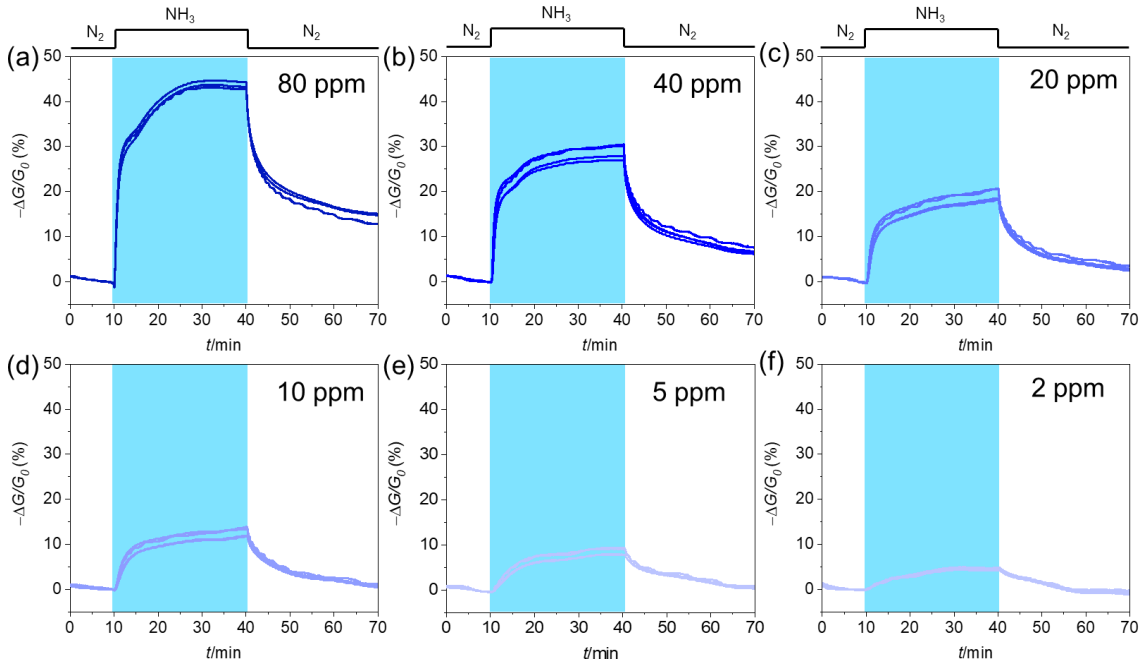

Figure S58. Responses of **NiPc-Cu** devices to (a) 80, (b) 40, (c) 20, (d) 10, (e) 5, and (f) 2 ppm of NH_3. For each concentration, 3-4 freshly prepared devices were used.

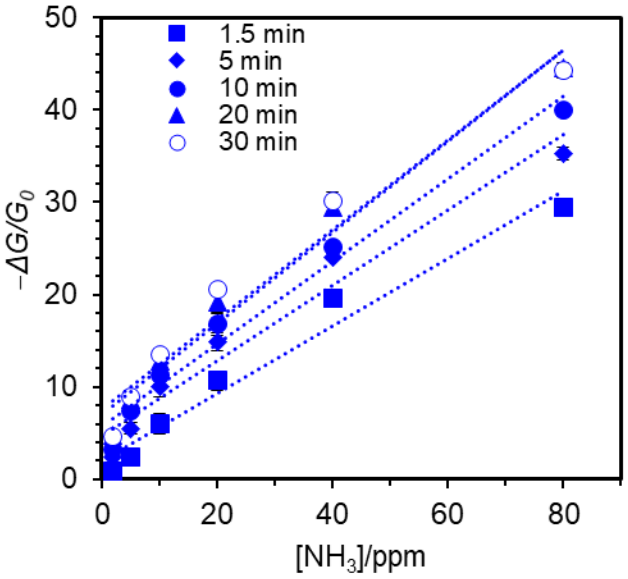

Figure S59. Response of **NiPc-Cu** device as a function of NH_3 concentration. The response values after the exposure for 1.5, 5, 10, 20 and 30 min were plotted. The slopes of the curves are 0.37, 0.38, 0.42, 0.63, and 0.64. SSR is 1.2975. *N*=1000, RMS is 0.0360.

Table S10. Calculated limits of detection for NH_3 using **NiPc-Cu** as a function of exposure times.

Exposure time/min	1.5	5	10	20	30
LOD/ppm	0.33	0.28	0.26	0.17	0.16

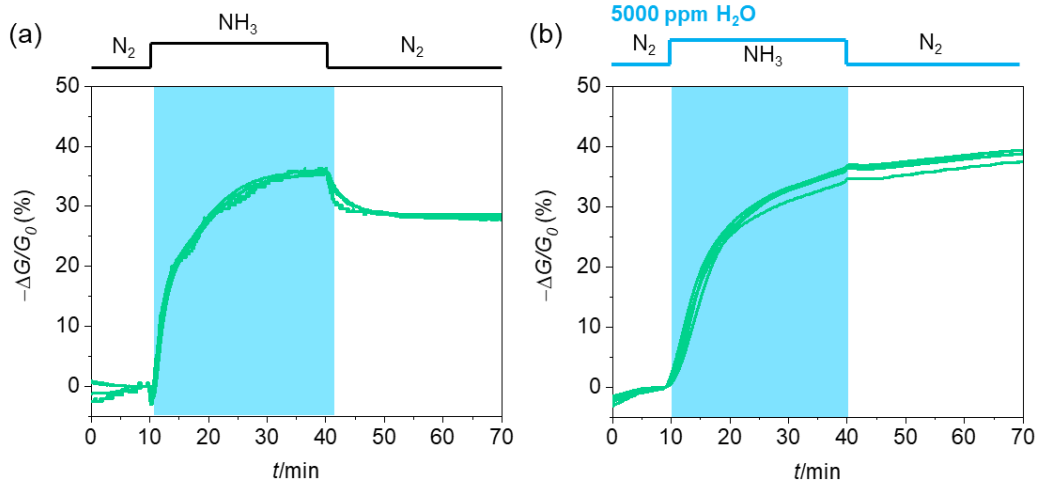

Figure S60. Comparison of response of **NiPc-Ni** devices to (a) 40 ppm of NH_3 without presence of H_2O and (b) 40 ppm of NH_3 in the presence of 5000 ppm of H_2O. Devices were used at an applied voltage of 1.0 V.

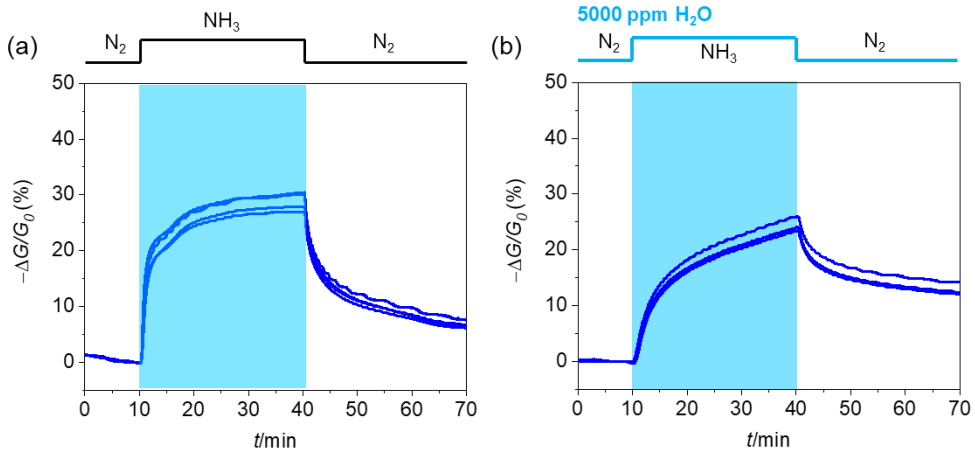

Figure S61. Comparison of response of **NiPc-Cu** devices to (a) 40 ppm of NH_3 without presence of H_2O and (b) 40 ppm of NH_3 in the presence of 5000 ppm of H_2O.

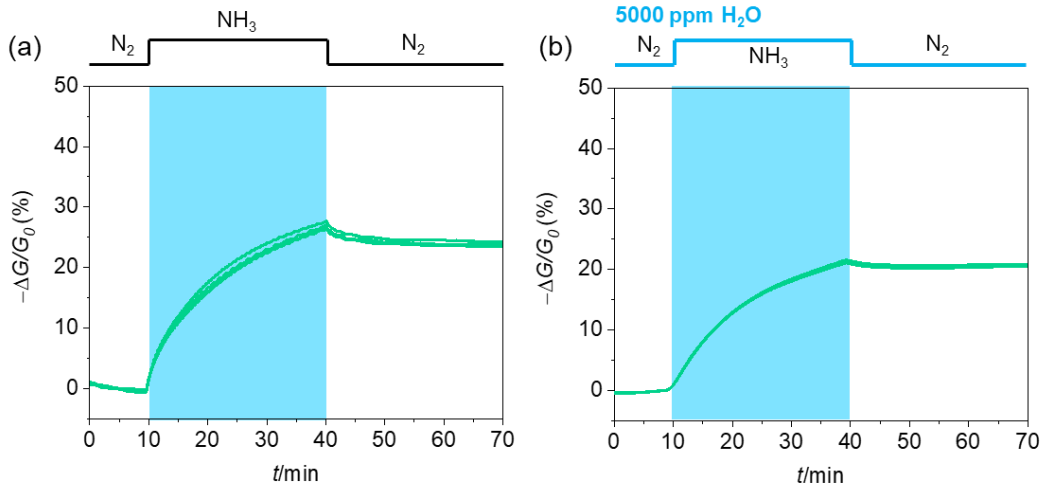

Figure S62. Comparison of response of **NiNPc-Ni** devices to (a) 40 ppm of NH_3 without presence of H_2O and (b) 40 ppm of NH_3 in the presence of 5000 ppm of H_2O.

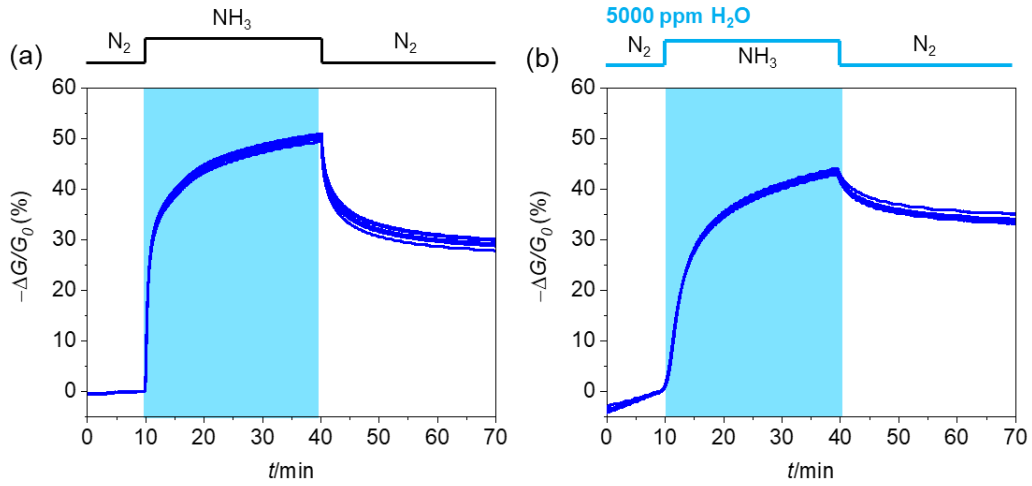

Figure S63. Comparison of response of **NiNPc-Cu** devices to (a) 40 ppm of NH_3 without presence of H_2O and (b) 40 ppm of NH_3 in the presence of 5000 ppm of H_2O.

Table S11. Degree of saturation (DS%) after 1.5 min exposure at different concentrations of NH_3.

	80 ppm	40 ppm	20 ppm	10 ppm	5 ppm	2 ppm
NiPc-Ni	33.8	28.6	20.4	10.8	10.9	14.8
NiPc-Cu	66.6	65.2	52.0	44.5	26.6	19.9

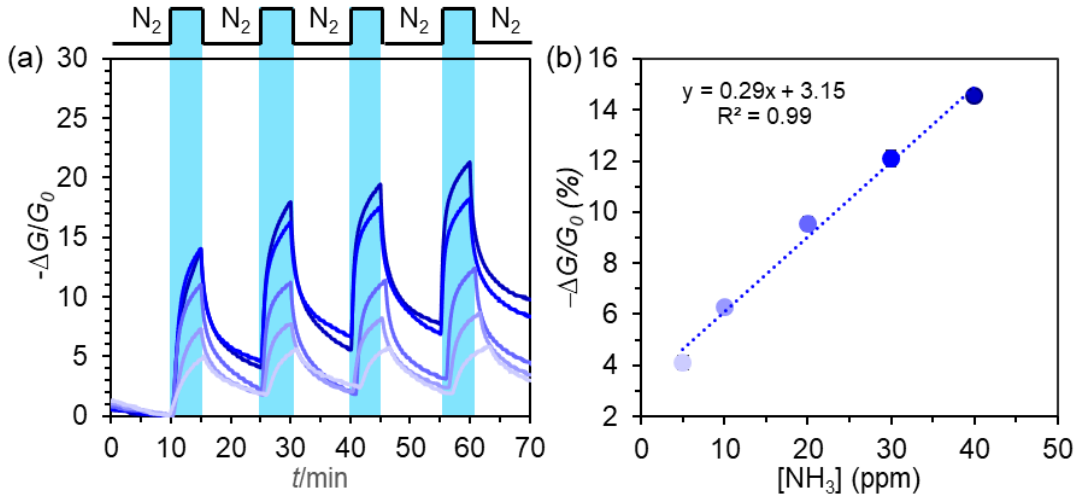

Figure S64. (a) Responses of **NiPc-Cu** devices to 4 sequential exposures of 40, 30, 20, 10, and 5 ppm (dark blue to light blue curve) of NH_3 at the applied voltage of 0.01 V. (b) Response of **NiPc-Cu** device as a function of NH_3 concentration. The LOD determined from this sequential exposure method is 0.34 ppm.

13.2.2. H_2S Sensing

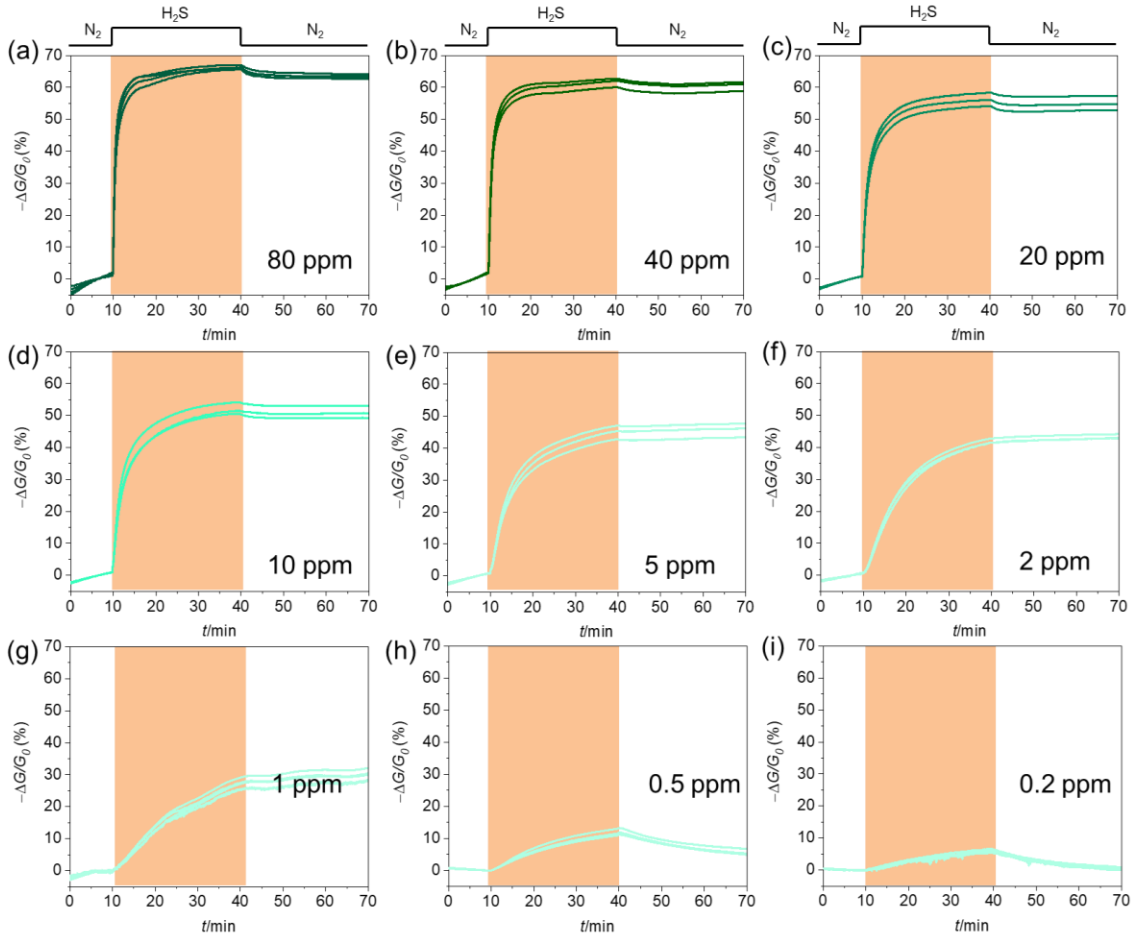

Figure S65. Responses of **NiPc-Ni** devices to (a) 80, (b) 40, (c) 20, (d) 10, (e) 5, (f) 2, (g) 1, (h) 0.5, and (i) 0.2 ppm of H_2S. For each concentration, 3 to 4 fresh devices were used with an applied voltage of 1.0 V.

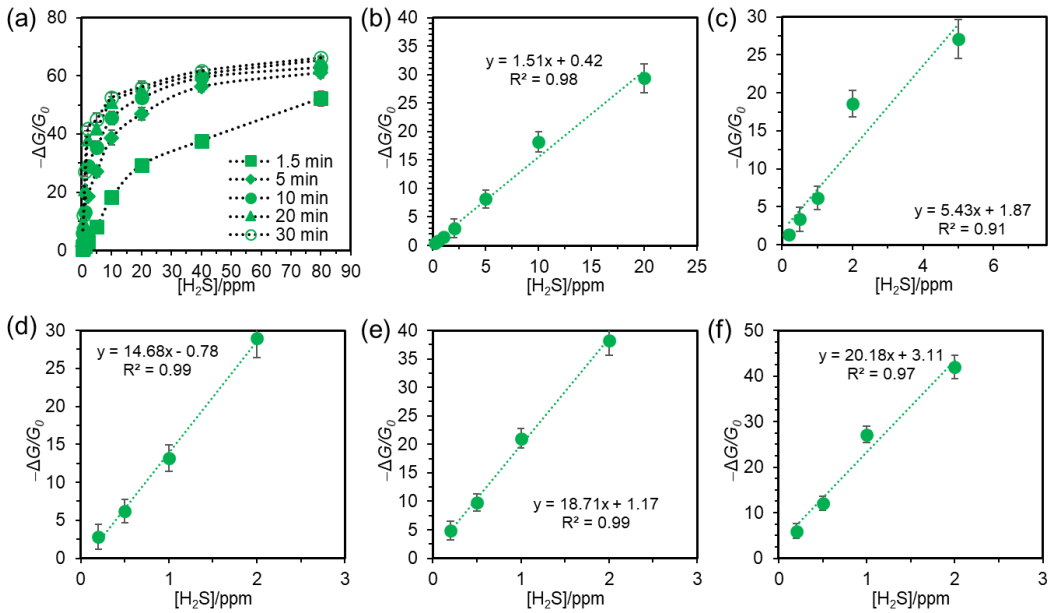

Figure S66. (a) Response of **NiPc-Ni** devices upon different exposure time as a function of H_2S concentration at 0.2-80 ppm. The observed linear relationship between the response and concentration upon (b) 1.5, (c) 5, (d) 10, (e) 20 and (f) 30 min exposure. SSR is 0.26389. *N*=1000, RMS is 0.016244.

Table S12. Calculated limits of detection for H_2S using **NiPc-Ni** under different exposure times.

Exposure time/min	1.5	5	10	20	30
LOD/ppb	32.27	8.97	3.31	2.60	2.41

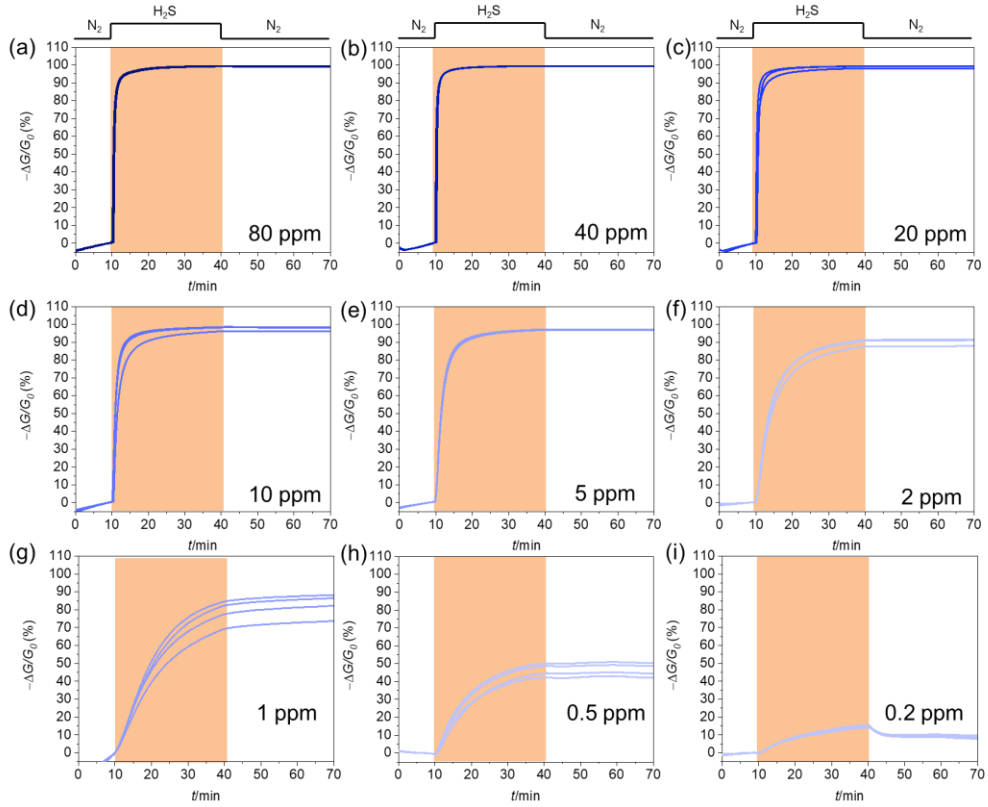

Figure S67. Responses of **NiPc-Cu** devices to (a) 80, (b) 40, (c) 20, (d) 10, (e) 5, (f) 2, (g) 1, (h) 0.5, and (i) 0.2 ppm of H_2S. For each concentration, 3 to 4 fresh devices were used.

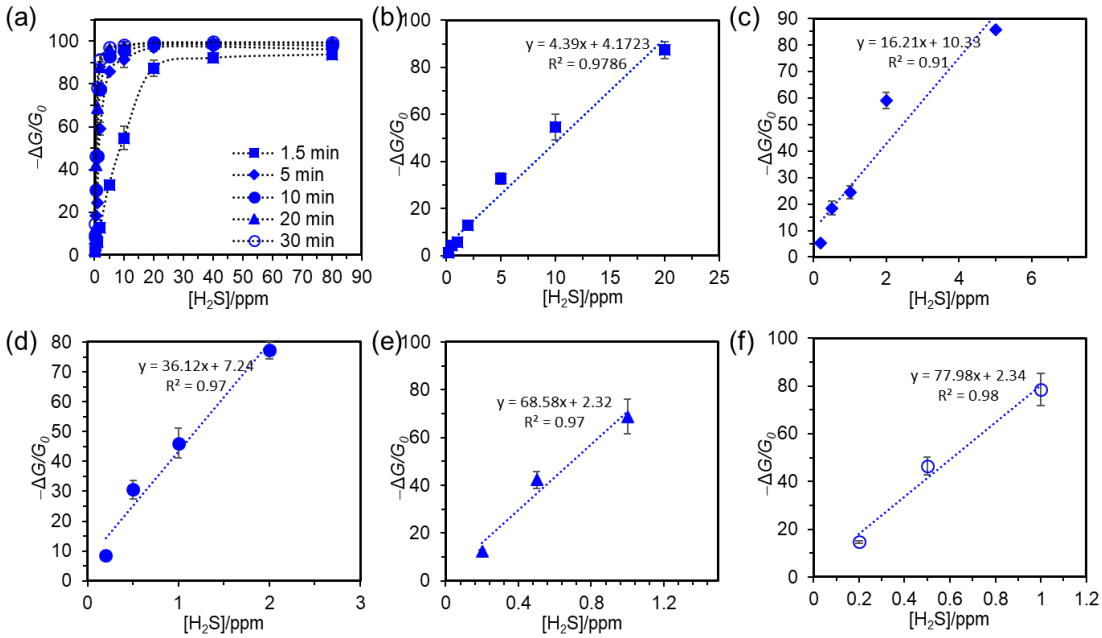

Figure S68. (a) Response of **NiPc-Cu** devices upon different exposure time as a function of H_2S concentration at 0.2-80 ppm. The observed linear relationship between the response and concentration upon (b) 1.5, (c) 5, (d) 10, (e) 20 and (f) 30 min exposure. SSR is 0.73441. *N*=1000, RMS is 0.0271.

Table S13. Calculated limits of detection for H_2S using **NiPc-Cu** as a function of exposure times.

Exposure time/min	1.5	5	10	20	30
LOD/ppb	18.52	5.01	2.25	1.19	1.04

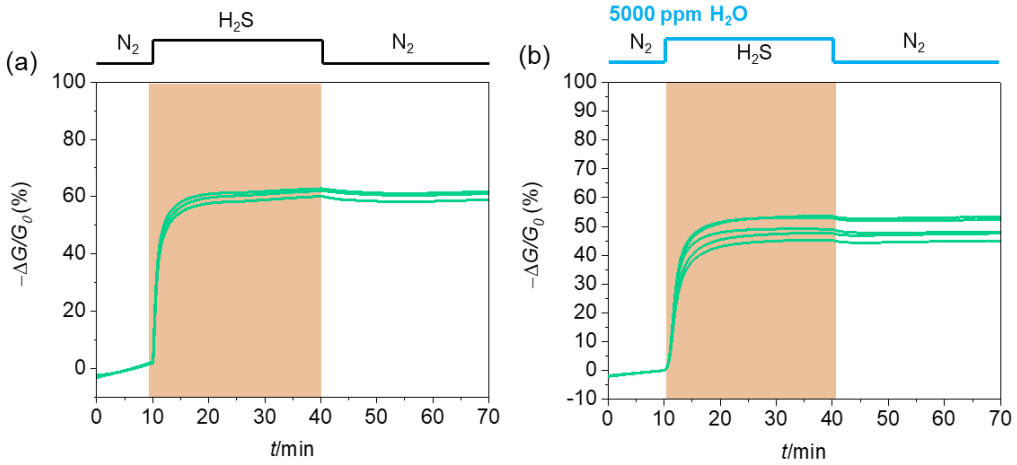

Figure S69. Comparison of response of **NiPc-Ni** devices to (a) 40 ppm of H_2S without presence of H_2O and (b) 40 ppm of H_2S in the presence of 5000 ppm of H_2O (voltage 1.0 V).

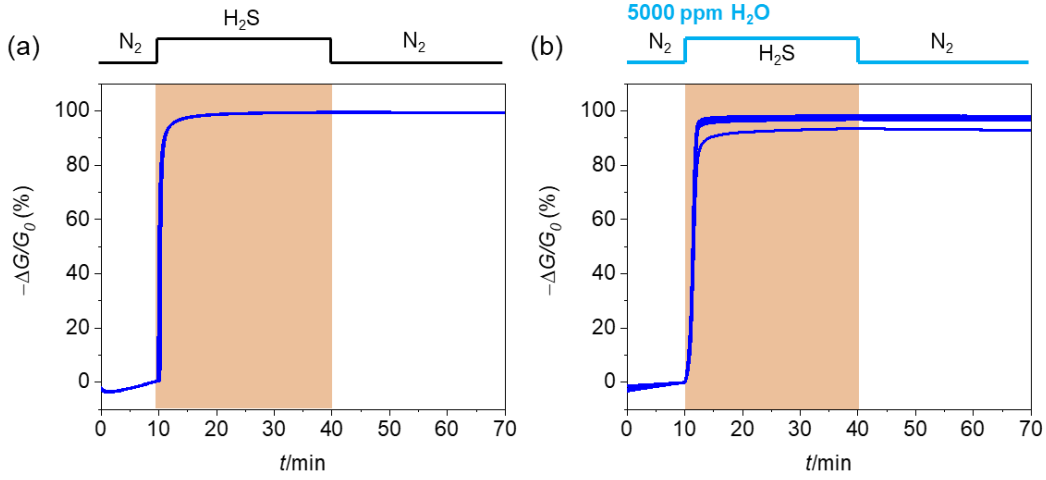

Figure S70. Comparison of response of **NiPc-Cu** devices to (a) 40 ppm of H_2S without presence of H_2O and (b) 40 ppm of H_2S in the presence of 5000 ppm of H_2O.

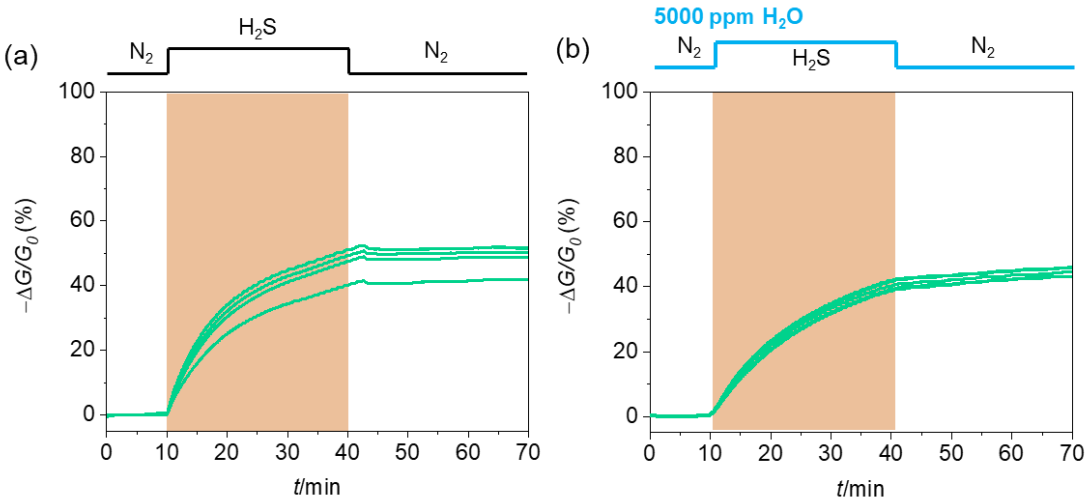

Figure S71. Comparison of response of **NiNPc-Ni** devices to (a) 40 ppm of H_2S without presence of H_2O and (b) 40 ppm of H_2S in the presence of 5000 ppm of H_2O.

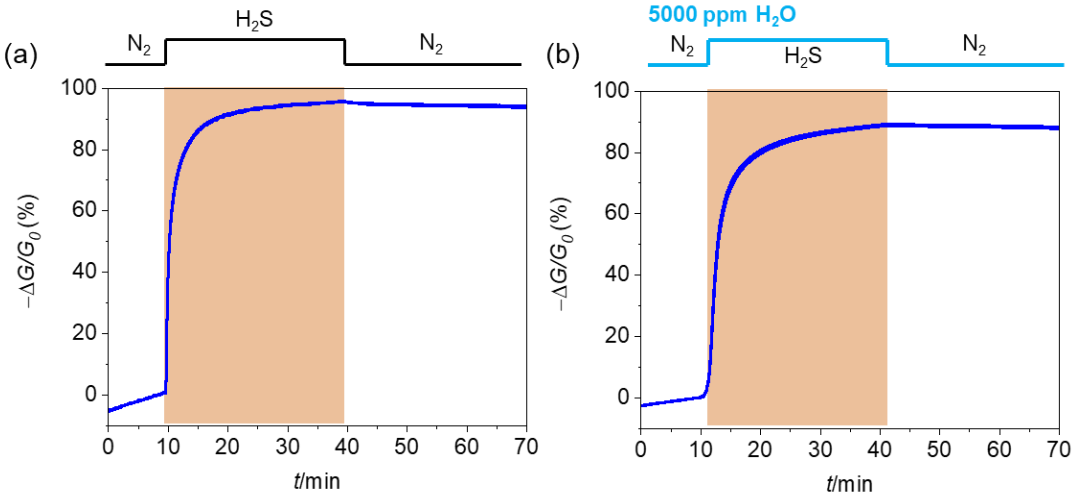

Figure S72. Comparison of response of **NiNPc-Cu** devices to (a) 40 ppm of H_2S without presence of H_2O and (b) 40 ppm of H_2S in the presence of 5000 ppm of H_2O.

Table S14. Degree of saturation (DS%) after 1.5 min exposure at different concentrations of H_2S.

	80 ppm	40 ppm	20 ppm	10 ppm	5 ppm	2 ppm	1 ppm	0.5 ppm	0.2 ppm
NiPc-Ni	78.9	61.2	52.3	34.7	18.1	7.10	5.5	7.4	6.4
NiPc-Cu	94.2	92.5	91.6	72.4	52.8	25.0	7.5	9.5	9.5

13.2.3. NO Sensing

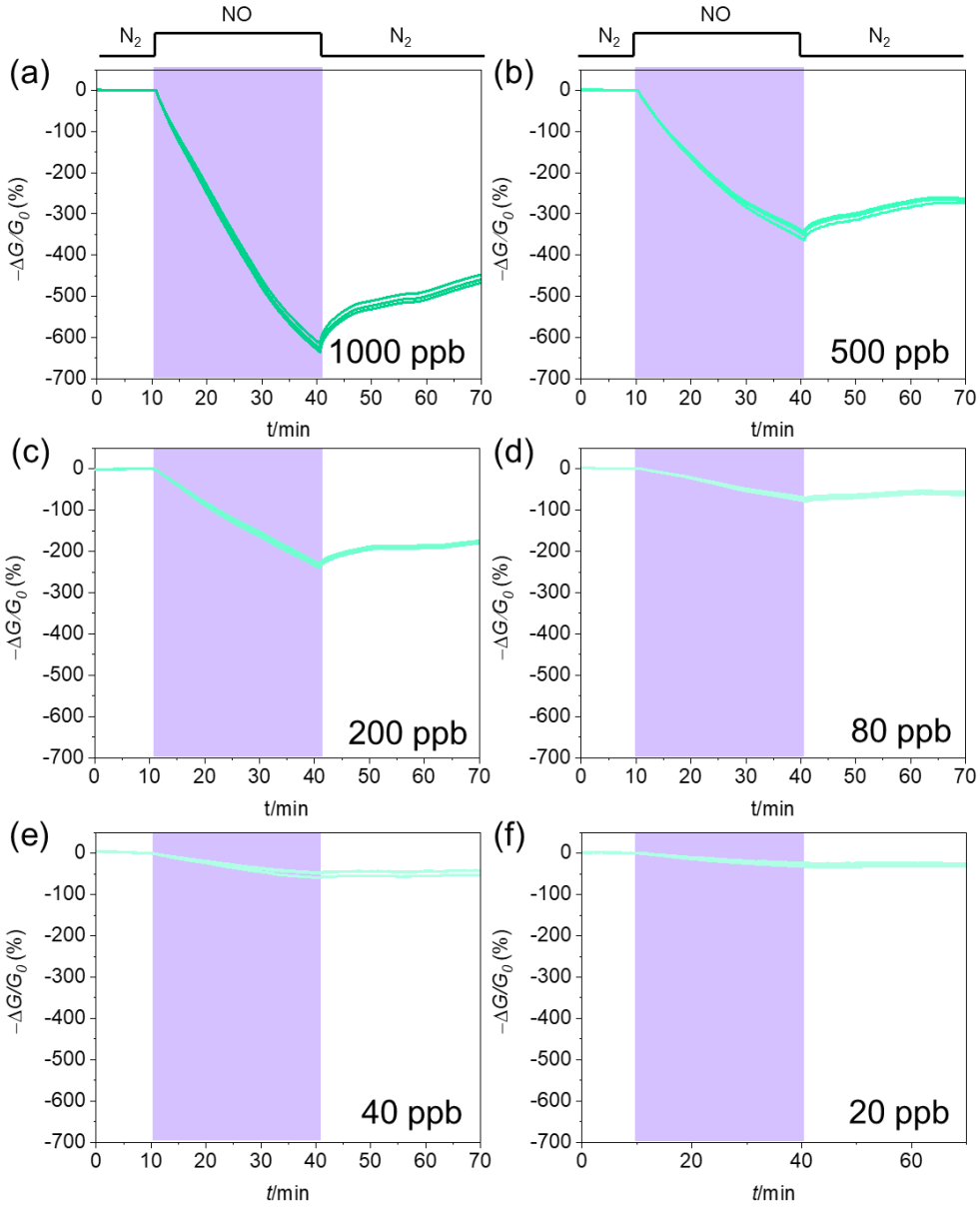

Figure S73. Responses of **NiPc-Ni** devices to (a) 1000, (b) 500, (c) 200, (d) 80, (e) 40, and (f) 20 ppb of NO. For each concentration, 3 to 4 fresh devices were used with an applied voltage of 1.0 V.

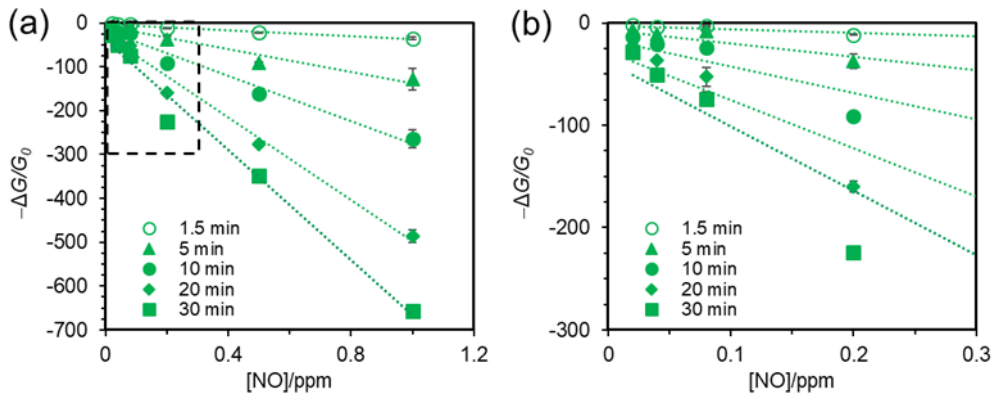

Figure S74. (a) Linear relationship between the response of **NiPc-Ni** device as a function of NO concentration at 0.02 to 1.0 ppm. (b) An expanded view of the chart in (a) marked with rectangle. The response values after the exposure for 1.5, 5, 10, 20 and 30 min were plotted. The slopes of the curves from bottom to up are -33.0, -130.8, -258.4, -470.4, and -627.8, respectively. RSS is 0.08223, *N*=600, RMS is 0.01170.

Table S15. Calculated limits of detection for NO using **NiPc-Ni** as a function of exposure time.

Exposure time/min	1.5	5	10	20	30
LOD/ppb	1.06	0.27	0.14	0.07	0.06

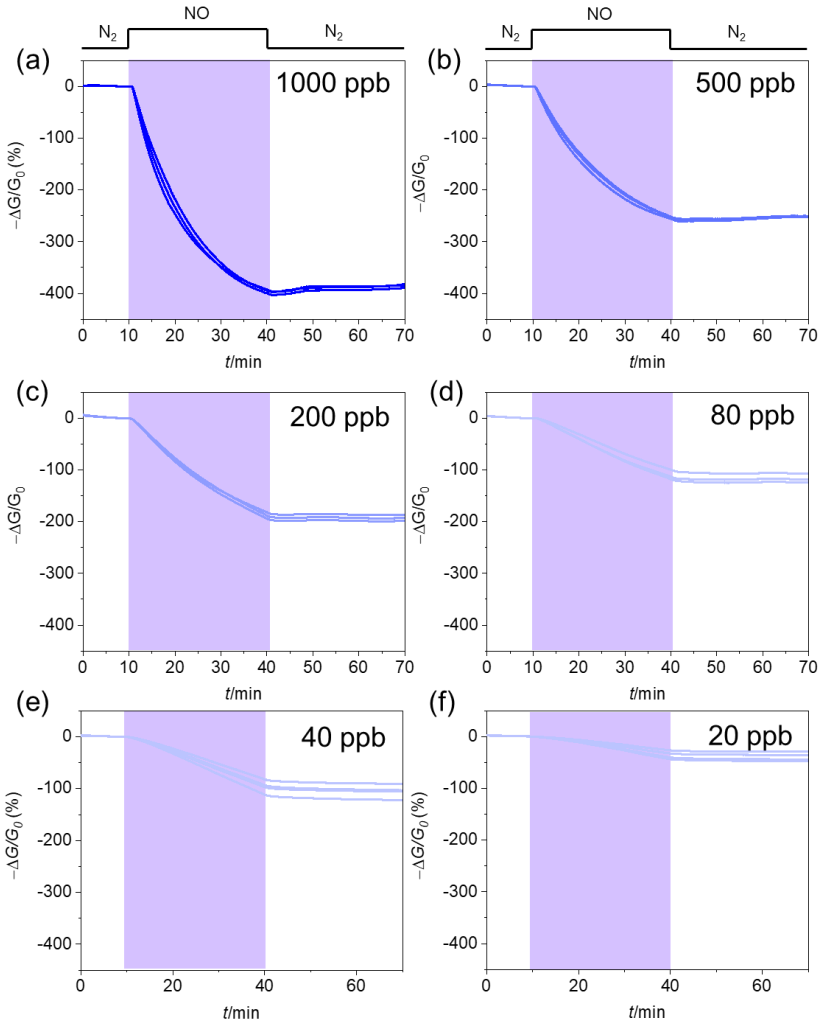

Figure S75. Responses of **NiPc-Cu** device to (a) 1000, (b) 500, (c) 200, (d) 80, (e) 40, and (f) 20 ppb of NO. For each concentration, 3 to 4 fresh devices were used.

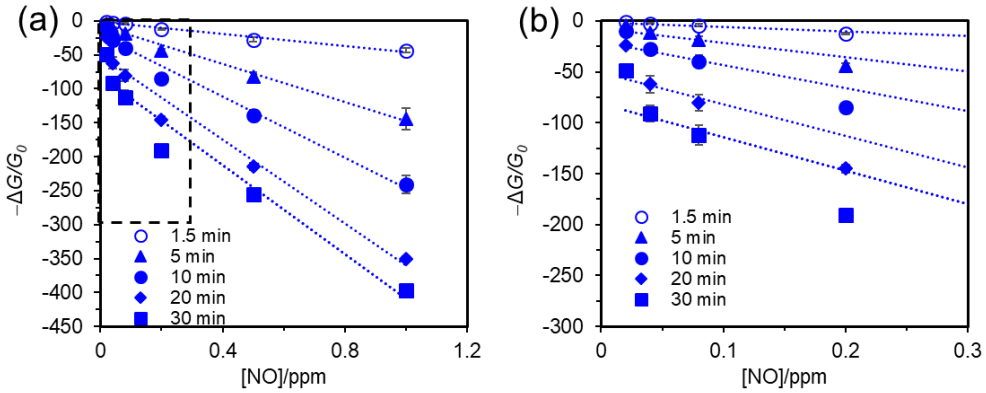

Figure S76. (a) Linear relationship between the response of **NiPc-Ni** device as a function of NO concentration at 0.02 to 1.0 ppm. (b) An expanded view of the chart in (a) marked with rectangle. The response values after the exposure for 1.5, 5, 10, 20 and 30 min were plotted. The slopes of the curves are -42.5, -139.8, -225.7, -309.4, and -332.0. SSR is 0.20441, *N*=1030, RMS is 0.01408.

Table S16. Calculated limits of detection for NO using **NiPc-Cu** as a function of exposure times.

Exposure time/min	1.5	5	10	20	30
LOD/ppb	1.00	0.30	0.19	0.14	0.13

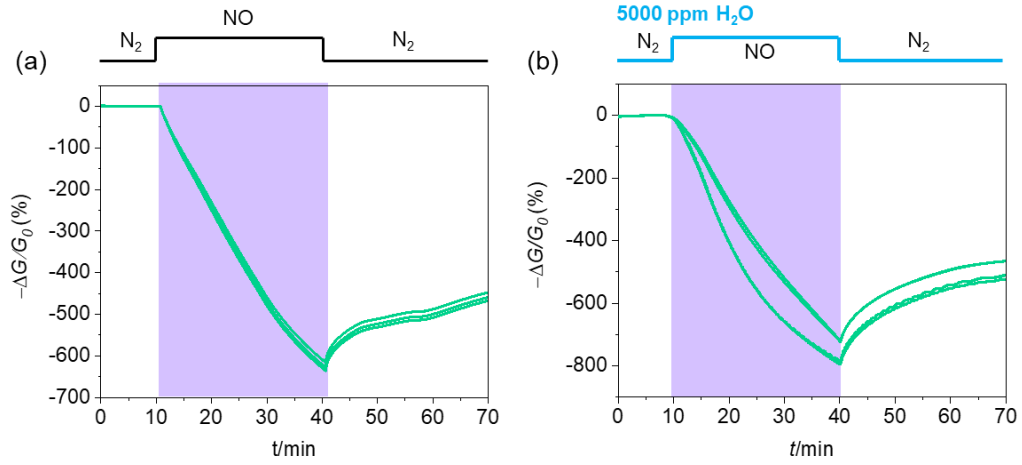

Figure S77. Comparison of response of **NiPc-Ni** devices to (a) 1 ppm of NO without presence of H_2O and (b) 1.0 ppm of NO in the presence of 5000 ppm of H_2O.

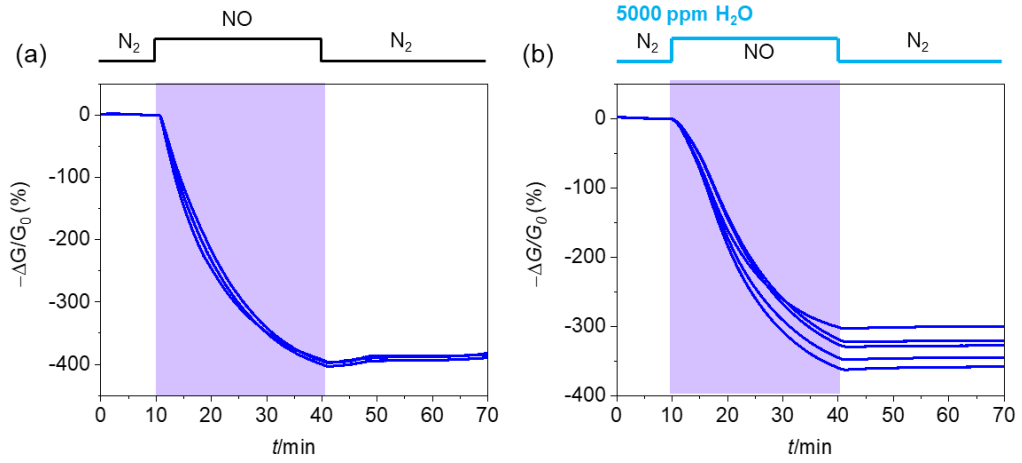

Figure S78. Comparison of response of **NiPc-Cu** devices to (a) 1.0 ppm of NO without presence of H_2O and (b) 1.0 ppm of NO in the presence of 5000 ppm of H_2O.

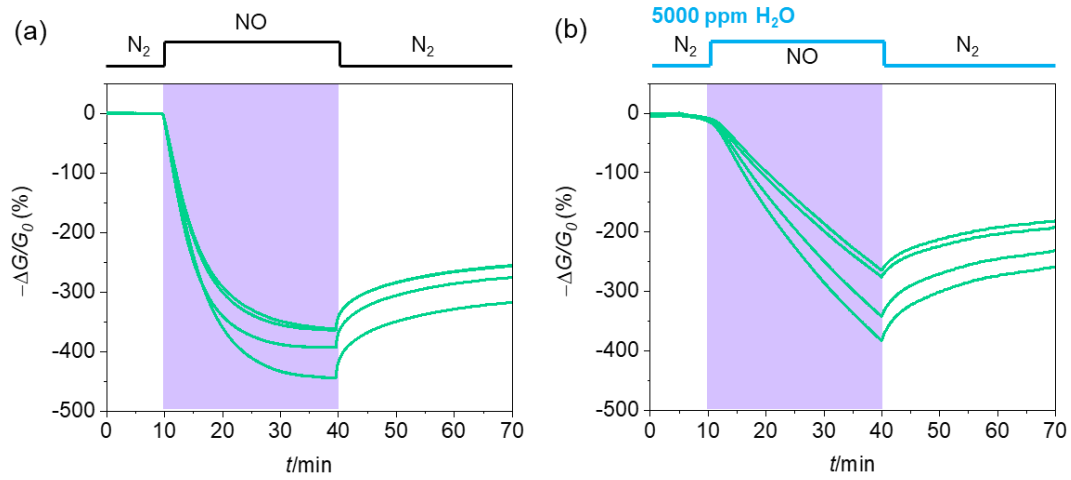

Figure S79. Comparison of response of **NiNPc-Ni** devices to (a) 1.0 ppm of NO without presence of H_2O and (b) 1.0 ppm of NO in the presence of 5000 ppm of H_2O.

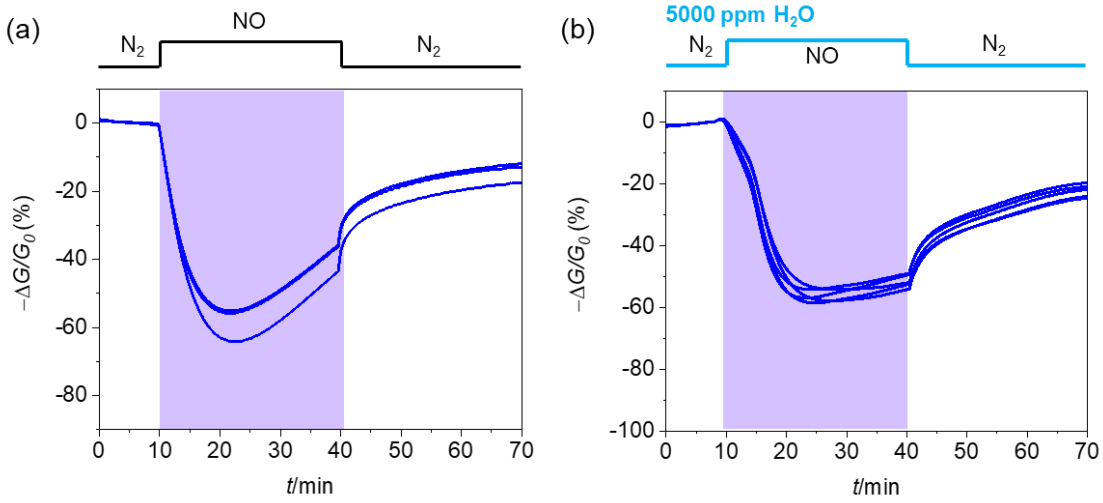

Figure S80. Comparison of response of **NiNPc-Cu** devices to (a) 1.0 ppm of NO without presence of H_2O and (b) 1.0 ppm of NO in the presence of 5000 ppm of H_2O.

Table S17. Degree of saturation (DS%) after 1.5 min exposure at different concentrations of NO.

	1 ppm	0.5 ppm	0.2 ppm	0.08 ppm	0.04 ppm	0.02 ppm
NiPc-Ni	5.3	6.3	5.1	4.4	7.4	6.4
NiPc-Cu	10.9	10.9	6.4	3.7	3.0	2.7

Table S18. Summary of coefficient of variation (%) for the four MOFs for 40 ppm NH_3, 40 ppm of H_2S, and 1.0 ppm of NO with and without the interference of H_2O. The averaged coefficient of variation is 3.98%.

	40 ppm NH_3	40 ppm NH_3 + 5000 ppm H_2O	40 ppm H_2S	40 ppm H_2S + 5000 ppm H_2O	1 ppm NO	1 ppm NO+ 5000 ppm H_2O
NiPc-Ni	1.81	2.57	2.26	4.99	1.85	5.32
NiPc-Cu	3.45	4.49	0.41	2.19	0.95	6.92
NiNPc-Ni	2.62	0.96	10.03	3.57	9.85	14.51
NiNPc-Cu	1.28	1.27	0.12	0.25	9.79	4.14

13.2.4. Analysis for Initial Rates of Response

Analyzing the initial rate of response of the sensor is a convenient technique that can enable concentration-dependent measurement on a short timescale (less than a minute). The application of initial rate analysis is well-established in biochemical sensors.[S23-24] The initial rate analysis usually takes a significantly shorter time to complete a measurement compared with the steady-state analysis.[S23] At the initial stage of the analyte exposure, only a very small portion of the activate sites on the surface of the materials is occupied. Considering that the sensor usually works in an environment it is exposed to low concentrations of analytes, it is rational to assume that, at the initial stage of the analyte exposure, the concentration of the analytes will be much smaller than the density of unoccupied active sites on the sensing material. Consequently, the reaction/interaction/binding event between the analyte and active sites on the surface of the sensing material can be treated as a pseudo-first-order reaction.[S25] In this case, the initial rate of the analyte binding will be proportional to the concentration of the analyte. Since the response of the sensor can be proportional to the quantity of analytes bound to the surface of the sensing material based on the site-binding mechanism for chemiresistive sensing,[S26] The initial rate of response can thus be expected to be proportional to the concentration of the analyte.

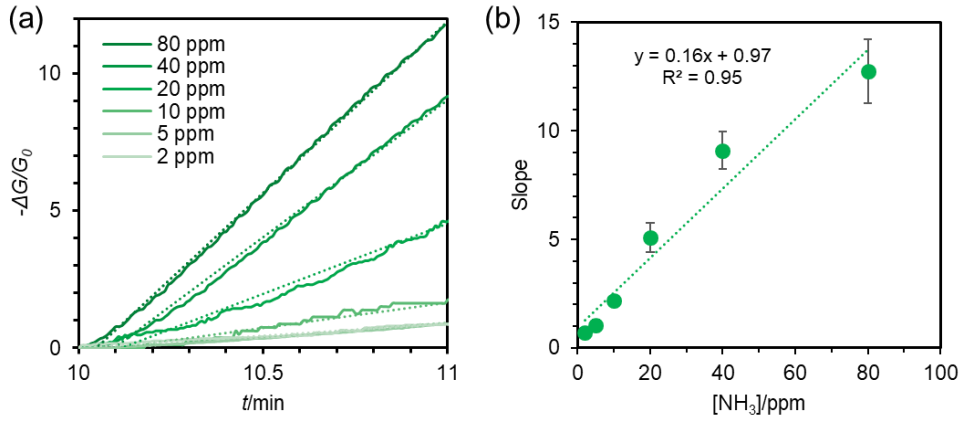

Figure S81. (a) Responses of **NiPc-Ni** devices to 80, 40, 20, 10, 5, and 2 ppm of NH_3 after 1 min's exposure and the linear fitting of the response. (b) The slope of the fitting as a function of concentration.

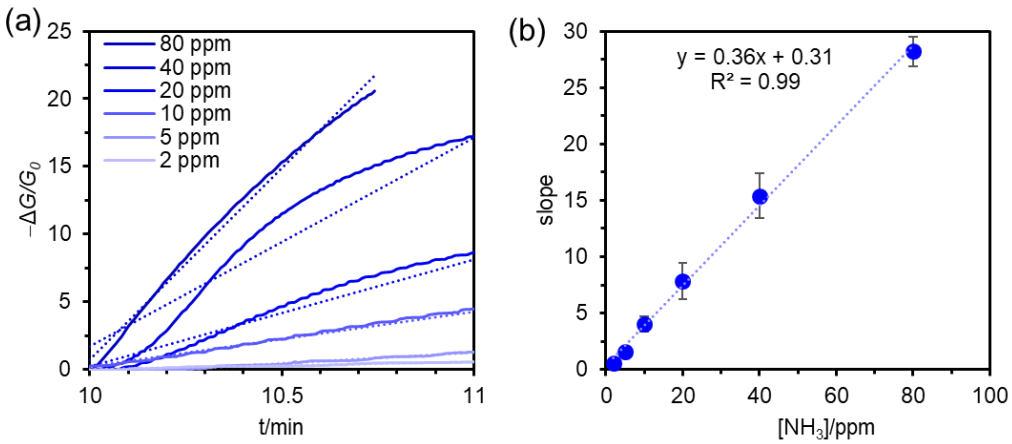

Figure S82. (a) Responses of **NiPc-Cu** devices to 80, 40, 20, 10, 5, and 2 ppm of NH_3 after 1 min's exposure and the linear fitting of the response. (b) The slope of the fitting as a function of concentration.

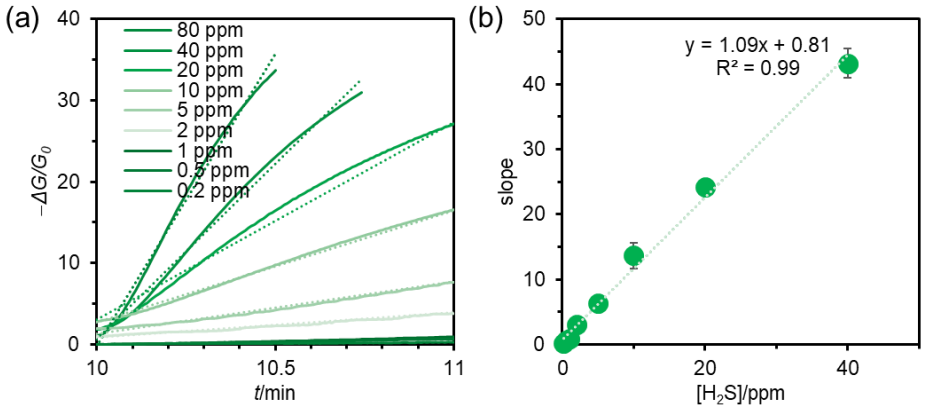

Figure S83. (a) Responses of **NiPc-Ni** devices to 80, 40, 20, 10, 5, 2, 1, 0.5, and 0.2 ppm of H_2S after 1 min exposure and the linear fitting of the response. (b) The slope of the fitting as a function of concentration.

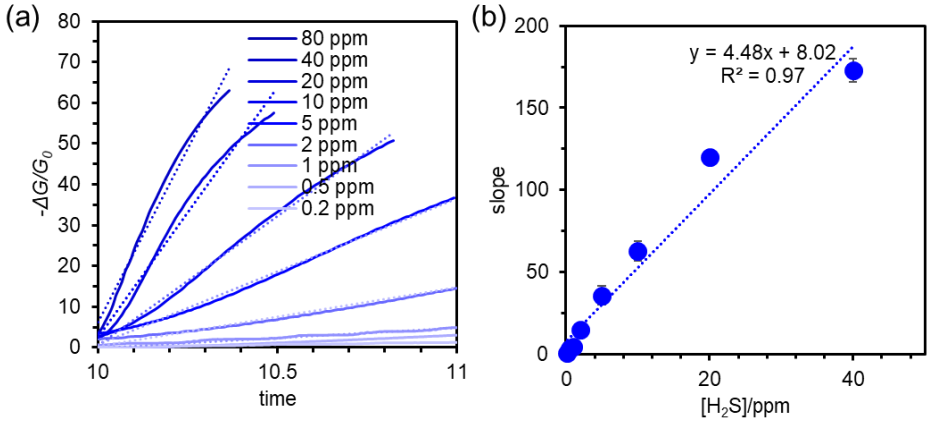

Figure S84. (a) Responses of **NiPc-Cu** devices to 80, 40, 20, 10, 5, 2, 1, 0.5, and 0.2 ppm of H_2S after 1 min exposure and the linear fitting of the response. (b) The slope of the fitting as a function of concentration.

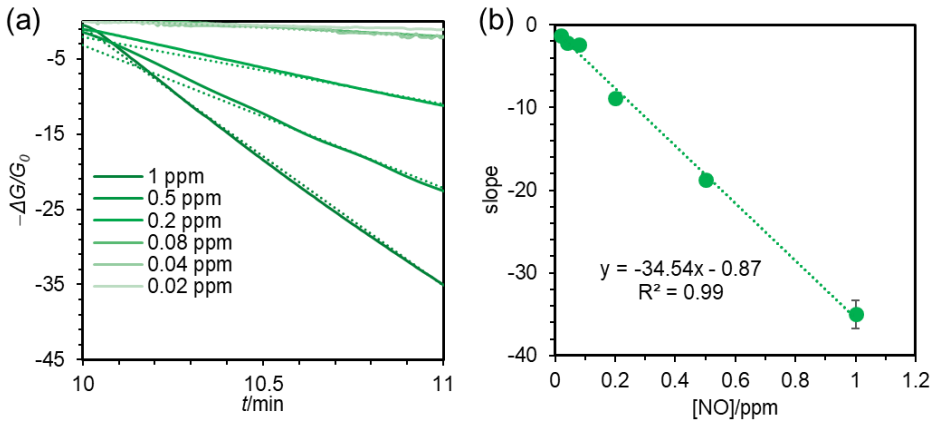

Figure S85. (a) Responses of **NiPc-Ni** devices to 1, 0.5, 0.2, 0.08, 0.04, and 0.02 ppm of NO after 1 min exposure and the linear fitting of the response. (b) The slope of the fitting as a function of concentration.

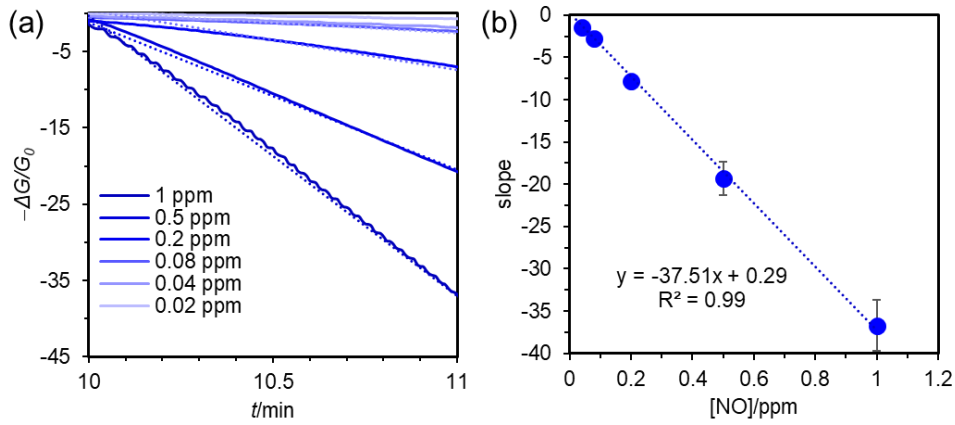

Figure S86. (a) Responses of **NiPc-Cu** devices to 1, 0.5, 0.2, 0.08, 0.04, and 0.02 ppm of NO after 1 min's exposure and the linear fitting of the response. (b) The slope of the fitting as a function of concentration.

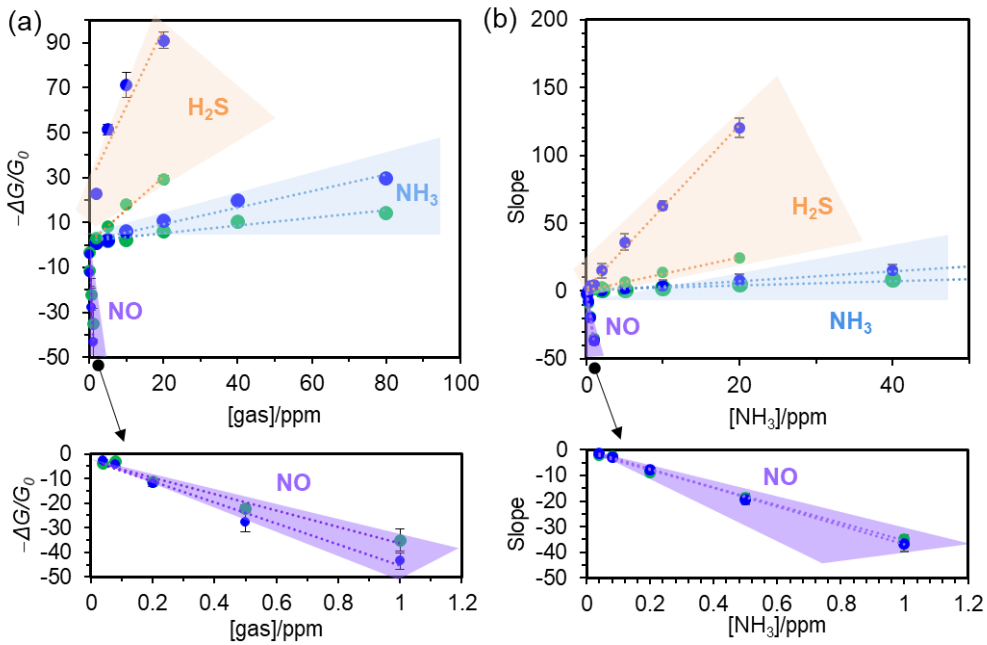

Figure S87. (a) Relationship between the response ($-\Delta G/G_0$) after 1.5 min exposure of gases and gas concentrations. (b) Relationship between the slope of the response ($(-\Delta G/G_0)/\Delta t$) during the first 1 min exposure to gases and gas concentrations. Both the response ($-\Delta G/G_0$) and slope of the response ($(-\Delta G/G_0)/\Delta t$) analysis allows the quick discrimination of the three gaseous analytes and their concentrations within a short time of 1.5 min and 1.0 min, respectively. The insets show the fitting range for NO.

Table S19. Parameters for principal component analysis for 40 ppm NH_3, 40 ppm H_2S, and 1.0 ppm NO.

MOFs	Gas	X1 (response at 30 min)	X2 (slope of response at 1 minutes)	X3 ($I_0/I_{30\ min}$)	X4 (response at 20 min)	X5 (response time)	X6 (recovery ratio)	X7 (response value after recovery)
NiPc-Ni	NH_3	35.71	9.47	1.56	34.3	15.4	20.18	28.5
	H_2S	61.62	43.17	2.61	61.1	4.1	2.62	60
	NO	-657.54	-34.37	0.13	-470	27	31.56	-450
NiPc-Cu	NH_3	30.08	15.42	1.43	28.7	9.3	80.05	6
	H_2S	99.56	170.01	227.27	99.2	1.07	0.56	99
	NO	-397.28	-36.69	0.20	-345	21.8	1.83	-390
NiNPc-Ni	NH_3	26.80	7.28	1.37	23.3	21	10.45	24
	H_2S	48.12	5.43	1.93	43	20.2	0.25	48
	NO	-389.75	-45.40	0.20	-360	10	25.59	-290
NiNPc-Cu	NH_3	50.23	48.00	2.01	48.2	11.6	42.27	29
	H_2S	95.20	103.00	20.82	94.6	4.7	1.26	94
	NO	-41.67	-10.70	0.71	-45	5	56.80	-18

Response time is the amount of time it takes to get to 90% of response values at 30 min exposure.

Recovery ratio is defined as $\frac{I_{30\ min}-I_{after\ recovery}}{I_{30\ min}-I_0} \times 100\%$.

The PCA was performed by using Statistics selection of OriginLab.

Table S20. Representative examples of NH_3, H_2S, and NO detection by NiPc-M MOFs and other nanomaterials/methods.

material	analyte	Sensing devices or method	LOD	Detection range	reference
NiPc-Ni	NH_3	chemiresistor	0.05-0.31 ppm	2-80 ppm	This work
NiPc-Cu	NH_3	chemiresistor	0.16-0.33 ppm	2-80 ppm	This work
$Cu_3(HHTP)_2$	NH_3	chemiresistor	0.500 ppm	1-100 ppm	S27
Cu_3HITP_2	NH_3	chemiresistor	0.5 ppm	0.5-10 ppm	S28
M_3HHTP_2−Graphene (M = Fe, Co, Ni, or Cu)	NH_3	chemiresistor	10 ppm	5-1200 ppm	S29
graphene	NH_3	chemiresistor	1 ppm	N/A	S30
graphene	NH_3	FET	0.16 ppm	5-100 ppm	S31
black phosphorus	NH_3	chemiresistor	10 ppm	10-300 ppm	S32
MoS_2	NH_3	FET	0.3 ppm	0.3-30 ppm	S33
reduced graphene oxide	NH_3	chemiresistor	1 ppb	1 ppb-50 ppm	S34
$Ti_3C_2T_x$	NH_3	chemiresistor	0.13 ppb	100-1000 ppb	S35
single-walled carbon nanotubes	NH_3	chemiresistor	0.1%	N/A	S36
Modified single-walled carbon nanotubes	NH_3	chemiresistor	0.1 ppm	1.5-20 ppm	S37
Polyaniline	NH_3	chemiresistor	1 ppm	1-600 ppm	S38

Palladium	NH_3	chemiresistor	1 ppm	0.2×10^{-6}–5×10^{-5} M	S39
N/A	NH_3	absorption spectroscopy	1 ppb	N/A	S40
N/A	NH_3	ion chromatography	2.8 ± 1.9 ppb	0-1000 ppb	S41
N/A	NH_3	gas chromatography with flame photometric detector (GC-FPD)	~1.5 pmol/mL	2-40 nmol/mL	S42
N/A	NH_3	cavity ring-down spectroscopy (CRDS)	50 ppb	0.1-2 ppm	S43
NiPc-Ni	H_2S	chemiresistor	2.4-32.3 ppb	0.2 -80 ppm	This work
NiPc-Cu	H_2S	chemiresistor	1.0-18.5 ppb	0.2 -80 ppm	This work
Ni_3HHTP_2	H_2S	chemiresistor	0.23 ppm	*5−80 ppm*	S18
M_3HHTP_2−Graphene (M = Fe, Co, Ni, or Cu)	H_2S	chemiresistor	35 ppm	5−80 ppm	S29
CuO	H_2S	chemiresistor	2 ppb	2 ppb−1.2 ppm	S44
reduced graphene oxide-Cu_2O composite	H_2S	chemiresistor	5 ppb	5−100 ppb	S45
graphene −PSS−PANI composite	H_2S	chemiresistor	1 ppm	1−50 ppm	S46
CuO-doped $(Ba_{0.8}Sr_{0.2})(Sn_{0.8}Ti_{0.2})O_3$ thick film	H_2S	resistor	4-10 ppb	1-100 ppm	S47
Nafion membrane (H_2SO_4 treated)	H_2S	electrochemical	100 ppb	0.1-100 ppm	S48
Polyaniline-$CuCl_2$ composite	H_2S	resistor	180 ppb	10-100 ppm	S49
TEMPO functionalized single-walled carbon nanotube	H_2S	chemiresistor	N/A	10 -100 ppm	S50
Au nanoparticle- single-walled carbon nanotube composite	H_2S	chemiresistor	3 ppb	20-1000 ppb	S51
YZ-$LiNbO_3$ film	H_2S	surface acoustic wave	N/A	1-10 ppm	S52
N/A	H_2S	microchannel scrubber with microfluoroscence detector	1 ppb	<0.02 ppm	S53
N/A	H_2S	gas chromatography with pulsed flame photometric detector (GC-PFPD)	2.4 ppb	100 ppb-6000 pb	S54
N/A	H_2S	gas chromatography with thermal conductivity detector (GC-TCD)	0.5 ppm	0.5-100 ppm	S55
N/A	H_2S	gas chromatography with flame photometric detector (GC-FPD)	~20 ppb	20-1500 ppb	S56
N/A	H_2S	gas chromatography with sulfur chemiluminescent detector (GC-SCD)	75 pg/mL	<60 ng/mL	S57
N/A	H_2S	cavity ring-down spectroscopy	105 ppb	N/A	S58
NiPc-Ni	NO	chemiresistor	0.06-1.06 ppb	20-1000 ppb	This work

NiPc-Cu	NO	chemiresistor	0.13-1.00 ppb	20-1000 ppb	This work
M_3HHTP_2−Graphene (M = Fe, Co, Ni, or Cu)	NO	chemiresistor	17 ppm	5−80 ppm	S29
Ni_3HITP_2, Ni_3HHTP_2	NO	chemiresistor	0.16, 1.4 ppm	2.5−80 ppm	S18
graphene	NO	chemiresistor	158 ppq	10 ppt	S59
MoS_2	NO	chemiresistor	0.8 ppm	0.3-2 ppm	S60
Pd–Pt/WO_3/p-Si/Al	NO	chemiresistor	N/A	50-250ppm	S61
functionalized carbon nanotubes	NO	chemiresistor	N/A	1-100 ppm	S62
WO_3	NO	potentiometric sensor array	N/A	1-100 ppb	S63
N/A	NO	gas chromatography with thermal conductivity detector (GC-TCD)	12 ppm	N/A	S64
N/A	NO	chemiluminescence	1 pmol	3-100000 pmol	S65
N/A	NO	cavity ring-down spectroscopy	0.7 ppb	<1 ppm	S66

13.3. XPS and EPR Studies of Gas Exposure

For each sample used for XPS and EPR test, about 2 mg and 6 mg of MOF materials were used for analytes exposure, respectively. The analyte-exposed samples were prepared by a gas purging cycle of N_2 (1 L/min, 30 minutes)—analyte (a controlled concentration, 30 min)—N_2 (1 L/min, 30 minutes) on pristine MOF materials. The concentrations of the analytes are controlled at 40 ppm for H_2S and NH_3, and 1 ppm for NO, respectively. The analyte-exposed samples were immediately used for EPR tests using the operation conditions as described in **Section 8**. For the XPS tests, the analyte exposed samples were prepared about 18 hours in advance, and were stored under N_2 at room temperature until the testing was done. The XPS analysis was performed under a pressure of ~10^{-9} psi.

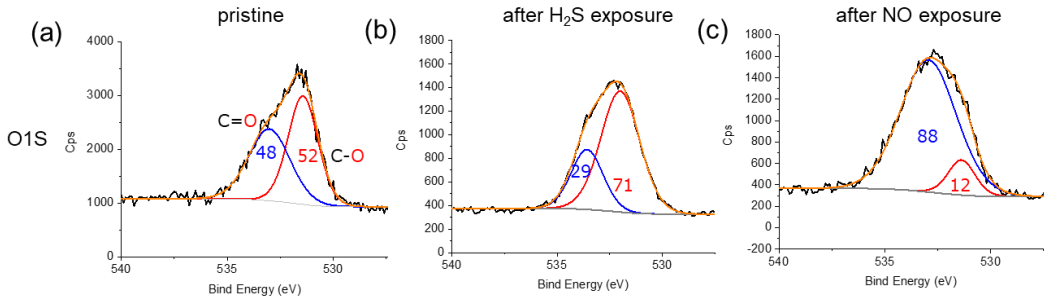

Figure S88. Comparison of the O1S XPS spectrum of (a) pristine **NiPc-Ni**, (b) **NiPc-Ni** with the exposure of H_2S (40 ppm for 30 minutes), and (c) **NiPc-Ni** with the exposure of NO (1 ppm for 30 minutes). Deconvoluted peaks of O1S from C=O and C-O are in blue and red, respectively, and the ratios (%) of peak area are given accordingly. The origin curves are the sum of the deconvoluted peaks.

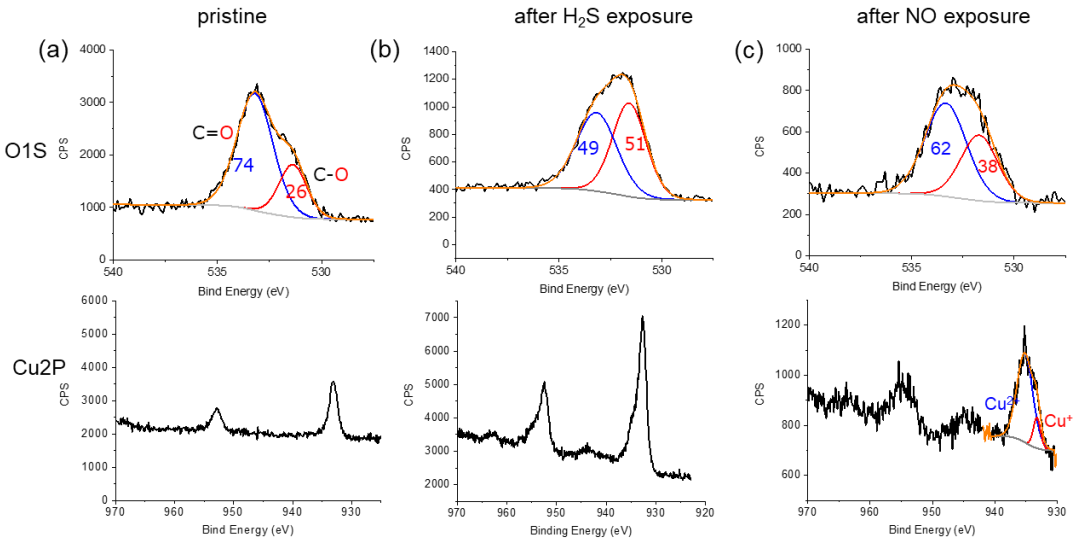

Figure S89. Comparison of the O1S and Cu2P XPS spectrum of (a) pristine **NiPc-Cu**, (b) **NiPc-Cu** after exposure to H_2S (40 ppm for 30 minutes), and (c) **NiPc-Cu** after the exposure to NO (1 ppm for 30 minutes). Deconvoluted peaks of O1S from C=O and C-O are in blue and red, respectively, and the ratios (%) of peak area are given accordingly. The deconvoluted Cu2p peaks in (c) in blue and red are Cu^{2+} and Cu^{+}, respectively. The origin curves are the sum of the deconvoluted peaks.

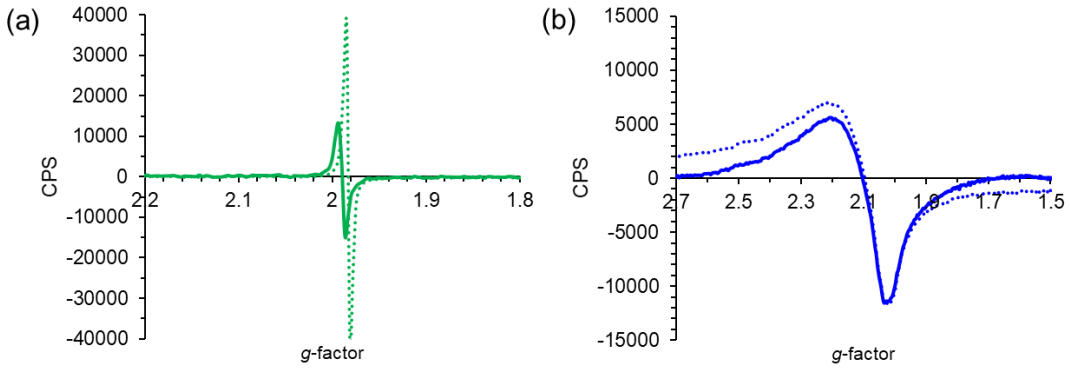

Figure S90. Comparison of the EPR spectrum of (a) **NiPc-Ni** and (b) **NiPc-Cu** with (solid line) and without (dash line) the exposure of 40 ppm H_2S for 30 minutes.

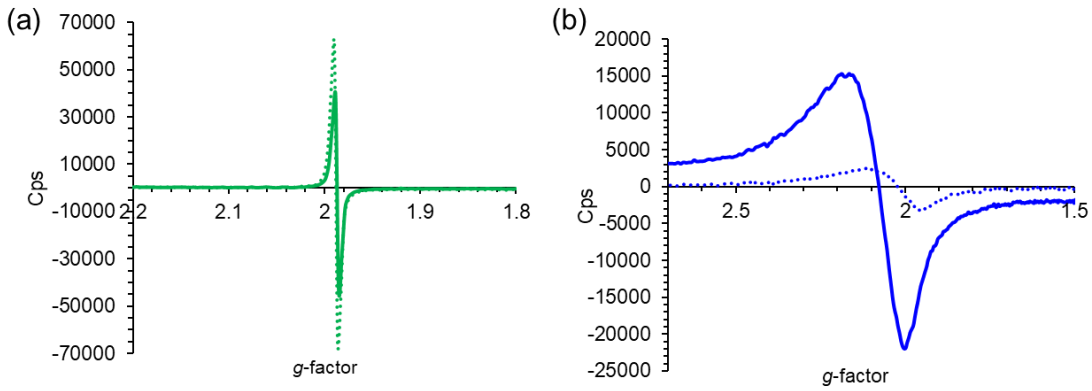

Figure S91. Comparison of the EPR spectrum of (a) **NiPc-Ni** and (b) **NiPc-Cu** with (solid line) and without (dash line) the exposure of 1 ppm NO for 30 minutes.

14. References

S1. Iqbal, Z.; Lyubimtsev, A.; Hanack, M. Synthesis of Phthalonitriles Using a Palladium Catalyst. *Synlett* **2008**, 2287.

S2. Rudiger, E. C.; Rominger, F.; Steuer, L.; Bunz, U. H. Synthesis of Substituted Trinaphthylenes. *J. Org. Chem.* **2016,** *81*, 193.

S3. Ruf, M.; Lawrence, A. M.; Noll, B. C.; Pierpont, C. G. Silicon and Zinc Coordination to Peripheral Catechol Sites of (2,3,9,10,16,17,23,24-Octahydroxyphthalocyaninato)Nickel(II). Phthalocyanine Coordination Chemistry at the Edge. *Inorg. Chem.* **1998,** *37*, 1992.

S4. Sheberla, D.; Sun, L.; Blood-Forsythe, M. A.; Er, S.; Wade, C. R.; Brozek, C. K.; Aspuru-Guzik, A.; Dincă, M. High Electrical Conductivity in Ni_3(2,3,6,7,10,11-Hexaiminotriphenylene)$_2$, a Semiconducting Metal–Organic Graphene Analogue. *J. Am. Chem. Soc.* **2014,** *136*, 8859.

S5. Dong, R.; Pfeffermann, M.; Liang, H.; Zheng, Z.; Zhu, X.; Zhang, J.; Feng, X. Large-Area, Free-Standing, Two-Dimensional Supramolecular Polymer Single-Layer Sheets for Highly Efficient Electrocatalytic Hydrogen Evolution. *Angew. Chem. Int. Ed.* **2015,** *54*, 12058.

S6. Wu, S.; Wen, G.; Schlogl, R.; Su, D. S. Carbon Nanotubes Oxidized by a Green Method as Efficient Metal-Free Catalysts for Nitroarene Reduction. *Phys. Chem. Chem. Phys.* **2015,** *17*, 1567.

S7. Qi, W.; Liu, W.; Zhang, B.; Gu, X.; Guo, X.; Su, D. Oxidative Dehydrogenation on Nanocarbon: Identification and Quantification of Active Sites by Chemical Titration. *Angew. Chem. Int. Ed.* **2013,** *52*, 14224.

S8. Sandhyarani, N.; Pradeep, T. An Investigation of the Structure and Properties of Layered Copper Thiolates. *J. Mater. Chem.* **2001,** *11*, 1294.

S9. Clough, A. J.; Skelton, J. M.; Downes, C. A.; de la Rosa, A. A.; Yoo, J. W.; Walsh, A.; Melot, B. C.; Marinescu, S. C. Metallic Conductivity in a Two-Dimensional Cobalt Dithiolene Metal–Organic Framework. *J. Am. Chem. Soc.* **2017,** *139*, 10863.

S10. Dou, J. H.; Sun, L.; Ge, Y.; Li, W.; Hendon, C. H.; Li, J.; Gul, S.; Yano, J.; Stach, E. A.; Dincă, M. Signature of Metallic Behavior in the Metal–Organic Frameworks M_3(Hexaiminobenzene)$_2$ (M = Ni, Cu). *J. Am. Chem. Soc.* **2017,** *139*, 13608.

S11. Kambe, T.; Sakamoto, R.; Kusamoto, T.; Pal, T.; Fukui, N.; Hoshiko, K.; Shimojima, T.; Wang, Z.; Hirahara, T.; Ishizaka, K.; Hasegawa, S.; Liu, F.; Nishihara, H. Redox Control and High Conductivity of Nickel Bis(Dithiolene) Complex π-Nanosheet: A Potential Organic Two-Dimensional Topological Insulator. *J. Am. Chem. Soc.* **2014,** *136*, 14357.

S12. Ding, X.; Feng, X.; Saeki, A.; Seki, S.; Nagai, A.; Jiang, D. Conducting

Metallophthalocyanine 2D Covalent Organic Frameworks: The Role of Central Metals in Controlling π-Electronic Functions. *Chem. Commun.* **2012,** *48*, 8952.
S13. Jin, S.; Ding, X.; Feng, X.; Supur, M.; Furukawa, K.; Takahashi, S.; Addicoat, M.; El-Khouly, M. E.; Nakamura, T.; Irle, S.; Fukuzumi, S.; Nagai, A.; Jiang, D. Charge Dynamics in a Donor-Acceptor Covalent Organic Framework with Periodically Ordered Bicontinuous Heterojunctions. *Angew. Chem. Int. Ed.* **2013,** *52*, 2017.
S14. Wan, S.; Gándara, F.; Asano, A.; Furukawa, H.; Saeki, A.; Dey, S. K.; Liao, L.; Ambrogio, M. W.; Botros, Y. Y.; Duan, X.; Seki, S.; Stoddart, J. F.; Yaghi, O. M. Covalent Organic Frameworks with High Charge Carrier Mobility. *Chem. Mater.* **2011,** *23*, 4094.
S15. Feng, X.; Liu, L.; Honsho, Y.; Saeki, A.; Seki, S.; Irle, S.; Dong, Y.; Nagai, A.; Jiang, D. High-Rate Charge-Carrier Transport in Porphyrin Covalent Organic Frameworks: Switching from Hole to Electron to Ambipolar Conduction. *Angew. Chem. Int. Ed.* **2012,** *51*, 2618.
S16. Schroder, D. K. *Semiconductor Material and Device Characterization*. John Wiley & Sons, Inc.: 2005.
S17. Smits, F. M. Measurement of Sheet Resistivities with the Four-Point Probe. *Bell System Technical Journal* **1958,** *37*, 711.
S18. Smith, M. K.; Mirica, K. A. Self-Organized Frameworks on Textiles (SOFT): Conductive Fabrics for Simultaneous Sensing, Capture, and Filtration of Gases. *J. Am. Chem. Soc.* **2017,** *139*, 16759.
S19. Li, J.; Lu, Y.; Ye, Q.; Cinke, M.; Han, J.; Meyyappan, M. Carbon Nanotube Sensors for Gas and Organic Vapor Detection. *Nano Lett.* **2003,** *3*, 929.
S20. Ammu, S.; Dua, V.; Agnihotra, S. R.; Surwade, S. P.; Phulgirkar, A.; Patel, S.; Manohar, S. K. Flexible, All-Organic Chemiresistor for Detecting Chemically Aggressive Vapors. *J. Am. Chem. Soc.* **2012,** *134*, 4553.
S21. Samarghandi, M. R.; Hadi, M.; McKay, G. Breakthrough Curve Analysis for Fixed-Bed Adsorption of Azo Dyes Using Novel Pine Cone—Derived Active Carbon. *Adsorption Science & Technology* **2014,** *32*, 791.
S22. Garcia, S.; Gil, M. V.; Martin, C. F.; Pis, J. J.; Rubiera, F.; Pevida, C. Breakthrough Adsorption Study of a Commercial Activated Carbon for Pre-Combustion CO_2 Capture. *Chem. Eng. J.* **2011,** *171*, 549.
S23. Riedel, K.; Renneberg, R.; Khn, M.; Scheller, F. A Fast Estimation of Biochemical Oxygen Demand Using Microbial Sensors. *Appl. Microbiol. Biotechnol.* **1988,** *28*.
S24. Tan, T. C.; Li, F.; Neoh, K. G. Measurement of BOD by Initial Rate of Response of a Microbial Sensor. *Sensors Actuators B: Chem.* **1993,** *10*, 137.
S25. Bohrer, F. I.; Sharoni, A.; Colesniuc, C.; Park, J.; Schuller, I. K.; Kummel, A. C.; Trogler, W. C. Gas Sensing Mechanism in Chemiresistive Cobalt and Metal-Free Phthalocyanine Thin Films. *J. Am. Chem. Soc.* **2007,** *129*, 5640.
S26. Kong, J.; Javey, A. *Carbon Nanotube Electronics*. 2009.
S27. Yao, M.-S.; Lv, X.-J.; Fu, Z.-H.; Li, W.-H.; Deng, W.-H.; Wu, G.-D.; Xu, G. Layer-by-Layer Assembled Conductive Metal–Organic Framework Nanofilms for Room-Temperature Chemiresistive Sensing. *Angew. Chem. Int. Ed.* **2017,** *129*, 16737.
S28. Campbell, M. G.; Sheberla, D.; Liu, S. F.; Swager, T. M.; Dincă, M. Cu_3(Hexaiminotriphenylene)$_2$: An Electrically Conductive 2D Metal–Organic Framework for Chemiresistive Sensing. *Angew. Chem. Int. Ed.* **2015,** *54*, 4349.
S29. Ko, M.; Aykanat, A.; Smith, M. K.; Mirica, K. A. Drawing Sensors with Ball-Milled Blends of Metal–Organic Frameworks and Graphite. *Sensors* **2017,** *17*, 2192.
S30. Schedin, F.; Geim, A. K.; Morozov, S. V.; Hill, E. W.; Blake, P.; Katsnelson, M. I.; Novoselov, K. S. Detection of Individual Gas Molecules Adsorbed on Graphene. *Nat. Mater.* **2007,** *6*, 652.
S31. Paul, R. K.; Badhulika, S.; Saucedo, N. M.; Mulchandani, A. Graphene Nanomesh as Highly Sensitive Chemiresistor Gas Sensor. *Anal. Chem.* **2012,** *84*, 8171.

S32. Donarelli, M.; Ottaviano, L.; Giancaterini, L.; Fioravanti, G.; Perrozzi, F.; Cantalini, C. Exfoliated Black Phosphorus Gas Sensing Properties at Room Temperature. *2D Mater.* **2016,** *3*, 025002.
S33. Lee, K.; Gatensby, R.; McEvoy, N.; Hallam, T.; Duesberg, G. S. High-Performance Sensors Based on Molybdenum Disulfide Thin Films. *Adv. Mater.* **2013,** *25*, 6699.
S34. Hu, N.; Yang, Z.; Wang, Y.; Zhang, L.; Wang, Y.; Huang, X.; Wei, H.; Wei, L.; Zhang, Y. Ultrafast and Sensitive Room Temperature NH_3 Gas Sensors Based on Chemically Reduced Graphene Oxide. *Nanotechnology* **2014,** *25*, 025502.
S35. Kim, S. J.; Koh, H. J.; Ren, C. E.; Kwon, O.; Maleski, K.; Cho, S. Y.; Anasori, B.; Kim, C. K.; Choi, Y. K.; Kim, J.; Gogotsi, Y.; Jung, H. T. Metallic $Ti_3C_2T_x$ MXene Gas Sensors with Ultrahigh Signal-to-Noise Ratio. *ACS Nano* **2018,** *12*, 986.
S36. Kong, J.; Franklin, N. R.; Zhou, C. W.; Chapline, M. G.; Peng, S.; Cho, K. J.; Dai, H. J. Nanotube Molecular Wires as Chemical Sensors. *Science* **2000,** *287*, 622.
S37. Panes-Ruiz, L. A.; Shaygan, M.; Fu, Y.; Liu, Y.; Khavrus, V.; Oswald, S.; Gemming, T.; Baraban, L.; Bezugly, V.; Cuniberti, G. Toward Highly Sensitive and Energy Efficient Ammonia Gas Detection with Modified Single-Walled Carbon Nanotubes at Room Temperature. *ACS Sens.* **2018,** *3*, 79.
S38. Chabukswar, V. V.; Pethkar, S.; Athawale, A. A. Acrylic Acid Doped Polyaniline as an Ammonia Sensor. *Sens. Actuators, B: Chem.* **2001,** *77*, 657.
S39. Winquist, F.; Spetz, A.; Lundstrom, I.; Danielsson, B. Determination of Ammonia in Air and Aqueous Samples with a Gas-Sensitive Semiconductor Capacitor. *Anal. Chim. Acta* **1984,** *164*, 127.
S40. Mount, G. H.; Rumburg, B.; Havig, J.; Lamb, B.; Westberg, H.; Yonge, D.; Johnson, K.; Kincaid, R. Measurement of Atmospheric Ammonia at a Dairy Using Differential Optical Absorption Spectroscopy in the Mid-Ultraviolet. *Atmos. Environ.* **2002,** *36*, 1799.
S41. Dawson, M. L.; Perraud, V.; Gomez, A.; Arquero, K. D.; Ezell, M. J.; Finlayson-Pitts, B. J. Measurement of Gas-Phase Ammonia and Amines in Air by Collection onto an Ion Exchange Resin and Analysis by Ion Chromatography. *Atmos. Meas. Tech.* **2014,** *7*, 2733.
S42. Kataoka, H.; Ohrui, S.; Kanemoto, A.; Makita, M. Determination of Ammonia as Its Benzenesulphonyldimethylaminomethylene Derivative in Environmental Water Samples by Gas-Chromatography with Flame Photometric Detection. *J. Chromatogr.* **1993,** *633*, 311.
S43. Manne, J.; Sukhorukov, O.; Jager, W.; Tulip, J. Pulsed Quantum Cascade Laser-Based Cavity Ring-Down Spectroscopy for Ammonia Detection in Breath. *Appl. Opt.* **2006,** *45*, 9230.
S44. Zhang, F.; Zhu, A. W.; Luo, Y. P.; Tian, Y.; Yang, J. H.; Qin, Y. CuO Nanosheets for Sensitive and Selective Determination of H_2S with High Recovery Ability. *J. Phys. Chem. C* **2010,** *114*, 19214.
S45. Zhou, L.; Shen, F.; Tian, X.; Wang, D.; Zhang, T.; Chen, W. Stable Cu_2O Nanocrystals Grown on Functionalized Graphene Sheets and Room Temperature H_2S Gas Sensing with Ultrahigh Sensitivity. *Nanoscale* **2013,** *5*, 1564.
S46. Cho, S.; Lee, J. S.; Jun, J.; Kim, S. G.; Jang, J. Fabrication of Water-Dispersible and Highly Conductive PSS-Doped PANI/Graphene Nanocomposites Using a High-Molecular Weight Pss Dopant and Their Application in H_2S Detection. *Nanoscale* **2014,** *6*, 15181.
S47. Jain, G. H.; Patil, L. A. Cuo-Doped Bsst Thick Film Resistors for ppb Level H_2S Gas Sensing at Room Temperature. *Sens. Actuators, B: Chem.* **2007,** *123*, 246.
S48. Yu, C. B.; Wang, Y. J.; Hua, K. F.; Xing, W.; Lu, T. H. Electrochemical H_2S Sensor with H_2SO_4 Pre-Treated Nafion Membrane as Solid Polymer Electrolyte. *Sens. Actuators, B: Chem.* **2002,** *86*, 259.
S49. Crowley, K.; Morrin, A.; Shepherd, R. L.; Panhuis, M. I. H.; Wallace, G. G.; Smyth, M. R.; Killard, A. J. Fabrication of Polyaniline-Based Gas Sensors Using Piezoelectric Inkjet and Screen Printing for the Detection of Hydrogen Sulfide. *IEEE Sens. J.* **2010,** *10*, 1419.
S50. Jung, H. Y.; Kim, Y. L.; Park, S.; Datar, A.; Lee, H. J.; Huang, J.; Somu, S.; Busnaina, A.;

Jung, Y. J.; Kwon, Y. K. High-Performance H_2S Detection by Redox Reactions in Semiconducting Carbon Nanotube-Based Devices. *Analyst* **2013,** *138*, 7206.
S51. Mubeen, S.; Zhang, T.; Chartuprayoon, N.; Rheem, Y.; Mulchandani, A.; Myung, N. V.; Deshusses, M. A. Sensitive Detection of H_2S Using Gold Nanoparticle Decorated Single-Walled Carbon Nanotubes. *Anal. Chem.* **2010,** *82*, 250.
S52. Galipeau, J. D.; LeGore, L. J.; Snow, K.; Caron, J. J.; Vetelino, J. F.; Andle, J. C. The Integration of a Chemiresistive Film Overlay with a Surface Acoustic Wave Microsensor. *Sens. Actuators, B: Chem.* **1996,** *35*, 158.
S53. Toda, K.; Ohira, S.; Ikeda, M. Micro-Gas Analysis System μGAS Comprising a Microchannel Scrubber and a Micro-Fluorescence Detector for Measurement of Hydrogen Sulfide. *Anal. Chim. Acta* **2004,** *511*, 3.
S54. Ki-Hyun, K. Performance Characterization of the GC/PFPD for H_2S, CH_3SH, DMS, and DMDS in Air. *Atmos. Environ.* **2005,** *39*, 2235.
S55. Rath, H. J.; Wimmer, J. Gas Chromatographic Analysis of Traces of Hydrogen Sulfide in Hydrogen. *Chromatographia* **1980,** *13*, 513.
S56. Mangani, F.; Bruner, F.; Penna, N. F. Interferences in Determination of Hydrogen-Sulfide in Air by Gas-Chromatography with Flame Photometric Detection. *Anal. Chem.* **1983,** *55*, 2193.
S57. Vitvitsky, V.; Banerjee, R. H_2S Analysis in Biological Samples Using Gas Chromatography with Sulfur Chemiluminescence Detection. *Method Enzymol* **2015,** *554*, 111.
S58. Siciliani de Cumis, M.; Viciani, S.; Galli, I.; Mazzotti, D.; Sorci, F.; Severi, M.; D'Amato, F. Note: An Analyzer for Field Detection of H_2S by Using Cavity Ring-Down at 1.57 μm. *Rev. Sci. Instrum.* **2015,** *86*, 056108.
S59. Chen, G.; Paronyan, T. M.; Harutyunyan, A. R. Sub-ppt Gas Detection with Pristine Graphene. *Appl. Phys. Lett.* **2012,** *101*, 053119.
S60. Li, H.; Yin, Z.; He, Q.; Li, H.; Huang, X.; Lu, G.; Fam, D. W.; Tok, A. I.; Zhang, Q.; Zhang, H. Fabrication of Single- and Multilayer MoS_2 Film-Based Field-Effect Transistors for Sensing NO at Room Temperature. *Small* **2012,** *8*, 63.
S61. Zhang, W.; Uchida, H.; Katsube, T.; Nakatsubo, T.; Nishioka, Y. A Novel Semiconductor NO Gas Sensor Operating at Room Temperature. *Sens. Actuators, B: Chem.* **198,** *49*, 58.
S62. Maklin, J.; Mustonen, T.; Kordas, K.; Saukko, S.; Toth, G.; Vahakangas, J. Nitric Oxide Gas Sensors with Functionalized Carbon Nanotubes. *Phys. Status Solidi B* **2007,** *244*, 4298.
S63. Mondal, S. P.; Dutta, P. K.; Hunter, G. W.; Ward, B. J.; Laskowski, D.; Dweik, R. A. Development of High Sensitivity Potentiometric NO_x Sensor and Its Application to Breath Analysis. *Sens. Actuators, B: Chem.* **2011,** *158*, 292.
S64. Dietz, R. N. Gas Chromatographic Determination of Nitric Oxide on Treated Molecular Sieve. *Anal. Chem.* **1968,** *40*, 1576.
S65. Bateman, R. M.; Ellis, C. G.; Freeman, D. J. Optimization of Nitric Oxide Chemiluminescence Operating Conditions for Measurement of Plasma Nitrite and Nitrate. *Clin. Chem.* **2002,** *48*, 570.
S66. Kosterev, A. A.; Malinovsky, A. L.; Tittel, F. K.; Gmachl, C.; Capasso, F.; Sivco, D. L.; Baillargeon, J. N.; Hutchinson, A. L.; Cho, A. Y. Cavity Ringdown Spectroscopic Detection of Nitric Oxide with a Continuous-Wave Quantum-Cascade Laser. *Appl. Opt.* **2001,** *40*, 5522.